Regulation of Directional Cell Migration from within the Nuclear Envelope

A Dissertation
SUBMITTED TO THE FACULTY OF
UNIVERSITY OF MINNESOTA
BY

Cosmo Augustus Saunders

IN PARTIAL FULFILLMENT OF THE REQUIREMENTS
FOR THE DEGREE OF
DOCTOR OF PHILOSOPHY

G.W. Gant Luxton, Adviser

March 2017

Acknowledgements

I would like to thank my adviser, Dr. G.W. Gant Luxton, for the opportunity to pursue my Ph.D. in his laboratory. He always encouraged me to tackle all questions that arose head-on and made sure I had the tools and reagents available to do so. He also showed me the power of interdisciplinary collaborations.

I would like to express my gratitude to all members of the Luxton lab that I have worked alongside. In particular, I thank Brian Woolums, Patrick Willey, Amy Schoenhofen, Alex McQuown and Jared Erickson for technical assistance, help with data analysis and troubleshooting, as well as ideas and helpful discussions.

I thank my collaborators in Dr. Joachim Mueller's lab, particularly Joachim Mueller, Jared Hennen, and Elizabeth M. Smith, for many productive interactions and discussions. It has been a very eye-opening and rewarding experience.

I am appreciative of Dr. Margaret Titus for her patience, help, guidance, and advice. Additionally, I thank researchers in her lab, specifically Ashley Arthur and Karl Petersen, for their help with experimental procedures, reagents, insightful comments and discussions, particularly in facilitating my introduction to *Dictyostelium discoideum*.

I am indebted to the members of my thesis committee, Drs. Laura Gammill, Melissa Gardner, Tom Hays, Lorene Lanier, and Harry Orr. Laura was an outstanding committee chair and went above and beyond her duty to help me when I requested it.

I made many wonderful friends during graduate school who helped balance life with research. To rephrase a passage from Faulkner's *The Sound and the Fury*… "they allowed me to forget my research every now and then for a moment and not spend all of my breath trying conquer it, as it is never done. Research often reveals to you your own folly and despair, and victory is an illusion of philosophers and fools." I also thank TT&tWNS for many great jam sessions.

I would like to especially thank my parents, Dr. Nancy C. Saunders, D.V.M., and Dr. James C. Sorenson, Ph.D., for their unwavering support. They taught me to think critically, sparked my interest in science, and instilled in me a sense of humor.

Table of Contents

LIST OF FIGURES

Chapter 1

INTRODUCTION:

Cell migration is fundamental biological process (Liu and Parent, 2011). Defective cell migration in multicellular organisms can lead to aberrant development, impair wound healing, and cancer metastasis (Aman and Piotrowski, 2010; Majumdar et al., 2014). During migration, the leading edge of the cell protrudes forward in order to interact with and direct the cell through its environment (Ridley, 2011). While much work has been focused on the cellular processes at the leading edge of the cell during migration, the proper positioning of organelles within a cell is an often overlooked but critical event during migration (Li and Gundersen, 2008).

Many migratory cell types, including fibroblasts, neurons, and *Dictyostelium* juxtaposition their nuclei and centrosome, such that one is closer to the leading edge than other (Luxton and Gundersen, 2011). Drawing a line through the center of the nucleus and centrosome highlights an axis of cell polarity. The alignment of the nucleus and centrosome along this axis is postulated to be a way for cells to maintain polarity during migration (Li and Gundersen, 2008). This axis is typically parallel to the direction of migration, although does not necessarily point in the direction of migration.

When the centrosome is positioned in front of the nucleus, this is termed

anterior centrosome orientation, and is seen in several cell types, including fibroblasts, neurons, and astrocytes (Gundersen and Worman, 2013). Other cell

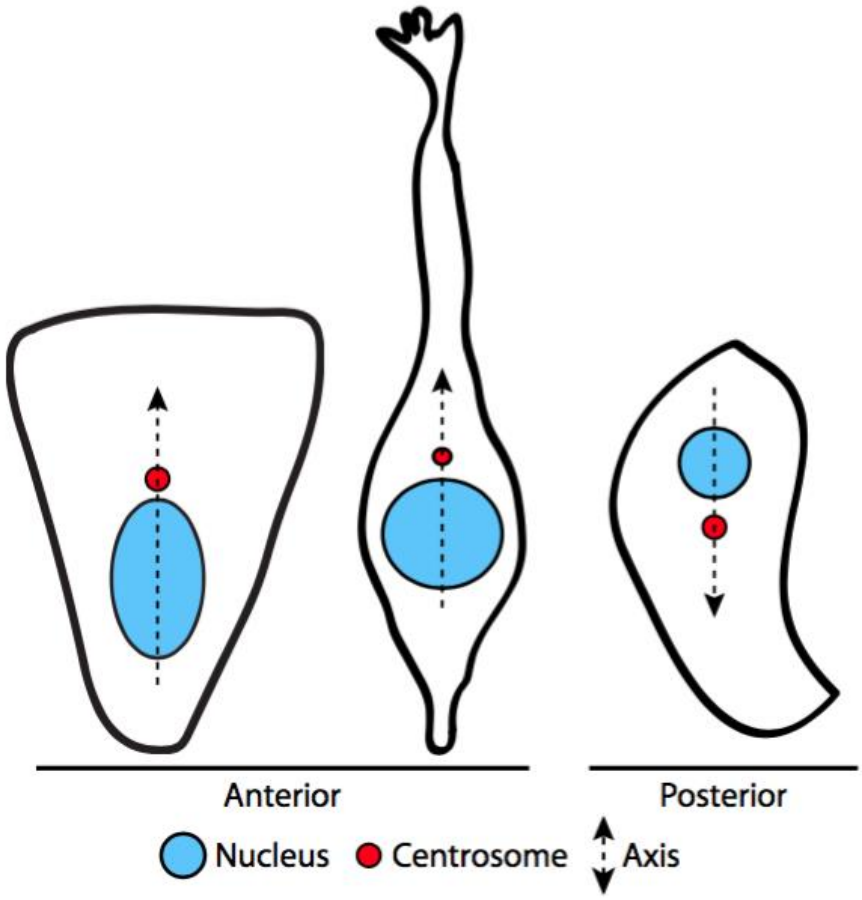

Figure 1: The NC axis of orientation. Idealized cells showing anterior and posterior centrosome orientation. Left to Right: A fibroblast, a neuron, and a *Dictyostelium*. All cell types are migrating towards the top of the page.

types, including neutrophils and *Dictyostelium* cells will migrate with a posterior centrosome orientation. In many migratory cell types, the centrosome nucleates microtubules and serves as a microtubule organizing center (MTOC) (Bartolini and Gundersen, 2006). The tight positioning of the centrosome to the nucleus thus allows for the dynamic ends of microtubules to grow away from the nucleus, allowing for efficient microtubule-based trafficking events to occur unimpeded by the relatively large nucleus (Luxton and Gundersen, 2011).

The nucleus is the largest organelle in eukaryotic cells and houses the genomic DNA by enveloping it in concentric membranes separated by 30-50 nm, consisting of the inner and outer nuclear membrane (INM and ONM, respectively) (Hetzer et al., 2005; Tzur et al., 2006; Wilson and Dawson, 2011). The nuclear envelope (NE) is composed of these two membranes, the perinuclear space (PNS) found between them and the underlying nuclear lamina which allows the nucleus to maintain its shape (Devos et al., 2014).

Nuclear positioning during migration in fibroblasts

While it was initially thought that the centrosome is moved to a position in front of a stationary nucleus during anterior centrosome orientation, direct imaging of fibroblasts orienting for migration showed that the nucleus is moved rearward while the centrosome is maintained in the center of the cell (Gomes et al., 2005). Anterior centrosome orientation is set up by a cascade of signaling pathways (Gundersen and Worman, 2013). The cascade starts with the Lysophosphatidic acid (LPA) receptor, which signals through small rho-GTPase

Cell division control protein 42 (Cdc-42) to begin two major events, maintaining the centrosome at the center of the cell via plasma membrane anchored microtubules, and rearward nuclear movement, via actomyosin contractility (Gomes et al., 2005).

After activation of Cdc-42, there is a bifurcation in the pathway. One branch of the pathway activates the PAR3/6 complex, which interacts with the dynein/dynactin complex. This branch of the pathway is needed for anchoring the plus end tips of microtubules to the sides of cells at cell-cell contacts, thus allowing for the centrosome to be maintained in the center of the cell, (Schmoranzer et al., 2009; Gomes et al., 2005). In the other branch downstream of cdc-42, myotonic dystrophy kinase-related Cdc42-binding kinase (MRCK) activates myosin-IIb, which bundles actin into cables and induces retrograde actin flow and rearward nuclear movement (Gomes et al., 2005). These cables are aligned parallel to the leading edge of the cell and flow rearward. This retrograde actin flow is harnessed by LINC complexes, which move the nucleus rearward (Luxton et al., 2010, 2011). LINC complexes are comprised of INM Sad1/Unc-84 (SUN) proteins and ONM Klarischt, Anc-1, and Syne Homology (KASH) domain containing nesprin proteins (Crisp et al., 2006).

Located on the ONM, nesprins can interact with all three components of the cytoskeleton: actin, microtubules, and intermediate filaments (FIGURE 3). These interactions can be direct, with Nesprin1-Giant and Nesprin2-Giant both

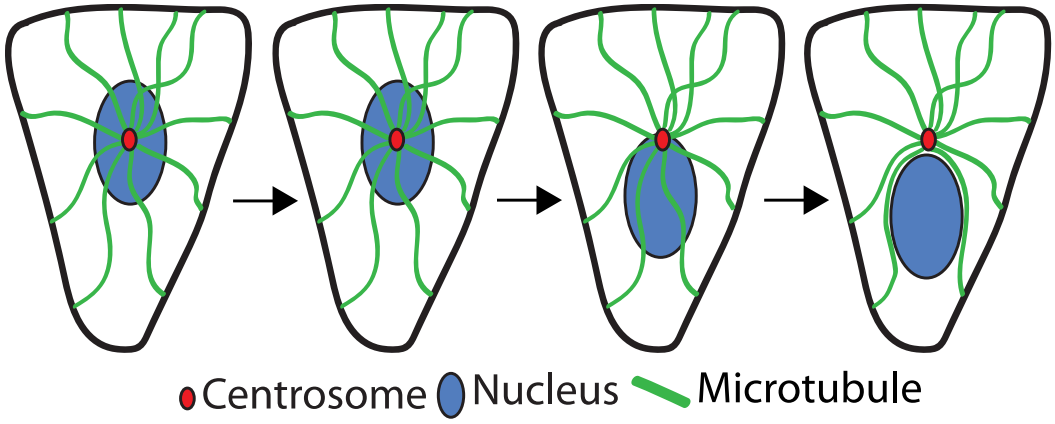

Figure 2: Nuclear and centrosomal positioning in migratory fibroblasts.

This cartoon shows a cell polarizing for migration towards the top of the page. At the beginning, the nucleus and centrosome are located randomly in the cell (although shown here in the center). Upon stimulation, the nucleus moves to the rear of the cell while the centrosome remains in the center of the cell

containing N-terminal calponin homology domains that can directly bind actin filaments (Luxton et al., 2010). Additionally, through molecular motors such as kinesin and dynein, nesprins can interact with microtubules (Roux et al., 2009). The middle portion of the giant isoforms of nesprin-1 and nesprin-2 are comprised of a series of spectrin-like repeats. These repeats are typically used for protein-protein interactions. The C-terminus of nesprins contains a transmembrane domain (TMD) that traverses the ONM and have a short 10-30 amino acid KASH peptide that extends into the lumen of the nuclear envelope (Starr and Fischer, 2005). Within the lumen of the nuclear envelope, also known as the perinuclear space (PNS), KASH peptides can directly bind to SUN proteins (Sosa et al., 2012; Wang et al., 2012).

SUN proteins have a highly conserved ~175 amino acid domain found at the C-terminus of the protein (Crisp et al., 2006). Recent crystallography studies of the C-terminal portion of the luminal domain of SUN2 show that the SUN domain is preceded by coiled-coils (Nie et al., 2016) that extend from the INM, allowing the entire luminal domain of SUN2 to span the perinuclear space, where it interacts with the KASH peptides near the ONM (Sosa et al., 2013). N-terminal to the coiled-coils of SUN proteins is a transmembrane domain which crosses the INM, allowing the N-terminus of SUN proteins to interact with the A-type nuclear lamins and chromatin within the nucleoplasm (Haque et al., 2006; Lombardi and Lammerding, 2011; Tzur et al., 2006).

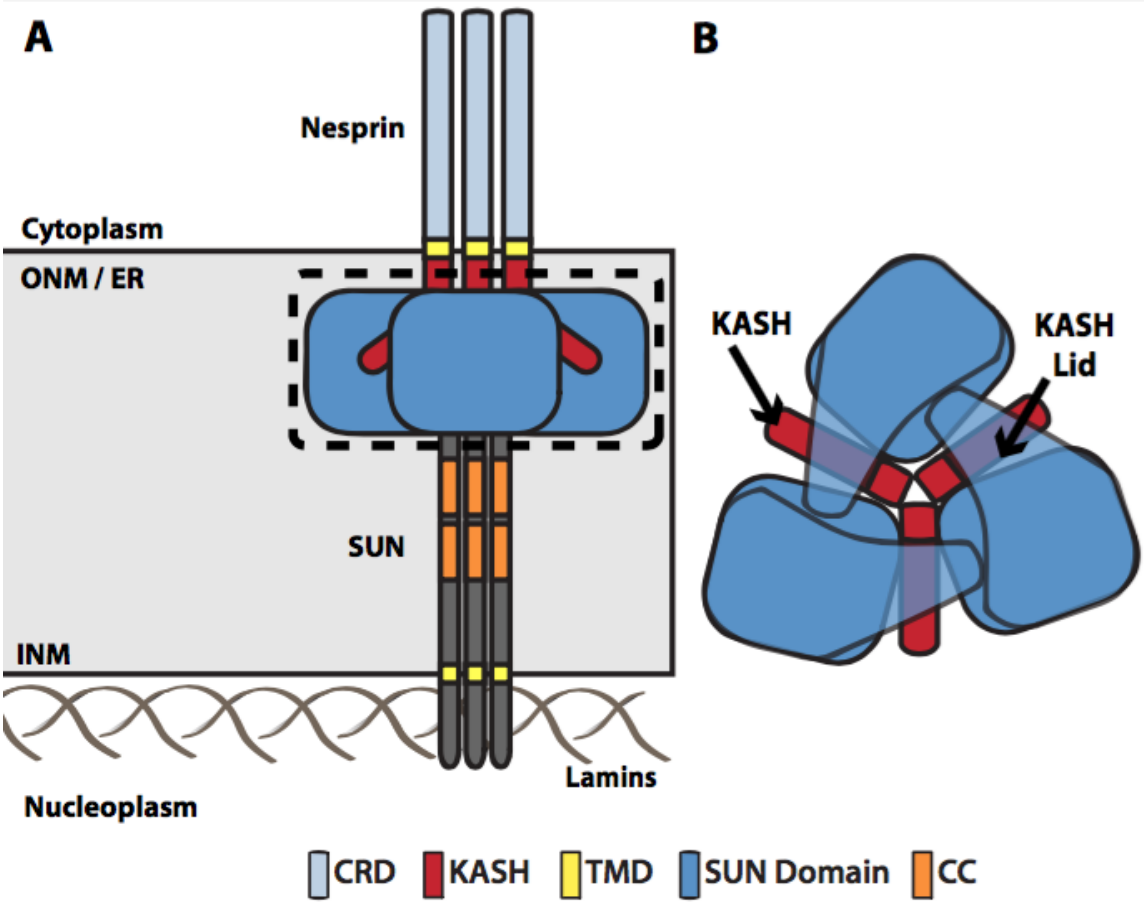

Figure 3: LINC complex interactions. (A) An intact LINC complex, with three SUN2 protomers (blue) binding three KASH domains. The portion in the dashed box is seen top down in (B). (B) A top down view of the SUN2-KASH interaction, based on the crystal structure from Sosa et al., 2012. The KASH lid of SUN2 folds down over the KASH peptide, which is wedged between SUN2 protomers. CRD: central rod domain, KASH: Klarischt, Anc-1, and Syne homology, TMD: transmembrane domain, SUN: Sad1/Unc-84 domain CC: canonical coiled-coils

Several groups have shown that SUN2 forms trimers, with the three SUN domains forming a cloverleaf like shape (Figure2, (Sosa et al., 2012; Zhou et al., 2012; Wang et al., 2012; Nie et al., 2016). This trimerization is critical for binding to KASH domains, as the KASH domain is sandwiched in a cleft formed between SUN protomers (Sosa et al., 2012; Wang et al., 2012). In this way, three SUN domains bind to three KASH domains, forming a heterohexameric complex. The SUN domain also has a flexible loop extending towards the ONM, called the KASH lid (Sosa et al., 2012). The KASH lid of SUN2 folds down over the KASH peptide of nesprins to further stabilize the complex. Due to the high degree of conservation between SUN domains, it has been predicted that all SUN proteins trimerize in a manner similar to SUN2 (Sosa et al., 2013). As an additional reinforcement, a disulfide bond forms between SUN2 and KASH, which is critical for mechanotransmission between the nucleus and the cytoplasm (Jahed et al., 2015).

An additional conformation of SUN2 has been solved, and suggests how SUN2 oligomerization could be regulated by its two coiled-coil domains, CC1 and CC2 (coiled-coil1 and coiled-coil2, respectively) (Nie et al., 2016). The crystal structure comprising the coiled-coil closest to the SUN domain, CC2, and the SUN domain showed that the KASH lid is bent backwards where it interacts with CC2. In this conformation, SUN2 would be unable to bind KASH peptides, both because the SUN domain would be unable to reach the ONM where the KASH peptides reside, but also because the KASH domain needs to be sandwiched

between SUN domains and held by the KASH lid. Coiled-coil1 plays a prominent role in controlling trimerization, as the CC1 alone and CC1-CC2 formed trimers, but CC2-SUN was found to be monomeric. Mutations in CC1 modulated oligomerization. This intrinsic dynamic regulatory model therefore says that SUN2 is inactive with the KASH lid bent back to interact with the CC2. A structural re-arrangement occurs via mechanisms unknown, which causes SUN2 to trimerize, straightening the molecule, extending it out towards the ONM and making it competent to bind KASH peptides (Nie et al., 2016).

Transmembrane Actin-Associated Nuclear Lines: TAN lines

The connection between the nucleus and rearward flowing actin during anterior centrosome orientation is mediated by assembly of higher-ordered nesprin-2G – SUN2 LINC complexes. The structures were named Transmembrane Actin-associated Nuclear (TAN) lines (Luxton et al., 2010). On the dorsal nuclear surface, linear arrays of Nesprin-2Giant directly bind actin via the N-terminus tandem Calponin homology domains (CHD), which are anchored by SUN2 to the A-type nuclear lamins within the nucleus (Luxton et al., 2010; Luxton and Gundersen, 2011; Folker et al., 2011). Disruption of LINC complex formation by overexpression of dominant-negative LINC complex constructs or siRNA mediated knockdown of SUN2 does not diminish the actin flow rearward over the nucleus, but does inhibit rearward nuclear movement (Luxton et al., 2010). Additionally, siRNA mediated knockdown of A-type nuclear lamins or

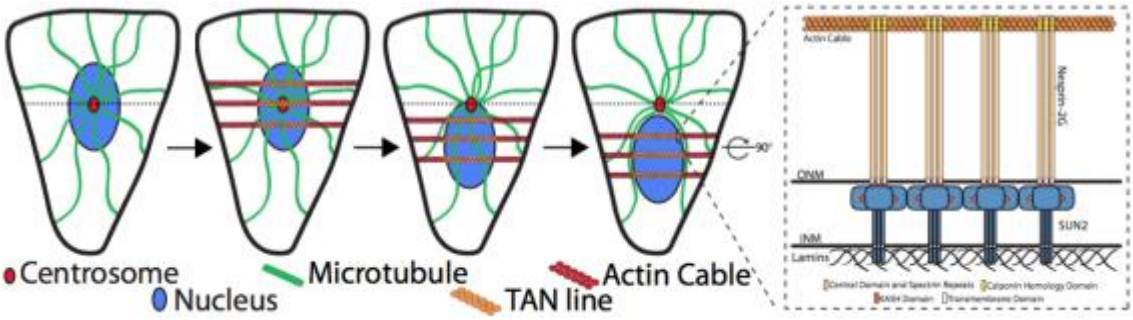

Figure 4: TAN lines move the nucleus to the rear of the cell while microtubules maintain the centrosome in the center of the cell. Dorsal perinuclear actin cables form on top of the nucleus and retrograde actin flow moves the nucleus rearward. (inset) Nesprin2G engages the actin cables via tandem Calponin homology domains in the cytoplasm and its KASH peptide binds to the SUN domain of SUN2 within the PNS. SUN2 spans most of the nuclear envelope and its N-terminus is anchored by the nuclear lamins. This connection allows for force transmission from the cytoplasm into the nucleoplasm and is required for rearward nuclear movement. For clarity, only actin cables that form over the nucleus are represented.

overexpression of lamins harboring mutations associated with striated-muscle diseases causes a failure of TAN lines to be properly anchored, resulting in defective rearward nuclear movement and leaving the nucleus in the center of the cell (Folker et al., 2011).

Dictyostelium nuclear positioning during migration

While the mechanisms of nuclear movement and positioning during polarization are probably best understood in mammalian fibroblasts, not all cell types position their nucleus in the cell rear (Luxton and Gundersen, 2011). Neutrophils and the social amoeba *Dictyostelium discoideum* can undergo migration with a posterior centrosome orientation (Chiplonkar et al., 1992; Sameshima et al., 1988). Interestingly, both neutrophils and *Dictyostelium* leave behind vesicles with signaling molecules that attract other migrating cell to follow them in a chain type fashion (Kriebel et al., 2008, 2003, Majumdar et al., 2014, 2016), further supporting the hypothesis that nuclear positioning might be controlled to help with proper vesicular trafficking (Luxton and Gundersen, 2011).

Dictyostelium discoideum encode SUN domain containing proteins, named SUN1 and SUNb (Schulz et al., 2009; Xiong et al., 2008). Additionally, they have at least two proteins similar to nesprins. One nesprin-like protein is Kif-9, which has a cytoplasmic Kinesin motor domain and has been shown to mediate nuclear-centrosomal attachment (Tikhonenko et al., 2013). The other nesprin-like protein, Interaptin, also known as actin binding protein D (Abpd), bears a striking resemblance to nesprin-2Giant; it has tandem N-terminal actin binding Calponin

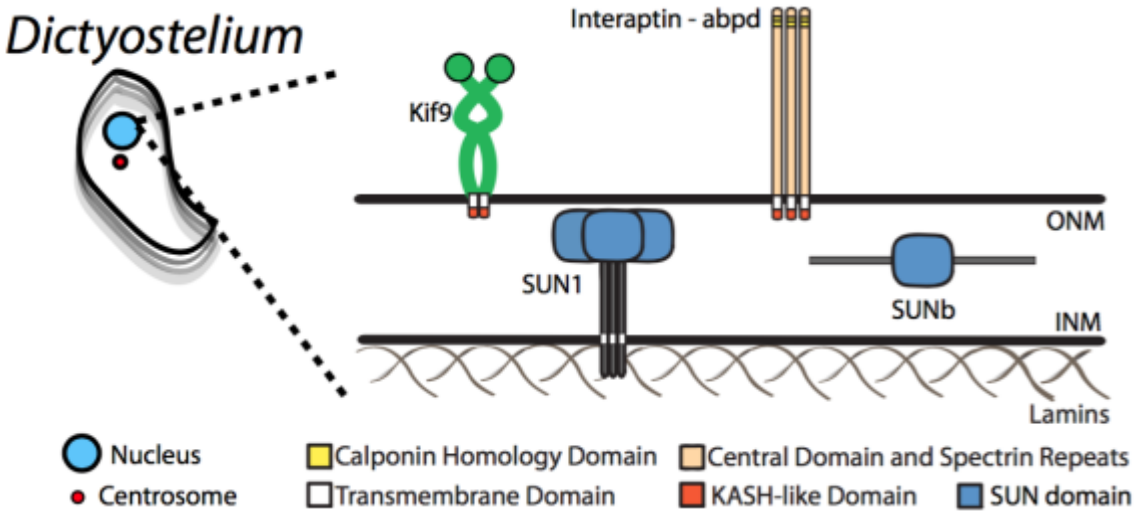

Figure 5: LINC complex components in Dictyostelium. Schematic showing potential arrangements of *Dictyostelium* LINC complex components within the Nuclear Envelope.

homology domain followed by a central domain that has spectrin-like repeats (Ponte et al., 2000; Rivero et al., 1998). Both Kif-9 and Interaptin localize to the nuclear envelope and have C-terminal single pass transmembrane domains with short peptides that extend into the lumen of the nuclear envelope (Meier, 2016).

AAA+ ATPases are ATP fueled remodeling machines.

The controlled assembly of the LINC complex is critical for many cellular functions mentioned above. During nuclear positioning prior to migration, SUN2-N2G LINC complexes need to be assembled, and then organized into linear arrays along dorsal perinuclear actin cables bound to actin in the cytoplasm. As SUN1 and SUN2 can both bind to KASH domains with similar affinity (Ostlund et al., 2009), proper regulation of the interaction with the KASH peptide of either of these two SUN proteins would be critical, since SUN1 is not a component of TAN lines (Luxton et al., 2010).

The disassembly of multiprotein complexes and protein aggregates in cells is largely accomplished by ATPases Associated with various cellular Activities (AAA+) proteins (Hanson and Whiteheart, 2005). As their name implies, AAA+ proteins are widely distributed in cells and have many important activities (White and Lauring, 2007). AAA+ proteins are found in all domains of life, and they have functional roles in all major organelles of eukaryotes. AAA+ proteins operate as ring-shaped oligomeric structures that harness the energy released from ATP hydrolysis in order to structurally remodel substrates (Stinson et al., 2013).

The typical AAA+ protein has an N-terminal adaptor-binding domain which

gives them substrate specificity (Graef et al., 2007). Following the adaptor binding domain is the AAA+ domain. There are several important motifs found within the AAA+ domain, such as Walker-A and Walker-B motifs which are needed for ATP binding and hydrolysis, respectively (White and Lauring, 2007). Mutation of the conserved glutamic acid in the Walker-B motif causes inhibition of ATP hydrolysis and tends to stabilize the AAA+ proteins as a hexamer, which is how they often bind to their substrates. This mutation is also referred to as a substrate trap mutation (Hanson and Whiteheart, 2005). Additionally, there are the sensor I and sensor II motifs that sense ATP binding (Wendler et al., 2012). Furthermore, AAA+ proteins have conserved arginine fingers which are important for ATP hydrolysis (Hanson and Whiteheart 2005). Depending upon the type of mutation, disruption of Walker-A, sensor I, sensor II, and arginine finger motifs typically does not inhibit oligomerization, but diminishes the ability of these proteins to hydrolyze ATP and do work (Wendler et al., 2012; Hanson and Whiteheart, 2005).

Another common theme is that AAA+ proteins operate as oligomeric structures, with ATP molecules situated between two subunits within the ring. When ATP is positioned in this ring, a conserved arginine from one subunit will interact with the active-site pocket of a neighboring subunit, thereby stimulating ATP hydrolysis. Upon ATP binding and hydrolysis, the ring structure of AAA+ proteins undergoes a conformational change (Stinson et al., 2013; Glynn et al., 2012, 2009). Most AAA+ proteins operate as homohexamers with a central pore

in the middle of the ring, through which substrates are pulled in an ATP dependent manner (Baker and Sauer, 2012; Hanson and Whiteheart, 2005). Oligomerization allows for ATP hydrolysis to be coupled to conformational changes throughout the ring, this being the mechanism for the protein's ability to physically remodel substrates (Glynn et al., 2009; Stinson et al., 2013). Oligomerization is also critical for ATP hydrolysis, as ATP molecules are positioned between two subunits within the ring. When ATP is positioned in this ring, a conserved arginine from one subunit will interact with the active-site pocket of a neighboring subunit, thereby stimulating ATP hydrolysis. Upon ATP binding and hydrolysis, the ring structure of AAA+ proteins undergoes a conformational change (Stinson et al., 2013; Glynn et al., 2012, 2009).

The central pore that is formed when AAA+ proteins oligomerize is lined with pore-loops that contain large hydrophobic residues (White et al., 2007; Martin et al., 2008; Roll-Mecak and Vale, 2008). These residues bind and physically pull on substrates, thus completing the link between ATP hydrolysis, conformational change, and substrate remodeling (Martin et al., 2008; White and Lauring, 2007; Sauer and Baker, 2011).

The torsin family of AAA+ proteins reside within the shared lumen of the nuclear envelope and endoplasmic reticulum and are candidate regulators of the LINC complex (Gerace, 2004; Goodchild and Dauer, 2004; Naismith et al., 2004). Torsin1A was the first family member identified and is mutated in the neurological movement disorder, DYT1 dystonia, discussed below (Ozelius et al.,

1997). Of the four other mammalian torsins, three (torsin1b, torsin2A, and torsin3A) have N-terminal signal sequences that target them to the shared lumen of the NE and ER. Torsin4A does not have an N-terminal signal sequence, it instead has a TMD and the AAA+ domain is predicted to localize to the lumen of the NE and ER (Rose et al., 2015).

Torsin1A is an Atypical AAA+ protein

Torsin1A is closely related to ClpB subfamily of AAA+ ATPases (Rose et al, 2015), although it differs from canonical AAA+ proteins in several ways. First, torsin1A lacks an obvious adaptor domain (Román-Hernández et al., 2011). Second, torsin1A monotopically associates with membranes via an N-terminal hydrophobic domain (NTD) (Vander Heyden et al., 2009, 2011). Thirdly, torsin1A has a non-canonical Walker-A motif, where the GxxxxGK[S/T] motif is instead GxxxxGKN. When the C-terminal threonine of ClpB is mutated to asparagine (T to N), it greatly diminishes the rate of ATP hydrolysis (Nagy et al., 2009). Fourthly, torsin1A has a redox-sensitive sensor II motif, which has been shown in both mammalian and *C.elegans* to be required for ATP-binding (Zhu et al., 2010, 2008). In the torsin1A sensor II, a disulfide bond forms between the highly conserved cysteines at residues 280 and 319 and is required for ATP binding (Zhu et al., 2010; Esra Demircioglu et al., 2016). Finally, torsin1A lacks a conserved arginine finger (Zhao et al., 2013; Brown et al., 2014; Sosa et al., 2014; Esra Demircioglu et al., 2016).

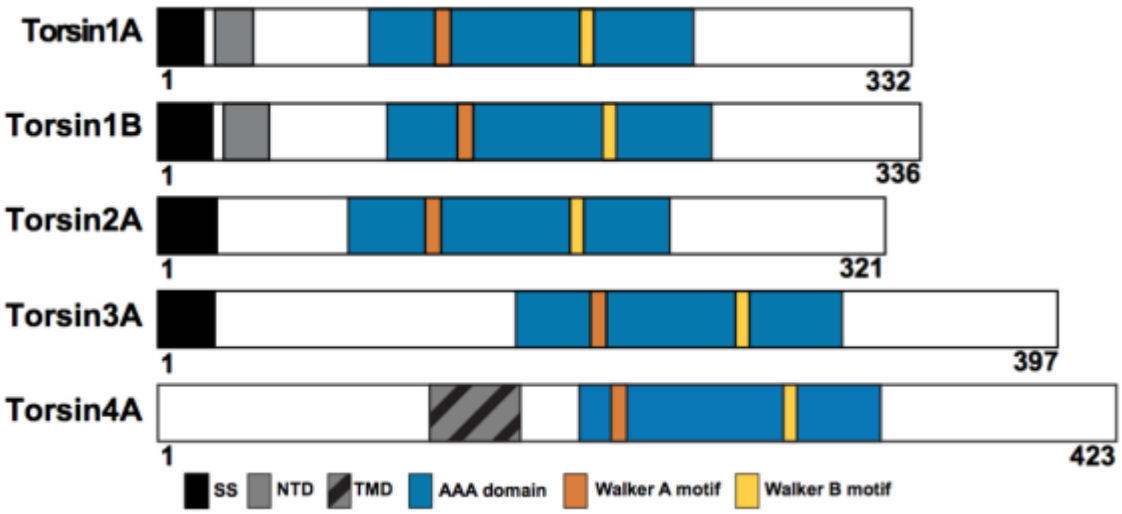

Figure 6: Schematic comparing human torsin domains and motifs. SS: Signal Sequence, NTD: N-terminal domain, TMD: Transmembrane domain, AAA: ATPase associated with various cellular activities

Torsin1A interacting partners are required for ATPase activity *in vitro*

Torsin1A has two major binding partners, Lamina Associated Polypeptide1 (LAP1) and Luminal Like Lap1 (LULL1), which are required for the ATPase activity of torsin1A (Zhao et al., 2013). LAP1 localizes to the INM, where it interacts with A-type nuclear lamins via its N-terminal domain (Goodchild et al., 2015; Goodchild and Dauer, 2005). LULL1 is found on the ONM and throughout the ER, and its N-terminus localizes to the cytosol. The C-terminal domain of LAP1 and LULL1 both extend into the lumen of the NE/ER and are 60% identical (Goodchild and Dauer, 2005).

The luminal domains of either LAP1 or LULL1 stimulate the ATPase activity of torsin1A several fold above background levels (Zhao et al., 2013). Recent crystal structures of the LAP1 and LULL1 luminal domains reveal that these proteins possess an AAA+ like fold, although they lack the ability to bind ATP themselves (Sosa et al., 2014; Esra Demircioglu et al., 2016). Furthermore, these luminal domains contain highly conserved arginine residues that stimulate the ATPase activity of torsin1A and torsin1B. Torsin2A has no ATPase activity with either LAP1 or LULL1, and torsin3A is not stimulated by LAP1 and only slightly stimulated by LULL1 (Zhao et al., 2013; Brown et al., 2014; Sosa et al., 2014).

The finding that LAP1 and LULL1 stimulate of the ATPase activity of torsin1A by providing an arginine finger led to a model for torsin1A activation, where torsin1A and LAP1/LULL1 form alternating heterohexameric ring-shaped structuture (Sosa et al., 2014; Brown et al., 2014; Rose et al., 2015). This model

allows for torsin1A ATPase activity to be stimulated by LAP1 or LULL1, depending upon the subcellular localization of torsin1A. An AAA+ protein forming a heterohexameric ring structure is not novel (Saffian et al., 2012; Gribun et al., 2008). However, having an ATP-binding AAA+ protein, like torsin1A, alternating with another protein that is unable to bind ATP, like LAP1/LULL1, is novel (Sosa et al., 2014).

Torsin1A has many cellular roles

Many cellular functions have been ascribed to torsin1A. Underscoring the importance of torsin1A, torsin1A null (torsin1A$^{-/-}$) mice die shortly after birth (Goodchild et al., 2005). At a cellular level, torsin1A plays a role in many processes, including asymmetric cellular division, neuronal migration, synaptic vesicle recycling and dopamine trafficking, Endoplasmic Reticulum Associated Degradation (ERAD) and centrosome orientation (Granata et al., 2009; McCarthy et al., 2012; Nery et al., 2011, 2014, Basham and Rose, 1999, 2001). Specifically within the nuclear envelope, torsin1A has been shown to be involved with nuclear envelope spacing, and the nuclear egress of Herpes simplex viruses and very large ribonucleic nuclear particles, called megaRNPs (Goodchild and Dauer, 2004; Goodchild et al., 2005; Maric et al., 2011; Speese et al., 2012). Torsin1A$^{-/-}$ neurons show INM blebs extending into the lumen of the NE, and expression of torsin1A with the Walker-B mutation causes the spacing between the INM and ONM to be much closer than in wild type conditions (Naismith et al., 2004).

Torsin1A and the LINC complex also have been shown to interact, with mutant torsin1A localization to the nuclear envelope dependent upon SUN1 (Jungwirth et al., 2011). Additionally, the localization of LINC complex components Nesprin-3, N2G, and SUN2 to the nuclear envelope are sensitive to torsin1A levels (Vander Heyden et al., 2009).

A better understanding of the mechanisms that control cellular polarity is critical for advancing our understanding of directed cell migration. Recent findings show that protein assemblies within the PNS, like the LINC complex, play important and critical roles during polarization and migration (Luxton et al., 2010; Stewart et al., 2015). However, the molecular mechanisms that control LINC complex assembly and TAN line formation are still nebulous and need more interrogation (Bone and Starr, 2016; Saunders and Luxton, 2016).

Chapter 2

Differential Oligomerization of SUN1 and SUN2 in Living Cells

This chapter was submitted as Jared Hennen[1★], Cosmo A. Saunders[2★], Joachim D. Mueller[1✚], and G.W. Gant Luxton[2✚] "Differential Oligomerization of SUN1 and SUN2 in Living Cells" to the journal eLife.

★Signifies equal contribution

✚Signifies co-corresponding authors

Cosmo A. Saunders generated all the constructs used in the paper and performed the experiments for figures 3B, 4B, 5B, 6B, 4S1B, 5S1B.

Synopsis

Linker of nucleoskeleton and cytoskeleton (LINC) complexes are conserved molecular bridges within the nuclear envelope that mediate mechanical force transmission into the nucleoplasm. The core of the LINC complex is formed by a translumenal interaction between the outer and inner nuclear membrane KASH and SUN proteins, respectively. Recent *in vitro* studies reveal that mammalian SUN2 is a trimer that recruits three KASH proteins. Here, we test the *in vivo* relevance and conservation of SUN protein trimerization using fluorescence fluctuation spectroscopy and brightness analysis. We show that SUN2 trimerizes within the nuclear envelope of living cells. We also reveal that the oligomerization of mammalian SUN1 within the nuclear envelope is not limited to a trimer, suggesting that this is not the sole arrangement for all SUN proteins. Finally, we uncover environment-dependent differences in SUN protein oligomerization suggestive of potential mechanisms for the regulation of LINC complex assembly.

INTRODUCTION

The nuclear envelope (NE) encloses the genome and defines the nuclear compartment in eukaryotic cells (Kite, 1913; Wilson and Dawson, 2011). The NE is composed of the nuclear membranes (inner nuclear membrane (INM), outer nuclear membrane (ONM) and pore membranes), the nuclear lamina, and nuclear pore complexes (NPCs) (Watson, 1955). The concentric INM and ONM are evenly separated by a ~30-50 nm perinuclear space (PNS) (Hatch and Hetzer, 2014). The ONM and PNS are contiguous with the ER lumen (Watson, 1955), whereas the INM contains a unique set of proteins that interact with the underlying nuclear lamina and chromatin (Burke and Stewart, 2014). While the majority of communication between the nucleus and cytoplasm occurs as regulated macromolecular transport via nuclear pore complexes (Knockenhauer and Schwartz, 2016), nuclear-cytoplasmic communication can also be mechanical in nature (Isermann and Lammerding, 2013; Jahed et al., 2014; Wang et al., 2009). For example, the forces generated by the cytoskeleton can be sensed and transmitted across the NE into the nucleoplasm by LINC complexes (Alam et al., 2014; Crisp et al., 2006; Luxton and Starr, 2014). These evolutionarily conserved molecular bridges span the INM, ONM and PNS and are critical for several fundamental cellular functions including cell division, DNA damage repair, meiotic chromosome pairing, and nuclear positioning (Chang et al., 2015b; Luxton and Starr, 2014; Meinke and Schirmer, 2015; Starr and

Fridolfsson, 2010)**.** An increasing number of human diseases are associated with defects in LINC complex function such as cerebellar ataxia, cancer, high frequency hearing loss, muscular dystrophy, cardiomyopathy, and neuropsychiatric disorders (Horn, 2014; Luxton and Starr, 2014; Saunders and Luxton, 2016).

LINC complexes are composed of two classes of type II membrane proteins, the ONM *Klarsicht*/*ANC-1*/*SYNE* homology (KASH) proteins (a.k.a. nesprins) and the INM *Sad1*/*UNC-84* (SUN) proteins (Crisp et al., 2006). The mammalian genome encodes six distinct KASH proteins (nesprin-1, -2, -3, -4, LRMP, and KASH5) and five distinct SUN proteins (SUN1-5) (Luxton and Starr, 2014; Meinke and Schirmer, 2015; Sosa et al., 2013). KASH proteins are defined by their conserved C-terminal KASH domain, which includes a trans-membrane domain (TMD) followed by the ~10-32 amino acid lumenal KASH peptide (Starr and Fischer, 2005; Starr and Han, 2002). The divergent N-terminal central rod domain (CRD) of KASH proteins extend away from the ONM into the cytoplasm where they engage various cytoskeletal elements and signaling molecules (Chang et al., 2015b; Kim et al., 2015; Luxton and Starr, 2014). SUN proteins are identified by the presence of the eponymous, C-terminal ~175 amino acid SUN domain that resides within the PNS (Malone et al., 1999; Tzur et al., 2006). The divergent SUN protein N-termini exist within the nucleoplasm where they interact

with A-type lamins, chromatin-binding proteins, and other INM proteins (Rothballer et al., 2013; Sosa et al., 2013; Starr and Fridolfsson, 2010). Recent

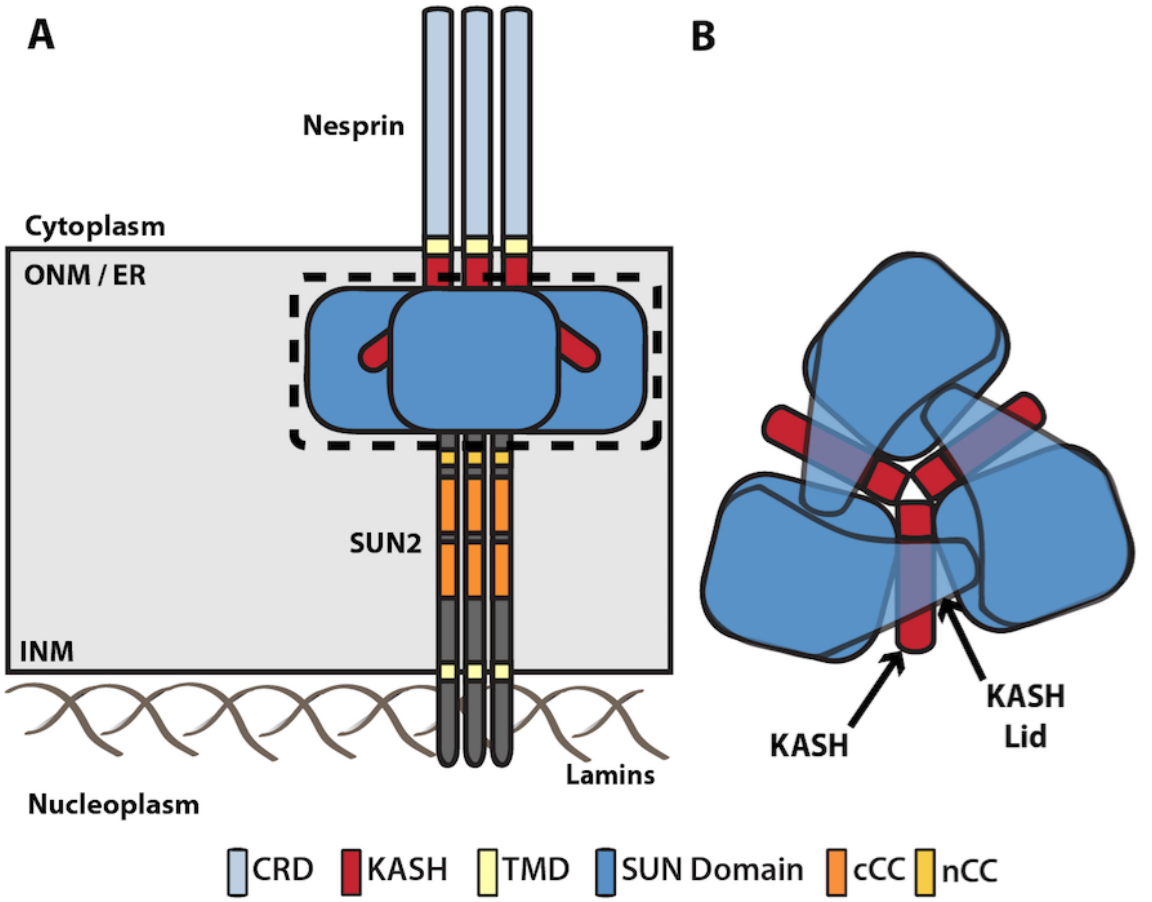

Figure 7: LINC complexes are hetero-hexameric molecular bridges composed of KASH and SUN proteins that span the NE. (A) Diagram of an assembled SUN2/nesprin hetero-hexamer, which is formed within the PNS of the NE by the direct interaction of three KASH peptides to domain interfaces of trimeric SUN proteins (Sosa et al., 2012; Wang et al., 2012; Zhou et al., 2012). (B) Top view of the SUN2 trimer bound to three KASH domains. A 20-residue antiparallel β sheet extension known as the KASH lid locks the KASH domain at the interface of SUN2 protomers (Sosa et al., 2012).

structural studies have revealed that human SUN2 trimerizes due to the presence of a canonical coiled-coil (cCC)-containing helical region within the luminal domain (LD) that may span the PNS from the inner leaflet of the ONM to the INM where it terminates in a TMD (Nie et al., 2016; Sosa et al., 2012; Wang et al., 2012; Zhou et al., 2012) (Figure 7A). In addition, a non-canonical coiled-coil (nCC) is found adjacent to the SUN domain (Sosa et al., 2012; Wang et al., 2012; Zhou et al., 2012). SUN2 trimerization creates deep hydrophobic grooves between neighboring SUN protomers, which recruit and stably interact with KASH peptides from nesprin-1 or nesprin-2 (Figure 7B). SUN2 further interacts with KASH peptides through a ~20 amino acid extension critical for KASH-binding known as the “KASH-lid”, which extends from one SUN protomer and clamps down over part of the KASH domain and a neighboring SUN protomer (Sosa et al., 2012) (Figure 7B). It is through the assembly of $(SUN\text{-}KASH)_3$ hetero-hexamers that LINC complexes can mechanically couple the nucleus to the cytoskeleton (Sosa et al., 2012; Wang et al., 2012). Despite these significant advances in our understanding of structural basis of mechanical nuclear-cytoskeletal coupling via the LINC complex, it is now critical that the *in vivo* relevance and conservation of the $(SUN\text{-}KASH)_3$ hetero-hexameric arrangement of LINC complexes are tested in living cells. As an initial step towards this goal, we decided to test the *in vivo* relevance and conservation of SUN protein trimerization using fluorescence fluctuation spectroscopy (FFS) and brightness analysis.

RESULTS

Quantification of protein-protein interactions within the NE of living cells by FFS and brightness analysis. FFS is a fluorescence microscopy technique that characterizes the mobility and stoichiometry of labeled proteins from the fluctuating fluorescence signal generated by these proteins as they pass through an optical observation volume created by the overlap of the two-photon beam spot and the sample (Macdonald et al., 2010; Slaughter and Li, 2010). Brightness analysis of these fluctuations monitors and quantifies protein association (Chen et al., 2003; Macdonald et al., 2013). To illustrate this concept, consider a fluorescently labeled protein that produces a “burst” of photons when it diffuses through the observation volume. The average photon count rate of these bursts identifies the brightness of the labeled protein. If this labeled protein dimerizes, it would produce on average twice as many photons as if it were a monomer since two fluorescing labels contribute to the fluctuating signal, leading to a doubling of the observed brightness (Chen et al., 2003). An additional z-scan of the two-photon spot through the cell was integrated into FFS to allow the investigation of thin sample volumes (Macdonald et al., 2010; Macdonald et al., 2013). Z-scan FFS and brightness analysis were previously used to study protein-protein interactions within the cytoplasm and at the plasma membrane (Fogarty et al., 2011; Macdonald et al., 2010; Smith et al., 2014; Smith et al., 2015a; Smith et al., 2015b).

Z-scan FFS experiments are carried out in two steps as previously described (Macdonald et al., 2010). First, the optical excitation spot generated by two-photon microscopy is moved axially through the center of a cell that expresses a fluorescently labeled protein (Figures 8A-B). The resulting axial fluorescence intensity profile or 'z-scan' characterizes the sub-cellular distribution of the fluorescent proteins along the length of the scan. Consequently, a fluorescently tagged protein that localizes to the NE produces a z-scan containing two peaks along the trajectory path, which correspond to signals produced by the fluorescent proteins found within the ventral and dorsal NEs, NE_V and NE_D, respectively (Figures 8B-C). Second, FFS is used to measure the intensity fluctuations of the fluorescently labeled proteins within the NE_V and NE_D after centering the two-photon spot on the respective peaks from the intensity profile (Figures 8D). Brightness analysis of the intensity fluctuations of the fluorescently labeled proteins provides a direct read-out of their average oligomeric state (Macdonald et al., 2010; Macdonald et al., 2013; Macdonald et al., 2014). For simplicity, we refer to the INM, ONM, and PNS collectively as the NE for the remainder of this work.

While z-scan FFS had been used successfully to characterize protein-protein interactions in the cytoplasm and at the plasma membrane of living cells (Macdonald et al., 2010; Smith et al., 2014; Smith et al., 2015a; Smith et al., 2015b), the NE was an unexplored environment for this experimental approach.

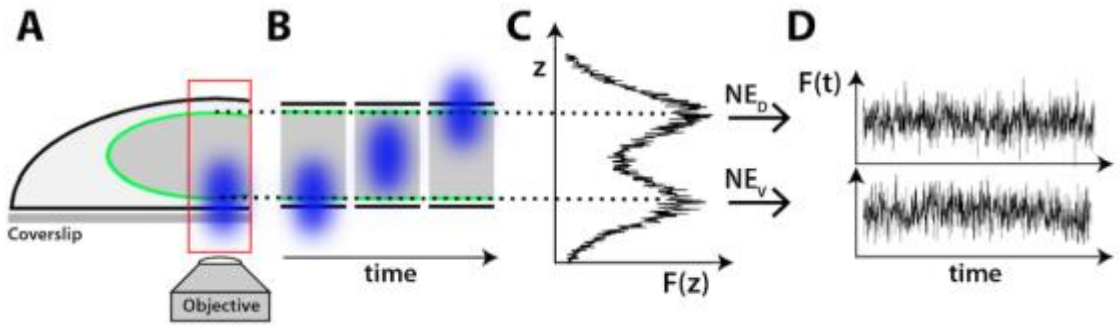

Figure 8: The application of Z-scan FFS to study protein interactions within the NE of living cells. (A) Diagram of a U2OS cell adhered to a glass coverslip that is expressing an EGFP-tagged protein that localizes to the NE (green ring around the grey nucleus), which is imaged by two-photon microscopy from below the coverslip surface. The two-photon spot (blue) does not reside entirely within the NE sample environment. **(B)** Diagram of the process of z-scan FFS where the two-photon spot is scanned axially over time through the center of the nucleus of a cell expressing a NE-localized EGFP-tagged protein. **(C)** A representative plot of the fluorescence intensity as a function of position along the z-axis for an NE-localized EGFP-tagged protein. The peak positions of the curve correspond to the location of the dorsal (NE_D) and ventral (NE_V) NEs as depicted by the dashed lines, which connect A-C. **(D)** The axial intensity scan in C is followed by a repositioning of the two-photon spot at either the NE_D or NE_V where the fluorescence intensity fluctuations are measured over time.

Therefore, we first measured the normalized brightness (*b*) of EGFP within the NE to determine the feasibility of z-scan FFS for quantitative brightness measurements within this unchartered sub-cellular compartment. EGFP is a robust reporter of brightness in the cytoplasm, nucleoplasm, and at the plasma membrane of living cells (Bag and Wohland, 2014; Chen et al., 2003; Chen et al., 2005; Macdonald et al., 2010; Macdonald et al., 2013; Macdonald et al., 2014; Smith et al., 2014; Smith et al., 2015a; Stahelin, 2013; Weidemann et al., 2014). To target EGFP to the ER lumen and PNS, we fused to its N-terminus the signal sequence (SS) of torsinA, which resides within the shared sub-cellular environment of the ER lumen and PNS (Hewett et al., 2003) (Figure 9A). An important control for the quantitative assessment of oligomerization by FFS is the demonstration of *b* doubling for a homo-dimeric protein complex (Chen et al., 2003; Macdonald et al., 2010). Therefore, we fused the torsinA SS to the N-terminus of a tandem dimeric EGFP construct, creating SS-EGFP$_2$ (Figure 9A). Both SS-EGFP and SS-EGFP$_2$ localized as expected to a reticular endomembrane system similar to that of the ER and NE when expressed in U2OS osteosarcoma cells (Figure 9B). Consistent with the localization of SS-EGFP to the NE, a typical z-scan intensity profile from a SS-EGFP-expressing U2OS cell exhibits two prominent peaks corresponding to the NE$_V$ and NE$_D$ (Figure 9C).

To obtain FFS measurements within the NE, the two-photon spot is centered on the dorsal and ventral NE by finding the corresponding intensity maximum in the z-scan intensity profile. However, accurate interpretation of FFS data and downstream brightness analyses within the NE requires quantitative knowledge of the fluorescence signal generated by fluorescent proteins present within the NE and other sub-cellular compartments such as the cytoplasm and nucleoplasm (Smith et al., 2014). To quantitatively analyze how much of the fluorescence at a given peak originates from the NE, the cell along the z-scan trajectory was modeled as a series of fluorescent layers with their associated intensity profiles. The axial intensity profile shown in Figure 9C suggests a minimal model where a nucleoplasmic layer separates the two NE layers. The thin cytoplasmic layer adjacent to the NE is ignored in this model, because its signal contribution is negligible. To describe the intensity profile of a geometry consisting of several layers, the intensity profile from each layer is summed (Smith et al., 2014). Fitting of the experimental intensity profile (NE Data, black line) to our three-layer model (NE Fit, solid orange line) demonstrates a good agreement between experiment and theory (Figure 9C). NE Fit is the superposition of the intensity profiles of the NE_V (short dashed green line) **and** NE_D (long dashed red line) layers together with the intensity profile of the nucleoplasmic layer (solid blue line) (Figure 9D). The separation of the intensity profile into the contributions from each layer illustrates that the fluorescence generated from the nucleoplasm is much less than what is generated from the NE (Figures 9C-D). Dividing the peak intensity

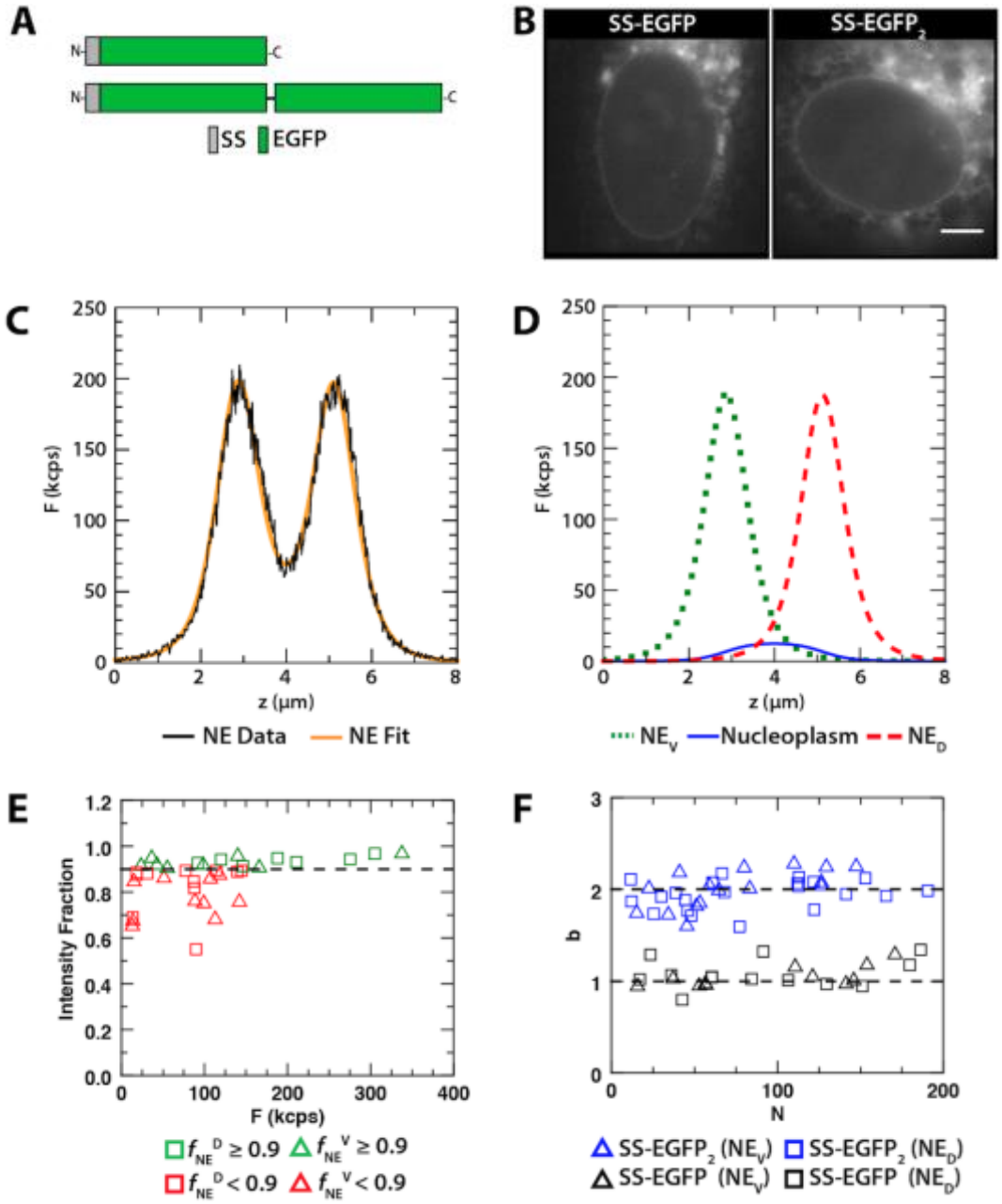

Figure 9: Demonstration of brightness doubling for a homo-dimeric protein complex within the NE.

Figure 9: Demonstration of brightness doubling for a homo-dimeric protein complex within the NE. (A) Diagram of the ER/NE lumen-targeted monomeric (SS-EGFP) and homo-dimeric (SS-EGFP$_2$) EGFP constructs used in this Figure. The EGFP proteins in SS-EGFP$_2$ are joined together by a 10 amino acid linker (black line). SS: torsinA signal sequence. **(B)** Representative wide-field epifluorescence images of either SS-EGFP or SS-EGFP$_2$ expression in the NE of living U2OS cells. Scale bar: 5 µm. **(C)** Experimental z-scan fluorescence intensity data (solid black curve) from a living U2OS cell expressing SS-EGFP. The fit (solid orange curve) of the intensity profiles to the three-layer model is in good agreement with the experimental data. **(D)** The fit from C determines the intensity profiles of the NE_D- and NE_V-layers as well as the intensity profile from the nucleoplasm. **(E)** Graph of the fraction of fluorescence intensity originating from the NE_D (f_{NE}^{D}, squares) and NE_V (f_{NE}^{V}, triangles) from z-scan measurements performed on multiple SS-EGFP-expressing U2OS cells. Cells with intensity fractions ≥ 0.9 (green) were subjected to brightness analysis, whereas those with intensity fractions < 0.9 (red) were removed from further analysis. **(F)** A Plot of *b* vs. *N* for SS-EGFP (black squares and triangles) and SS-EGFP$_2$ (blue squares and triangles) measured at either the NE_D (squares) or NE_V (triangles). Each data point represents the *b* measured in a different cell expressing either construct.

from the NE_V by the total intensity at the same location defines the intensity fraction from the NE_V. Repeating the same procedure at the dorsal location determines the intensity fraction from the NE_D. Calculating the intensity fractions of the z-scan data shown in Figure 3C demonstrated that 94% and 91% of the peak intensity are from the NE_V and NE_D, respectively. Reporting the intensity fractions from the z-scan measurements performed on multiple SS-EGFP-expressing U2OS cells as a function of the intensity at the NE reveals intensity fractions varying from ~0.55-0.95 (Figure 9E). Due to the lack of systematic differences between NE_V (triangles) and NE_D (squares) intensity fractions (Figure 9E), we refer to the intensity fraction independent of location from here on.

Partitioning of the fluorescence signal into NE and non-NE sources (Figure 9D) provides essential information for the unbiased evaluation of brightness from a thin sample layer in the presence of contaminating outside contributions (Smith et al., 2014). However, since the procedure is labor-intensive and time-consuming, it is advantageous to select cells that require no such correction. Application of our previously described theoretical model for z-scan FFS of multiple layers (Smith et al., 2014) predicts that the contamination contributed by fluorescence from non-NE sources is < 10% for cells with an intensity fraction of NE over total fluorescence ≥ 0.9. Since the standard deviation of *b* measurements in cells is ~10% (Hur et al., 2014), the bias introduced by non-NE

sources is negligible, provided the NE fluorescence intensity fraction is ≥ 0.9 (Figure 9E, dashed black line).

Nearly 50% of SS-EGFP-expressing U2OS cells satisfied the intensity fraction requirement and were selected for *b* measurements (green shapes, Figure 9E). The remaining cells were not measured further (red shapes, Figure 9E). For the remainder of this study, only cells that met this requirement were analyzed. The *b* and number concentration (*N*) were calculated from the collected FFS data, which reflects the average number of EGFP labels within the optical observation volume and can be converted into a molar concentration provided the observation volume is known. Because the thickness of the NE layer is unknown, the observation volume cannot be accurately calculated. Therefore, we report *b* as a function of *N*, which is proportional to the molar concentration. The mean and standard deviation of *b* obtained from all measured SS-EGFP-expressing U2OS cells was 1.06 ± 0.14 independent of *N* (Figure 9F), which is within the experimental uncertainty consistent with SS-EGFP being monomeric within the NE. Mean and standard deviation *b* values of SS-EGFP measured at the NE_V (1.05 ± 0.11) and NE_D (1.08 ± 0.16) were statistically indistinguishable (Figure 9F).

To test our ability to quantitatively assess oligomerization by FFS within this sub-cellular compartment, we sought to replicate *b* doubling for a previously

described homo-dimeric EGFP construct, $EGFP_2$, within the NE (Chen et al., 2003; Macdonald et al., 2014). The expression of this construct was targeted to the contiguous ER lumen and PNS of the NE by fusing the SS of torsinA to $EGFP_2$, generating SS-$EGFP_2$ (Figure 9A). Z-scan measurements performed at the NE_V and NE_D of SS-$EGFP_2$-expressing U2OS cells with NE intensity fractions ≥ 90% revealed a mean *b* and standard deviation of 1.98 ± 0.18 that was independent of *N* (Figure 9F). This result demonstrates *b* doubling for SS-$EGFP_2$ in the NE. The mean and standard deviation *b* values of SS-$EGFP_2$ measured at the NE_V (2.01 ± 0.21) and NE_D (1.95 ± 0.16) were statistically indistinguishable (Figure 9F). Since the *b* values for SS-EGFP and SS-$EGFP_2$ were not influenced detectably by whether or not they were obtained from the NE_V or NE_D, *b* will be reported without reference to the location where they were measured within the NE. The results obtained for SS-EGFP and SS-$EGFP_2$ establish the feasibility of quantitative brightness measurements in the NE. Throughout the remainder of this manuscript, all the *b* data reported from z-scan FFS measurements performed in the NE were obtained using the measurement protocol described above.

Quantification of SUN2 oligomeric states within the NE. Having established that z-scan FFS and brightness analysis could be used to study protein-protein interactions within the NE of living cells, we turned our attention towards SUN2. Initially, we attempted to measure the oligomerization of a previously described

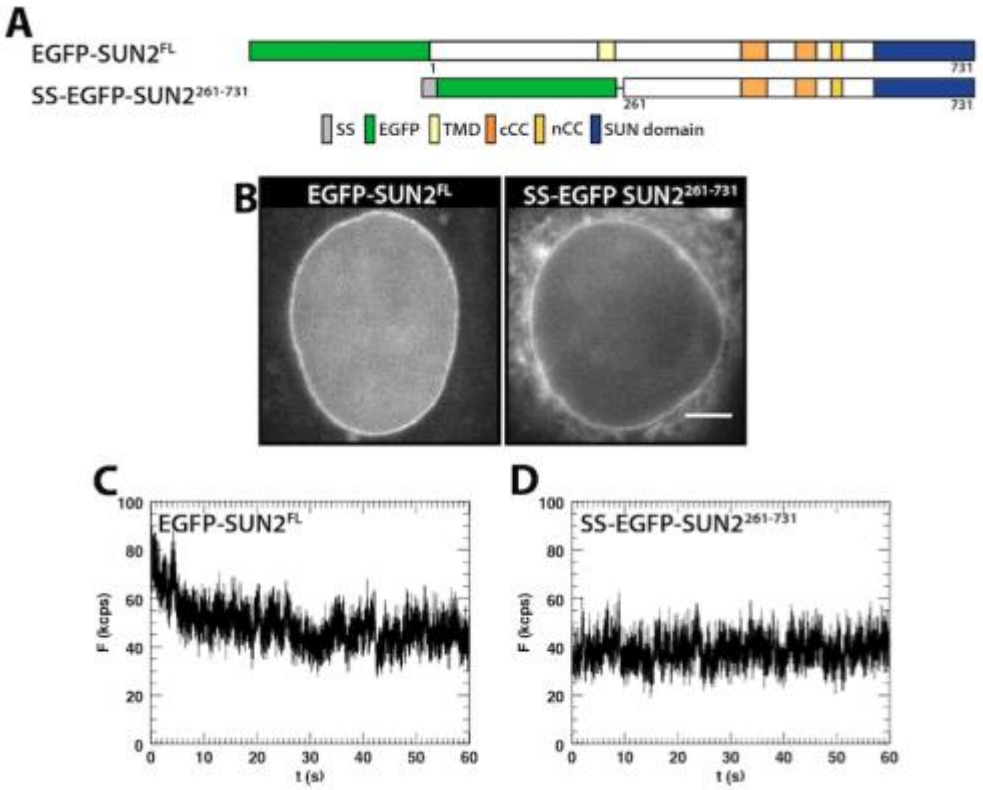

Figure 10: EGFP-SUN2FL is refractory to z-scan FFS and brightness analysis due to photobleaching. (A) Diagram of the SUN2 constructs used in this Figure. (B) Representative wide-field epifluorescence images of EGFP fluorescence in living U2OS cells expressing the indicated constructs. Scale bar: 5 µm. (C) Fluorescence intensity (solid black curve) of EGFP-SUN2^{FL} decays as a function of time measured in the NE of a U2OS cell. (D) Fluorescence intensity (solid black curve) of SS-EGFP-SUN2$^{216-731}$ measured in the NE of a U2OS cell remains stable.

functional EGFP-tagged full-length (FL) SUN2 construct (EGFP-SUN2^{FL}, Figure 10A) (Luxton et al., 2010; Östlund et al., 2009). However, EGFP-SUN2^{FL} is known to have low diffusional mobility due to the fact that it interacts with A-type nuclear lamins within the nucleoplasm (Östlund et al., 2009). Sufficiently low mobility leads to photobleaching in FFS experiments, which interferes with brightness analysis (Hur et al., 2014). Thus, we generated a SS-EGFP-tagged SUN2 construct that encodes the entire LD of SUN2 (SUN2^{LD}) not including the TMD (SS-EGFP-SUN2$^{261-731}$, Figure 10A). Consequently, this construct, like the SUN constructs used throughout this work, will not be constrained by membrane-association and will therefore be able to diffuse throughout the ER lumen and PNS. Following expression in U2OS cells, both EGFP-SUN2^{FL} and SS-EGFP-SUN2$^{261-731}$ localized to an endomembrane system reminiscent of the peripheral ER and NE (Figure 10B). As expected, EGFP-SUN2^{FL} was more enriched at the NE than SS-EGFP-SUN2$^{261-731}$, which was more diffuse throughout the ER (Figure 10B). We observed significant photobleaching of EGFP-SUN2^{FL} (Figure 10C), whereas SS-EGFP-SUN2$^{261-731}$ was unaffected (Figure 10D). Since the immobile nature of EGFP-SUN2^{FL} precludes quantitative FFS analysis, we focused our efforts on studying the oligomerization of the SUN2 LD (SUN2^{LD}) within the NE.

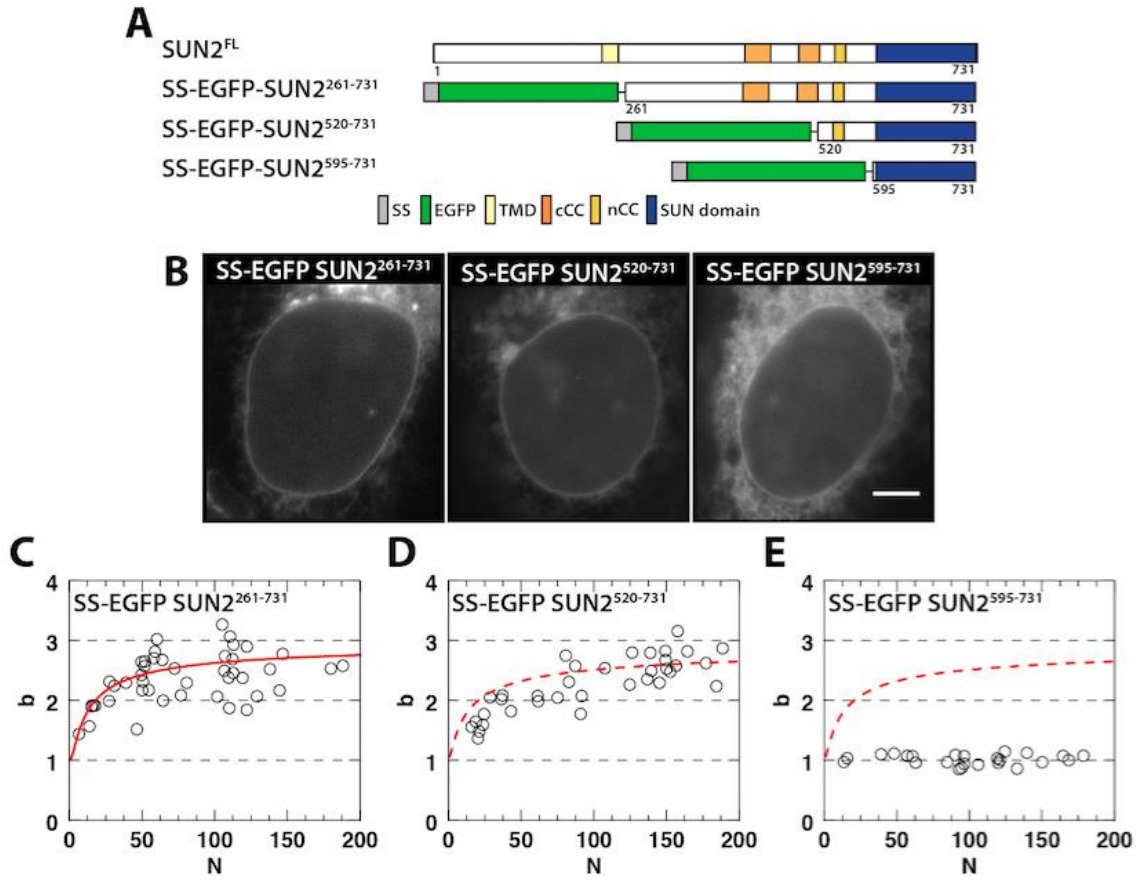

Figure 11: SUN2 trimerizes within the NE. (A) Diagram of the SUN2 constructs used in this figure. (B) Representative wide-field epifluorescence images of EGFP fluorescence in the NE of living U2OS cells expressing the indicated constructs from A. Scale bar: 5 μm. (C-E) Plots of *b* vs. *N* for the indicated constructs measured in the NE. The data in C are fit (solid red curve) to a monomer/dimer/trimer binding model, which is then shown in D and E (dashed red curve) to allow for comparison between the constructs. The fitted dissociation coefficients are $K_{MD} = 4100^{+5900}_{-4000}$ and $K_{DT} = 0.06^{+3}_{-0.04}$.

In addition to SS-EGFP-SUN2$^{261-731}$, we generated two truncated constructs SS-EGFP-SUN2$^{520-731}$ and SS-EGFP-SUN2$^{595-731}$, which encode the nCC through the SUN domain and the SUN domain alone, respectively (Figure 11A). Similar to SS-EGFP-SUN2$^{261-731}$, both SS-EGFP-SUN2$^{520-731}$ and SS-EGFP-SUN2$^{595-731}$ localized throughout the peripheral ER and NE following expression in U2OS cells (Figure 11B). The FFS intensity traces measured at the NE were free of photobleaching, which permitted us to perform brightness analysis (data not shown). Plotting the *b* vs. *N* from measurements performed in multiple U2OS cells expressing SS-EGFP-SUN2$^{261-731}$ (*n* = 30) revealed a concentration-dependent increase in *b* with values mainly between two and three for $N > 50$ (Figure 11C). These data indicate that SS-EGFP-SUN2$^{261-731}$ exhibits an average oligomerization state that is between a dimer and a trimer. While the *b* binding curve has not yet achieved saturation within the experimentally accessible concentration range, the data are approaching the next integer *b* of three, which would suggest a limiting trimeric stoichiometry for SS-EGFP-SUN2$^{261-731}$. A fit (solid line, Figure 11C) to a simple binding curve for monomer/dimer/trimer equilibrium is consistent with the *b* data obtained for this construct. The fitted dissociation coefficients K_{MD} = 4100 and K_{DT} = 0.06 in units of *N* for the monomer/dimer and dimer/trimer reaction indicate that the dimer population is a minority species since the monomer/dimer interaction is much weaker than the dimer/trimer interaction. Thus, the *b* binding curve can also be modeled by a monomer/trimer equilibrium (Figure 12, solid green line).

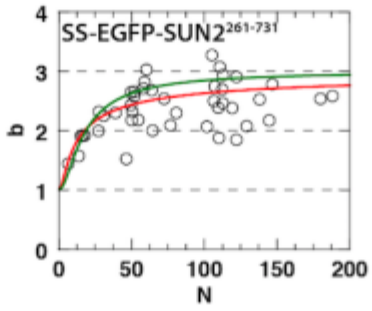

Figure 12: A monomer/trimer binding reaction is sufficient to describe the b binding curve of SS-EGFP-tagged SUN2$^{216-731}$ within the NE. The red line is a fit of the experimental *b* data (circles) to the monomer/dimer/trimer equilibrium model shown in Figure 4C. The green curve represents the fit to a monomer/trimer model with a dissociation coefficient K_{MT} = 26 ± 7.

The *b* values measured for SS-EGFP-SUN2$^{520-731}$ increase with *N* and approach three at high *N* values (Figure 11D). The *b* binding curve (dashed line) for SS-EGFP-SUN2$^{261-731}$ is shown to facilitate comparison of the two constructs. While the *b* data reported for SS-EGFP-SUN2$^{520-731}$ are on average slightly below the binding curve for $N < 100$, the differences are remarkably small. Unlike either SS-EGFP- SUN2$^{261-731}$ or SS-EGFP-SUN2$^{520-731}$, the *b* values obtained for SS-EGFP-SUN2$^{595-731}$ remain close to one and do not increase with concentration (Figure 11E). These results demonstrate that SUN2 trimerizes within the NE of living cells and that the SUN domain is not sufficient for this oligomerization, which is in agreement with previously reported *in vitro* studies (Sosa et al., 2012; Zhou et al., 2012).

Quantification of SUN1 oligomeric states within the NE. To address the conservation of SUN protein trimerization, we turned our attention to the mammalian SUN1 protein. We first compared the feasibility of using a previously described functional EGFP-tagged SUN1^{FL} construct (EGFP-SUN1^{FL}, Figure 13A) (Luxton et al., 2010; Östlund et al., 2009) for our z-scan FFS measurements. However, since SUN1 is also relatively immobile due to interactions with A-type lamins (Östlund et al., 2009), we again found that photobleaching was problematic. Thus we generated a SS-EGFP-tagged SUN1 LD (SUN1^{LD}) construct analogous to SS-EGFP-SUN2$^{261-731}$ (SS-EGFP-SUN1$^{457-913}$, Figure 13A). Following expression in U2OS cells, both EGFP-

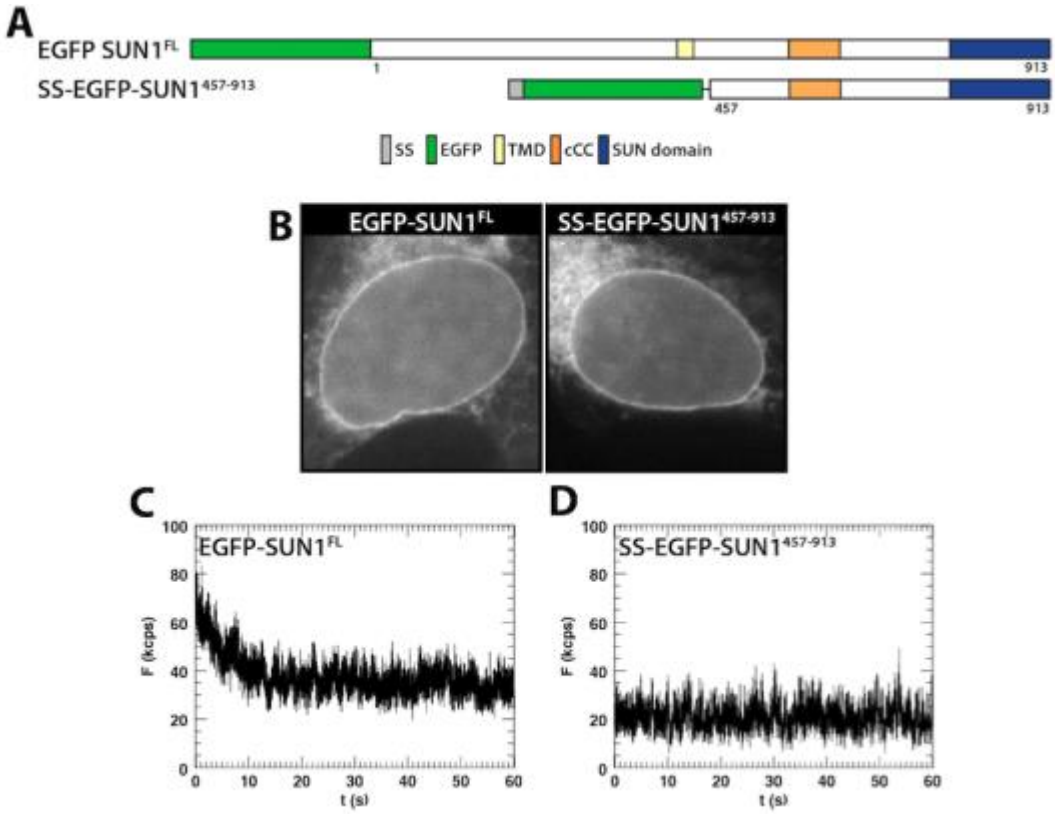

Figure 13: Full-length EGFP-tagged SUN1 is refractory to z-scan FFS and brightness analysis due to photobleaching. (A) Diagram of the SUN1 constructs used in this figure. (B) Representative wide-field epifluorescence image of EGFP fluorescence in living U2OS cells expressing the indicated constructs. Scale bar: 5 μm. (C) Fluorescence intensity (solid black curve) of EGFP-SUN1^{FL} decays as a function of time measured in the NE of a U2OS cell. (D) Fluorescence intensity (solid black curve) of SS-EGFP-SUN1$^{457-913}$ measured in the NE of a U2OS cell remains stable.

SUN1^{FL} and SS-EGFP-SUN1$^{457-913}$ localized as expected to the peripheral ER and NE (Figure 13B). Again, the FL construct was highly immobile and susceptible to photobleaching (Figure 13C), whereas the LD construct was unaffected (Figure 13D). Thus, we focused our efforts on studying the oligomerization of the SUN1^{LD} within the NE.

Because of the lack of structural information regarding the exact location and number of coiled-coil (CC) domains in SUN1, we limited our analysis to one additional SS-EGFP-tagged SUN1^{LD} construct, which encodes only the SUN domain (SS-EGFP-SUN1$^{777-913}$, Figure 14A). Both SS-EGFP-SUN1$^{457-913}$ and SS-EGFP-SUN1$^{777-913}$ localized to the peripheral ER and NE following expression in U2OS cells (Figure 14B). The *b* of SS-EGFP-SUN1$^{457-913}$ increased over the entire range of *N* (Figure 14C). However, the data obtained for this construct cannot be fit to a binding curve because its *b* increased in an approximately linear fashion with *N* without a clearly detectable decrease in the slope. The straight red line through the data serves to guide the eye and for future comparison with the *b* data from SS-EGFP-SUN1$^{777-913}$. We cannot estimate the stoichiometry of SS-EGFP-SUN1$^{457-913}$, because the *b* data did not exhibit a trend towards a limiting value. Nevertheless, the highest *b* value that we measured was approximately five for SS-EGFP-SUN1$^{457-913}$ indicating the presence of higher-order oligomeric states than what we observed for SS-EGFP-SUN2$^{261-731}$. In contrast, the *b* of SS-EGFP-SUN1$^{777-913}$ was independent of *N*

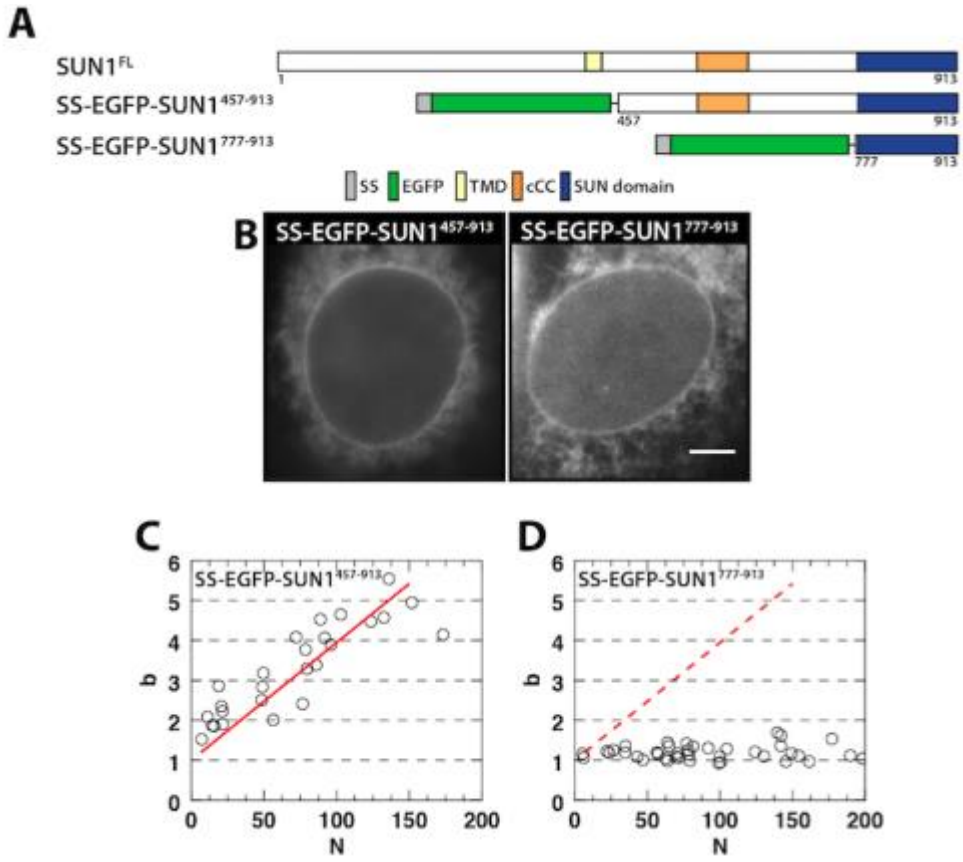

Figure 14: SUN1 assembles higher-order oligomers within the NE. (A) Diagram of the SUN1 constructs used in this Figure. (B) Representative wide-field epifluorescence images of EGFP fluorescence in the NE of living U2OS cells expressing the indicated constructs from A. Scale bar: 5 μm. (C and D) Plots of *b* vs. *N* for the indicated constructs measured in the NE. The data in C are fit (solid red line) to a linear regression, which is then shown in D (dashed red line) to allow for comparison between the constructs.

with a value close to one (Figure 14D). These results suggest that SUN1 can form higher-order oligomers than SUN2

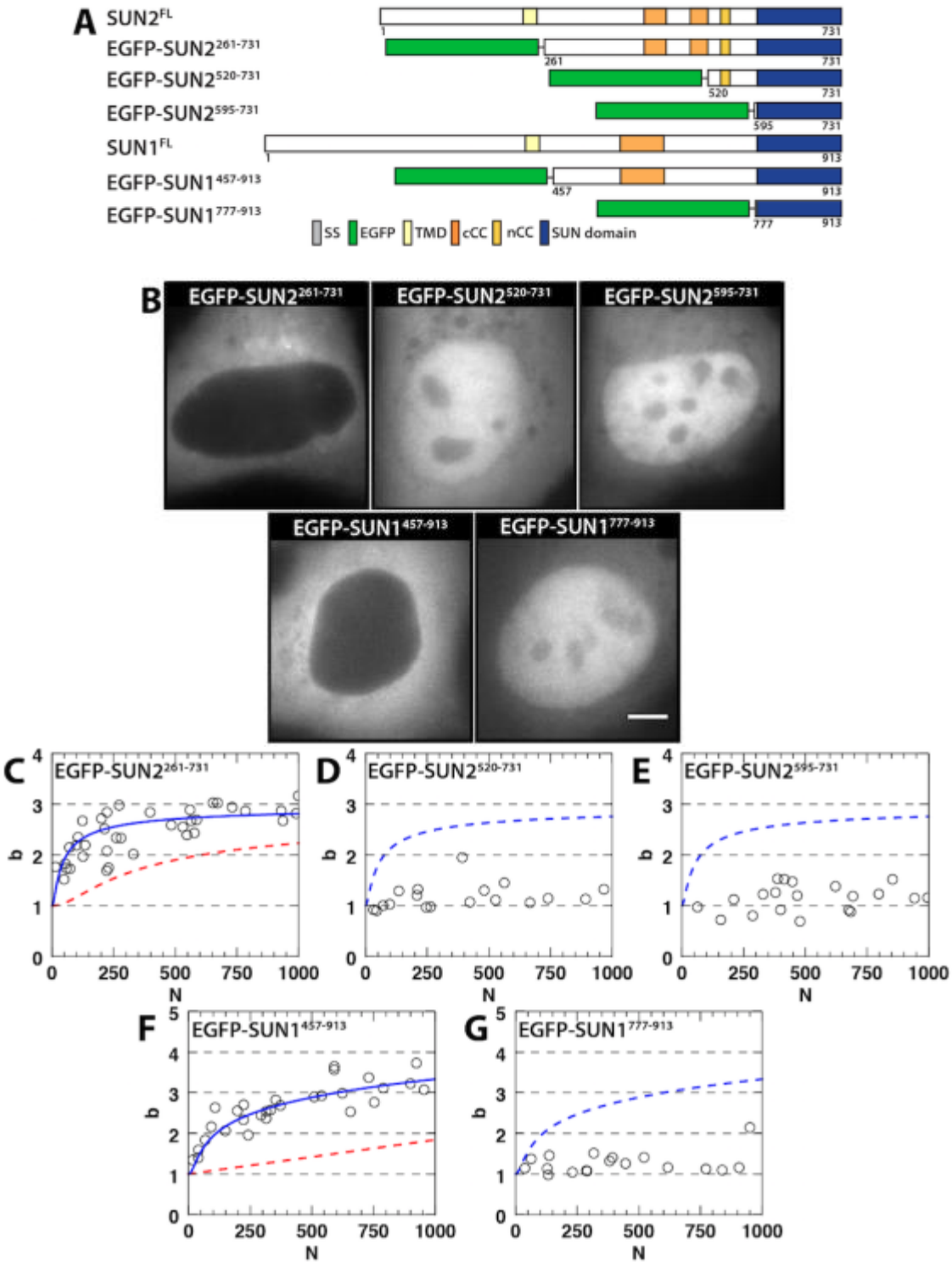

Figure 15: SUN1 and SUN2 oligomerization within the cytoplasm.

Figure 15: SUN1 and SUN2 oligomerization within the cytoplasm. (A) Diagram of the SUN constructs used in this figure. **(B)** Representative wide-field epifluorescence images of EGFP fluorescence in living U2OS cells expressing the indicated constructs from A. Scale bar: 5 μm. **(C-G)** Plots of the *b* vs. *N* for the indicated constructs measured in the cytoplasm. The data in C are fit to a trimeric binding model (solid blue curve), which is then shown in D and E (dashed blue curve) to allow for comparison between the SUN2 constructs. The dissociation coefficients for EGFP-SUN2$^{261\text{-}731}$ are K_{MD} = 8000 ± 4000 and K_{DT} = 0.3 ± 0.2. The data in F are fit to a monomer/trimer/hexamer binding model with calculated dissociation coefficients K_{MT} = 100 ± 60 and K_{TH} = 1500 ± 400, which is then shown in G (dashed blue curve) to allow for comparison between the SUN1 constructs. The estimated binding curves (dashed red curve) for the data obtained in the NE for the SS-EGFP-SUN2$^{261\text{-}731}$ and SS-EGFP-SUN1$^{457\text{-}913}$ are presented in C and F, respectively.

within the NE of living cells, indicating the presence of additional interactions not present in SUN2.

Quantification of SUN1 and SUN2 oligomerization within the cytoplasm. To determine if the environment of the NE influenced the oligomerization of SUN1 and/or SUN2, we performed FFS measurements and subsequent brightness analyses of EGFP-tagged versions of the $SUN1^{LD}$ and $SUN2^{LD}$ constructs described above in the cytoplasm of U2OS cells. Cytoplasmic expression was achieved by removal of the torsinA SS from the aforementioned constructs (Figure 15A). Each of the EGFP-$SUN1^{LD}$ and -$SUN2^{LD}$ constructs localized throughout the cytoplasm and the nucleoplasm of the expressing U2OS cells, save for EGFP-$SUN1^{457-913}$ and EGFP-$SUN2^{261-731}$, which were solely found within the cytosol (Figure 15B). To measure the oligomeric states of these constructs within the cytoplasm, FFS experiments were performed by focusing the two-photon spot into the cytoplasm of U2OS cells expressing the above indicated EGFP-tagged SUN protein LD constructs and analyzed as previously described (Macdonald et al., 2010; Macdonald et al., 2013). The *b* of EGFP-$SUN2^{261-731}$ in the cytoplasm increased with *N* and appeared to reach a limiting value of three at $N > 600$ (Figure 15C). This result indicates the presence of trimeric protein complexes and agrees with the estimated stoichiometry of the protein we observed in the NE. A fit of the cytosolic *b* data measured for cytoplasmic EGFP-$SUN2^{261-731}$ to a trimeric binding curve (solid blue line) is

shown with monomer/dimer and dimer/trimer dissociation coefficients K_{MD} = 8000 and K_{DT} = 0.3, respectively (Figure 15C). Because K_{DT} is much higher than K_{MD}, the dimer population is negligible and a monomer/trimer equilibrium is sufficient to describe the *b* binding curve for EGFP-SUN2$^{261-731}$ (Figure 16A).

A direct comparison of the cytoplasmic *b* binding curve with the NE *b* binding curve is not feasible because the *N* of both experiments is referenced to different effective observation volumes. While the observation volume in the cytoplasm can be experimentally determined (Macdonald et al., 2013), no such procedure exists for the NE. Nevertheless, we can estimate the NE observation volume by multiplying the areal cross section of the two-photon spot with the thickness of the NE. Assuming a PNS thickness of 40 nm (Franke et al., 1981), we arrive at an effective volume of 6.9 10^{-3} fl, which is 34-fold smaller than the observation volume in the cytoplasm. Thus, by multiplying *N* in the NE by 34 we compensate for the difference in observation volume and obtain a cytoplasmic number concentration *N*. We applied this procedure to the trimeric *b* binding curve in the NE to create the predicted *b* binding curve in the cytoplasm (red dashed line, Figure 15C). A comparison of these two curves demonstrates that the observed *b* increase with *N* in the cytoplasm is significantly more pronounced than what was observed in the NE. In contrast, both EGFP-SUN2$^{520-731}$ and EGFP-SUN2$^{595-731}$ appeared to be monomeric within the cytoplasm as their *b* values remained near one (Figures 15E-F). These results show that while SUN2$^{261-731}$

and SUN2$^{595-731}$ reached the same limiting oligomeric states in both the cytoplasm and NE, only the binding curve of SUN2$^{261-731}$ displayed a concentration-dependence that was environment-dependent. In addition, these results demonstrate a dramatic environmental dependence on the oligomerization of SUN2$^{520-731}$ with it reaching a limiting trimeric state in the NE at high *N* values and remaining monomeric regardless of concentration in the cytoplasm.

Differences in the behavior of the EGFP-tagged SUN1$^{457-913}$ constructs in the cytoplasm relative to the NE were also observed. While the *b* of SS-EGFP-SUN1$^{457-913}$ and EGFP-SUN1$^{457-913}$ rises with increasing *N*, the *b* increase of EGFP-SUN1$^{457-913}$ within the cytoplasm slows at higher concentrations unlike the linear increase with *N* we observed in the NE (Figure 15F). To further compare these results, we graphed the linear trend line (red dashed line) for the *b* of SS-EGFP-SUN1$^{457-913}$ in the NE with converted *N* on the graph reporting the *b* of EGFP-SUN1$^{457-913}$ in the cytosol (Figure 15F). This comparison clearly shows that the *b* of this SUN1^{LD} construct in the cytoplasm rises much faster than in the NE (Figure 15F). Unlike EGFP-tagged SUN2$^{261-731}$, EGFP-tagged SUN1$^{457-913}$ does not reach the same *b* levels in the cytoplasm as in the NE (Figure 15F). Instead, the *b* data slightly exceed 3 in the cytoplasm at high *N* values. A fit of the *b* values to a monomer/dimer/trimer binding model reveals that the tail of the binding curve ($N > 500$) is not reproduced by the model (Figure 16B). This misfit

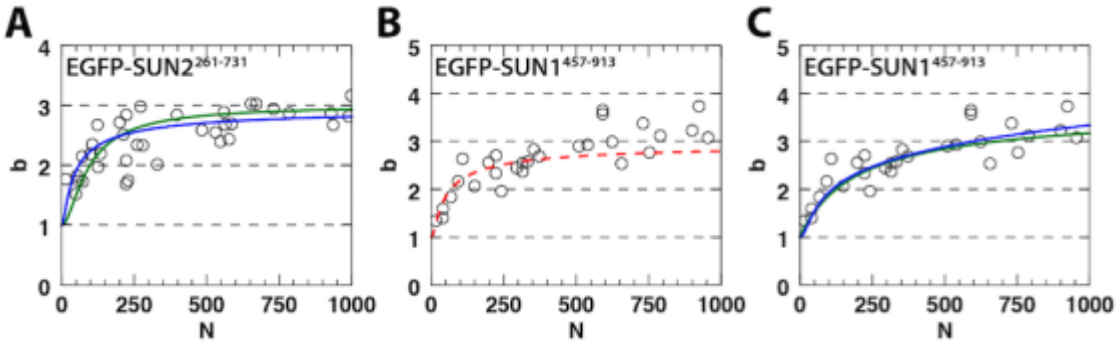

Figure 16: Cytoplasmic b binding curves of EGFP-SUN2$^{261-731}$ and EGFP-SUN1$^{457-913}$ fit to different binding models. (A) The blue curve is a fit of the experimental *b* data generated for EGFP-SUN2$^{261-731}$ (circles) to the monomer/dimer/trimer equilibrium binding model shown in Figure 6C. The green curve represents the fit of this data to a monomer/trimer binding model with a monomer/trimer dissociation coefficient K_{MT} = 130 ± 9. (B) The dashed red curve is a fit of the experimental *b* data generated for EGFP-SUN1$^{457-913}$ (circles) to a monomer/dimer/trimer binding model. (C) The blue curve is a fit of the experimental *b* data generated for EGFP-SUN1$^{457-913}$ (circles) to the monomer/trimer/hexamer equilibrium binding model shown in Figure 6F. The green curve represents the fit of this data to a monomer/dimer/tetramer binding model with a monomer/dimer dissociation coefficient K_{MD} = 110 ± 30 and a dimer/tetramer dissociation coefficient K_{DT} = 90 ± 30.

implies the need for at least one stoichiometric state in excess of a trimer for EGFP- SUN1$^{457-913}$ in the cytoplasm. A monomer/trimer/hexamer binding model (blue curve) was sufficient to describe the experimental data (Figure 15F). However, other models can also reproduce the brightness data as demonstrated by fitting the data in Figure 15F to a monomer/dimer/tetramer equilibrium (Figure 16C). This model was suggested by recent biochemical results indicating the existence of SUN1 dimers and tetramers (Lu et al., 2008). Currently, the experimental data cannot distinguish between these different binding models. Finally, the *b* of EGFP-SUN1$^{777-913}$ remains close to one over the measured concentration range (Figure 15G), in agreement with the behavior observed for SS-EGFP-SUN1$^{777-913}$ in the NE environment (Figure 14D).

We observed a more pronounced *N*-dependent brightness increase for EGFP-tagged SUN2$^{261-731}$ and SUN1$^{457-913}$ in the cytoplasm that in the NE when referenced to the same observation volume (Figures 15C and F). A potential explanation for these results could be the presence of unlabeled endogenous SUN proteins within the NE that compete with these labeled SUN constructs, leading to the assembly of protein complexes containing a mixture of labeled and unlabeled SUN proteins and ultimately a reduction in the measured *b*. However, once the exogenously expressed EGFP-tagged protein concentration becomes high enough, the presence of the endogenous population becomes negligible

and the limiting *b* is unchanged (Chen and Mueller, 2007). Thus, we performed modeling to test whether the existing data are compatible with the concept of endogenous competition. To do this, we fit the SS-EGFP-SUN2$^{261-731}$ *b* data generated in the NE to the cytoplasmic monomer/dimer/trimer binding model while including unlabeled endogenous SUN protein with the same binding affinity as the labeled protein. The dissociation coefficients from the cytoplasmic fit were divided by 34 to account for the reduced observation volume in the NE. The fit demonstrates that the experimental SS-EGFP-SUN2$^{261-731}$ data are consistent with the model of endogenous competition for a number concentration of N = 17 ± 2 for the unlabeled protein (Figure 17A). Next, we applied the same procedure to the SS-EGFP-SUN1$^{457-913}$ *b* data taken in the NE using the cytosolic dissociation coefficients of the monomer/trimer/hexamer model divided by 34. The best fit resulted in an unlabeled number concentration of N = 9 ± 2, which closely reproduced the SS-EGFP-SUN1$^{457-913}$ *b* data, except at high concentrations, where the fit underestimates the experimental *b* values (Figure 17B). The discrepancy between model and data potentially hints at the presence of higher oligomeric states not covered by the monomer/trimer/hexamer model. It is not surprising that the cytoplasmic binding model would fail to describe such states for SS-EGFP-SUN1$^{457-913}$, because our cytoplasmic measurements for EGFP-SUN1$^{457-913}$ only covered number concentrations N < 1000, which corresponds to effective NE concentration of N < 30 (blue solid curve, Figure 17B). The fitted binding curve at higher values of N (blue dashed curve, Figure

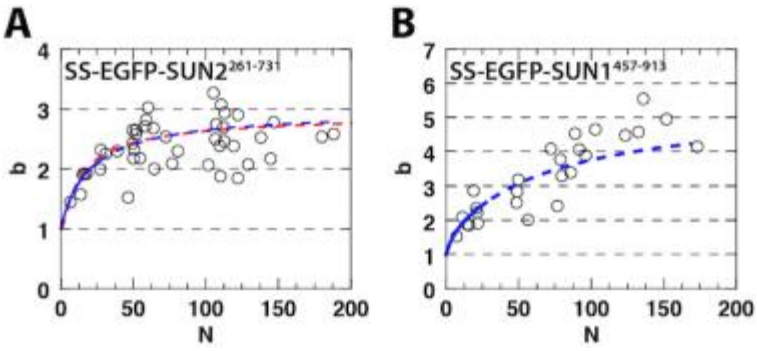

Figure 17: Modeling the contribution of endogenous unlabeled SUN proteins on the b binding curves of EGFP-tagged SUN proteins within the NE. (A) The dashed red curve is the fit of the experimental *b* data generated for SS-EGFP-SUN2$^{261-731}$ (circles) to the monomer/dimer/trimer equilibrium binding model shown in Figure 4C. The blue curve is a fit of this data using the dissociation coefficients of the cytoplasmic monomer/dimer/trimer binding model (Figure 6C) divided by 34. The fit included unlabeled endogenous SUN protein (N = 17 ± 2) with the same binding affinity as the labeled protein. (B) The blue curve is fit of the experimental *b* data generated for EGFP-SUN1$^{457-913}$ (circles) using the dissociation coefficients of the cytoplasmic monomer/trimer/hexamer binding model (Figure 6F) divided by 34. The fit included unlabeled endogenous SUN protein (N = 9 ± 2) with the same binding affinity as the labeled protein. The solid blue line represents the equivalent NE concentration range of the binding data directly observed in the cytoplasm (N < 1000) and accounts for the 34-fold difference in number concentration between the two environments. The dashed blue line depicts an extrapolation of the cytoplasmic binding model to higher concentrations.

17B) represents an extrapolation of the cytoplasmic binding model and is unable to predict new interactions that occur in the extrapolated concentration domain.

Thus, endogenous competition of SUN proteins with SS-EGFP-SUN2$^{261-731}$ and SS-EGFP-SUN1$^{457-913}$ is able to explain the relatively weaker interactions observed in the NE as compared to the cytoplasm (Figures 15C and F), provided we postulate the existence of SS-EGFP-SUN1$^{457-913}$ oligomers that exceed the states accessible by the monomer/trimer/hexamer model. These results provide a prediction for the endogenous concentration that can be tested in future experiments in order to assess if environmental effects modulate the binding interactions of SUN proteins. Moreover, we want to emphasize that the inability of EGFP-SUN2$^{520-731}$ to oligomerize within the cytoplasm while the related SS-EGFP-SUN2$^{520-731}$ construct trimerizes within the NE (Figure 15D) cannot be attributed to endogenous competition, because the brightness in the NE exceeds the brightness in the cytoplasm. Consequently, our data imply the existence of previously unidentified regulators of SUN protein oligomerization within the NE.

DISCUSSION

In this work, we tested the *in vivo* relevance and conservation of SUN protein trimerization. We provide evidence for the existence of SUN2 trimers within the PNS and that the LD is critical for its oligomerization, which is in agreement with

in vitro structural studies (Nie et al., 2016; Sosa et al., 2012; Wang et al., 2012). We demonstrate that the related SUN1 protein also oligomerizes within the NE of living cells; however, SUN1 forms higher-order oligomers than SUN2 suggesting that trimers are not the limiting assembly state for all SUN proteins. In addition, we identify environment-dependent differences in SUN protein oligomerization between the cytoplasm and NE. Since not all of these differences can be attributed to the presence of endogenous SUN proteins, we propose that SUN protein oligomerization may be subject to previously unidentified mechanisms of regulation within the NE. Specifically, we reveal the nCC of SUN2 as a potential target for regulation. The differential *in vivo* oligomerization of SUN1 and SUN2 described in this work imply that SUN proteins may have evolved to form different assembly states in order to participate in diverse mechanotransduction events.

The development of FFS for use within the NE of living cells provides a powerful experimental method for probing the *in vivo* biochemical and biophysical behaviors of NE proteins within their native environment. The results obtained from FFS experiments performed in living cells allows for a critical assessment of models of NE protein function based on *in vitro* experiments. A unique strength of FFS is that it provides access to the average oligomeric state of protein complexes in living cells through brightness analysis. This work extends the

application of FFS to the NE and establishes z-scan FFS as a viable experimental approach for quantifying protein-protein interactions within this

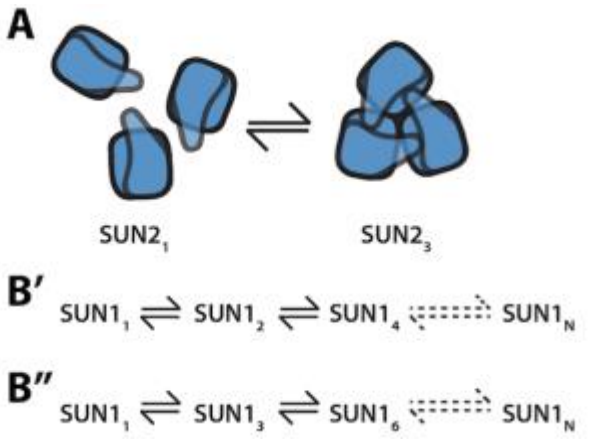

Figure 18: Working models of SUN1 and SUN2 oligomerization within the NE. (A) Working model of SUN2 oligomerization within the NE. (B' and B'') Working models of SUN1 oligomerization with the NE, which ultimately lead to the assembly of higher-order SUN1 oligomers ($SUN1_N$). Simple molecular equations are provided due to the lack of structural information available for SUN1.

previously un-explored sub-cellular compartment, which enables the investigation of their biochemical and biophysical behaviors of NE proteins within their native environment.

Mechanisms of SUN2 trimerization within the NE. Our data support the existence of SUN2 trimerization within the NE of living cells, which is in agreement with previously published *in vitro* studies (Sosa et al., 2012; Wang et al., 2012; Zhou et al., 2012). Our modeling suggests the following working model of SUN2 oligomerization where SUN2 monomers are in equilibrium with SUN2 trimers NE, with no evidence for a significantly populated dimeric state (Figure 18A). These *in vivo* data are inconsistent with the previously postulated existence of an extended network of SUN2 within the PNS, which forms through the SUN2 cCCs and/or SUN domain (Wang et al., 2012; Zhou et al., 2012). While $SUN2^{261-731}$ contains both cCCs and nCC, $SUN2^{520-731}$ only possesses the nCC. Despite this difference, both constructs displayed similar concentration-dependent oligomerization within the NE (Figures 11C-D) clearly demonstrating that the nCC is sufficient for SUN2 trimerization. The sufficiency of the nCC for SUN2 trimerization is corroborated by crystallographic data generated using a human SUN2 construct containing the nCC and SUN domain (Sosa et al., 2012).

Differential SUN protein oligomerization within the NE. The general ability of SUN proteins to form oligomers within the NE is further demonstrated by

brightness analysis of SS-EGFP-SUN1$^{457-913}$. SS-EGFP-SUN1$^{457-913}$ exhibited *b* values that increased over the entire tested range of concentrations without saturating, which indicates that SUN1 forms higher-order oligomers than SUN2 within the NE of living cells. This is also supported by the cytosolic *b* binding data obtained for EGFP-SUN1$^{457-913}$, which indicate the presence of oligomeric states in excess of a trimer. Currently, we cannot distinguish between two working models of SUN1 oligomerization that are not mutually exclusive (Figures 18B'-B"). In the first, SUN1 oligomerizes via a monomer/dimer/tetramer reaction (Figure 18B'). In the second, SUN1 oligomerizes via a monomer/trimer/hexamer reaction (Figure 18B"). Both reactions would ultimately lead to the assembly of higher-order SUN1 oligomers ($SUN1_N$) through progressive oligomerization (i.e. monomer to trimer to hexamer to n-mer).

The ability of SUN1 to form higher-order oligomers within the NE is consistent with a previously published report of the existence of immobile macromolecular assemblies of SUN1 within the NE (Lu et al., 2008). The same report demonstrated that SUN1 was able to form dimers and tetramers that were mediated by inter-chain disulfide bonds (Lu et al., 2008), suggesting that SUN1 oligomerization may be regulated by changes in the redox potential of the ER lumen/PNS (Frand et al., 2000; Hwang et al., 1992). It is also possible that the higher-order SUN1 oligomers that we detected in our experiments may result from lateral SUN1 trimer-trimer interactions similar to those that were previously

postulated for SUN2 (Wang et al., 2012; Zhou et al., 2012). Future experiments designed to identify amino acids within the $SUN1^{LD}$ that are critical for oligomerization will shed much needed light on the poorly understood mechanism of SUN1 oligomerization.

The differences we observe in our z-scan FFS experiments between the oligomerization of SUN1 and SUN2 provide supporting evidence for SUN protein functional specification. SUN1 and SUN2 are stated to perform redundant functions during the DNA damage response (Lei et al., 2012), radial neuronal migration in the developing mouse cerebral cortex and hippocampus (Zhang et al., 2009), and synaptic nuclear anchorage in mouse skeletal muscle (Lei et al., 2012). In strong support of the interchangeability of SUN1 and SUN2, expression of the *SUN1* gene under the control of a neuron-specific promoter was able to rescue the neonatal lethality in SUN1/2 double knockout mice indicating that SUN1 and SUN2 are critically and redundantly required for normal central nervous system development (Lei et al., 2012). These redundancies may be due to the ability of both SUN1 and SUN2 to interact promiscuously with the KASH peptide of several KASH proteins including nesprin-1, -2, and -3 (Stewart-Hutchinson et al., 2008). In addition, the $SUN1^{LD}$ and $SUN2^{LD}$ were shown to have a similar affinity of interaction for the KASH peptide of nesprin-2 (Östlund et al., 2009), suggestive of a similar mechanism of SUN-KASH interaction for these SUN proteins. In support of this idea, both SUN1 and SUN2 act redundantly to

recruit nesprin-1 and nesprin-2 to the NE of mouse muscle and retina cells, respectively (Lei et al., 2009; Yu et al., 2011). However, the functions performed by SUN1 and SUN2 described above may only be partially redundant and these redundancies appear to vary from tissue to tissue. For example, the functional redundancy reported for SUN1 and SUN2 during synaptic nuclear anchorage in mouse skeletal muscle was only observed in mice lacking both genes (Lei et al., 2009). SUN2 knockout mice did not exhibit defects, whereas SUN1 knockout mice were only partially defective during synaptic nuclear anchorage in this tissue (Lei et al., 2009). In addition, SUN1 was found to be more important for nesprin-2 recruitment to the NE in retina cells than SUN2 (Yu et al., 2011). Furthermore, the expression of SUN1 in the nervous system of SUN1/2 double knockout mice did not fully restore these mice to a wild type phenotype as demonstrated by the persistence of behavioral defects (Lei et al., 2009), which may be related to the requirement for SUN1 during the development of specific brain regions including the midbrain (Zhang et al., 2009).

SUN proteins differentially associate with various structures found within the NE. For example, fluorescence resonance energy transfer experiments show that SUN1 is more closely associated with A-type lamins than SUN2 (Östlund et al., 2009). SUN1 is also known to form ring-shaped clusters at the NE attachment sites of meiotic telomeres (Chikashige et al., 2006; Ding et al., 2007; Horn et al., 2013; Penkner et al., 2007; Schmitt et al., 2007). SUN1 also localizes to NPCs

and is important for their assembly and distribution along the NE in interphase cells (Liu et al., 2007; Talamas and Hetzer, 2011). Unlike SUN1, SUN2 is recruited to linear arrays of nesprin-2G known as TAN lines that form along perinuclear actin cabled during rearward nuclear movement in migrating fibroblasts and myoblasts (Chang et al., 2015a; Luxton et al., 2010). The ability of SUN1 to form higher-order oligomers than SUN2 within the NE may potentially explain the differential requirement of SUN1 during meiotic chromosome pairing via lateral microtubule-generated forces and/or during nuclear pore complex (NPC) biogenesis (Ding et al., 2007; Horn et al., 2013; Li et al., 2014; Lottersberger et al., 2015; Lu et al., 2008; Talamas and Hetzer, 2011). In the future, it will be important to examine the relationship between SUN protein oligomerization and these examples of functional specificity.

Regulation of SUN protein oligomerization within the NE. With the exception of the isolated SUN domain constructs, expression of the majority of our EGFP-tagged SUN1 and SUN2 constructs within the cytoplasm significantly altered their oligomerization. Both EGFP-tagged SUN1$^{457\text{-}913}$ and SUN2$^{260\text{-}731}$ constructs displayed differences in the concentration dependence of their *b* binding curves between the cytoplasm and the NE. These differences may be explained by either binding competition with endogenous SUN proteins or environment-specific modulation of cCCs and/or nCC. While our modeling shows that competition with endogenous SUN proteins may potentially account for the

observed concentration-dependent changes in binding, it cannot rule out the contribution of environmental effects on SUN protein oligomerization. Consequently, it will be important to measure EGFP-tagged SUN1 and SUN2 construct oligomerization in cells lacking either SUN1 or SUN2. Because our modeling provides predictions on the expected change in the binding curve, we will be able to distinguish between the effect of endogenous SUN proteins and environmental effects.

Potential environmental factors could be the presence of NE or lumenal proteins, which may structurally regulate and/or influence SUN protein oligomerization. The lack of NPCs within the cytoplasm may potentially explain the difference in SUN1 oligomerization within these two sub-cellular compartments. Within the NE, SUN1 trimers may assemble into higher-order oligomers via potential lateral interactions between trimers. Alternatively, SUN1 may not associate with NPCs as trimers and instead SUN1 monomers or other oligomeric assembly states may be important for NPC-association. Recently, the SUN1 was reported to directly interact with Nup153, an essential component of the NPC basket, within the nucleoplasm (Li and Noegel, 2015). Since SS-EGFP-SUN1$^{457\text{-}913}$ resides within the PNS of the NE, the Nup153-SUN1 interaction is unlikely to be responsible for the higher-order oligomerization we observed in our experiments. Therefore, to be able to test the role of the NPC on SUN1 oligomerization, further efforts must be directed towards identifying additional mechanisms responsible for SUN1

localization to the NPC. SUN protein oligomerization may also be regulated within the NE by protein disulfide isomerases (PDIs), a family of ER-resident thiol-disulfide oxidoreductases that catalyze the exchange of a disulfide bond with or within substrates (Appenzeller-Herzog and Ellgaard, 2008). Since their substrates are mostly unidentified, it will be exciting to test whether or not PDIs may regulate SUN protein and consequently LINC complex assembly.

In addition to these protein-based environmental factors, the contiguous ER lumen and PNS have a high calcium concentration and an oxidizing environment that favors the formation of disulfide bonds (Ellgaard and Helenius, 2003; Papp et al., 2003; Sevier and Kaiser, 2002). The SUN2 crystal structure identified the presence of a conserved loop that coordinates a bound cation, known as the cation loop (Sosa et al., 2012). Although the cation was potassium in the published crystal structure, the potential flexibility of the cation loop was hypothesized to coordinate a calcium ion in the PNS (Sosa et al., 2012). Since shortening the cation loop by one amino acid disrupted KASH-binding, which depends upon trimerization (Sosa et al., 2012), we anticipate that the cation loop may be important for SUN2 oligomerization.

Perhaps the strongest evidence for the existence of the environmental regulation of SUN protein oligomerization is provided by the inability of EGFP-SUN2$^{520\text{-}731}$ to trimerize within the cytoplasm. Since endogenous unlabeled SUN2 is absent

from the cytoplasm and therefore unable to influence the oligomerization of this construct, we postulate that either the oligomerization of SUN2$^{520-731}$ requires the presence of chemical factors and/or SUN2-interacting proteins found within the NE. Close inspection of the binding data for SUN2$^{520-731}$ within the NE demonstrates slightly weaker binding than observed for SUN2$^{261-731}$ (Figure 11D), revealing the energetic contributions of the cCCs to the oligomerization process. That SUN2$^{520-731}$ no longer trimerizes within the cytoplasm suggests that the nCC-mediated SUN2 oligomerization may be a target for regulatory factors. Interestingly, Sosa *et al*. report that a similar SUN2 construct that contains the nCC and SUN domain crystallized as a trimer was significantly impaired for KASH-binding as evaluated by pull-downs (Sosa et al., 2012). This implies that their construct may not have been able to oligomerize in the pull-down assay, since KASH-binding sites are formed at the interface between SUN2 protomers (Sosa et al., 2012; Wang et al., 2012). Taken together, these results indicate that the nCC-containing region between the cCCs and the SUN domain may be targeted by currently unidentified regulator factors to modulate SUN2 oligomerization independent of the cCCs. To address this hypothesis, the relative contributions of the cCCs and the nCC during SUN2 oligomerization need to be evaluated and the potential regulators of SUN2 function within the NE identified.

Conclusions. Our study establishes z-scan FFS and brightness analysis as a powerful tool for quantifying protein-protein interactions within the PNS of the NE. In agreement with previous *in vitro* structural studies (Sosa et al., 2012; Wang et al., 2012; Zhou et al., 2012), we show that SUN2 trimerizes within the NE. We also demonstrate that unlike SUN2, SUN1 forms higher-order oligomers within this sub-cellular compartment. Finally, we provide supporting evidence that SUN protein oligomerization within the NE may be subject to as-of-yet unidentified regulatory mechanisms. Our results provide the foundation for future studies designed to use z-scan FFS and brightness analysis to characterize the biochemical and biophysical behavior of soluble and membrane-bound NE proteins within their native cellular environment. In particular, future efforts will be focused on adapting image correlation spectroscopy methods (Digman et al., 2012) to the NE of living cells to overcome the current limitations imposed by the limited mobility of SUN proteins. Given the ever-growing list of human diseases associated with mutations in genes encoding NE proteins, z-scan FFS and brightness analysis will uniquely allow the consequences of these mutations to be experimentally determined in the NE of living cells.

MATERIALS AND METHODS

Reagents. Restriction enzymes (REs) were either purchased from New England Biolabs (NEB, Ipswich, MA) or Promega (Madison, WI). Phusion DNA

polymerase, T4 DNA ligase, and T4 PolyNucleotide Kinase (PNK) were also purchased from NEB. All other chemicals were from Sigma-Aldrich (St. Louis, MI) unless otherwise specified. GFP mouse monoclonal antibodies were from Sigma-Aldrich (Cambridge, MA). IRDye® 650 nm-conjugated goat anti-mouse secondary antibodies were from LI-COR (Lincoln, NE). Wizard SV Gel and PCR Clean-Up System was from Promega. GeneJet Plasmid Midiprep Kit was from ThermoFisher Scientific (Waltham, MA).

Cell culture. U2OS cells obtained from the ATCC (Manassas, VA) were cultured using standard sterile technique in DMEM medium with 10% fetal bovine serum from Hycolone Laboratories (Logan, UT).

DNA constructs. The SS-EGFP and SS-EGFP$_2$ constructs were generated as follows using a previously described human SS-EGFP-torsinA construct (Goodchild and Dauer, 2004). EGFP from SS-EGFP-torsinA was PCR amplified using the primers SS-EGFP-F and SS-EGFP-R (Table 1), which contain 5' *Nhe*I and *Eco*RI RE cut sites, respectively. The PCR product was purified and digested alongside SS-EGFP-torsinA with *Nhe*I and *Eco*RI. Following gel purification, the digested PCR product and plasmid were ligated together to create SS-EGFP. To generate SS-EGFP$_2$, EGFP was amplified from SS-EGFP-torsinA using the primers SS-EGFP$_2$-F and SS-EGFP$_2$-R (Table 1), which contains 5' *Bsr*GI and *Apa*I RE cut sites, respectively. In addition, SS-EGFP$_2$-F

encodes a 10 amino acid linker (GHGTGSTGSG) following the *Bsr*GI site, while SS-EGFP2-R encodes a mutated *Bsr*GI site that disrupts the 3' *Bsr*GI present in EGFP. The resulting PCR product was then purified and digested beside SS-EGFP with *Bsr*GI and *Apa*I. The digested PCR product and plasmid were purified and ligated to make SS-EGFP$_2$.

The EGFP-tagged FL mouse SUN1 and SUN2 constructs were previously described (Luxton et al., 2010) and used as templates for the generation of the SS-EGFP-tagged lumenal SUN1 and SUN2 constructs. To create SS-EGFP-SUN2$^{261\text{-}731}$, the sequence encoding amino acids 261-731 was PCR amplified from EGFP-SUN2^{FL} using the SS-EGFP-SUN2$^{261\text{-}731}$-F and SS-EGFP-SUN2$^{261\text{-}731}$-R primer pair (Table 1), which contain 5' *Bsr*GI and *Eco*RI RE cut sites, respectively. In addition, SS-EGFP-SUN2$^{261\text{-}731}$-F encodes a 10 amino acid linker (GHGTGSTGSG) following the *Bsr*GI site. The PCR product was purified and digested alongside SS-EGFP with *Bsr*GI and *Eco*RI. Following gel purification, the digested PCR product and plasmid were ligated together to create SS-EGFP-SUN2$^{261\text{-}731}$. SS-EGFP-SUN2$^{520\text{-}731}$ and SS-EGFP-SUN2$^{595\text{-}731}$ were both generated via Kinase, Ligase, DpnI (KLD) treatment where 2µL PCR product was treated with T4 ligase, T4 PNK, and DpnI in T4 ligase buffer in a 20µL reaction for 20 minutes at room temperature. The forward primers used to create SS-EGFP-SUN2$^{520\text{-}731}$ and SS-EGFP-SUN2$^{595\text{-}731}$ were SS-EGFP-SUN2$^{520\text{-}731}$-F and SS-EGFP-SUN2$^{595\text{-}731}$-F, respectively (Table 1). The same reverse primer, SS-

EGFP-SUN2$^{\Delta}$-R (Table 1), was used for both SS-EGFP-SUN2$^{520-731}$ and SS-EGFP-SUN2$^{595-731}$.

To create SS-EGFP-SUN1$^{457-913}$, the sequence encoding amino acids 457-913 was PCR amplified from EGFP-SUN1^{FL} using the primers SS-EGFP-SUN1$^{457-913}$-F and SS-EGFP-SUN2$^{457-913}$-R (Table 1), which contain 5' *Bsr*GI and *Eco*RI RE cut sites, respectively. SS-EGFP-SUN1$^{457-913}$-F also encodes a 10 amino acid linker (GHGTGSTGSG) following the *Bsr*GI site. The PCR product was purified and digested beside SS-EGFP with *Bsr*GI and *Eco*RI. Following gel purification, the digested PCR product and plasmid were ligated together to create SS-EGFP-SUN1$^{457-913}$. SS-EGFP-SUN1$^{777-913}$ was generated via KLD treatment using the primers SS-EGFP-SUN1$^{777-913}$-F and SS-EGFP-SUN1$^{777-913}$-R (Table 1).

The cytoplasmic EGFP-tagged SUN1 and SUN2 constructs were generated via KLD reactions as follows. EGFP-SUN2$^{260-731}$ and EGFP-SUN1$^{457-913}$ were made first using the primers SS$^{\Delta}$-F and SS$^{\Delta}$-R (Table 1). KLD treatments were used to make EGFP-SUN2$^{520-731}$ and EGFP-SUN2$^{595-731}$. The forward primers used to create EGFP-SUN2$^{520-731}$ and EGFP-SUN2$^{595-731}$ from EGFP-SUN2$^{260-731}$ were SS-EGFP-SUN2$^{520-731}$-F and SS-EGFP-SUN2$^{595-731}$-F, respectively (Table 1). The same reverse primer, SS-EGFP-SUN2^{deletion}-R (Table 1), was used for both EGFP-SUN2$^{520-731}$ and EGFP-SUN2$^{595-731}$. EGFP-SUN1$^{777-913}$ was generated via KLD treatment from EGFP-SUN1$^{457-913}$ using the primers SS-EGFP-SUN1$^{777-913}$-F and SS-EGFP-SUN1$^{777-913}$-R (Table 1).

Transfections. Transient transfections were carried out 24 hours prior to measurement using GenJet from SignaGen Laboratories (Rockville, MD) or Lipofectamine LTX from Invitrogen (Carlsbad, CA) according to the manufacturers' instructions. Immediately before measurement, the growth medium was replaced with Dulbecco's phosphate-buffered saline (PBS) with calcium and magnesium from Biowhittaker (Walkerville, MD).

Live cell epifluorescence microscopy. Twelve hours prior to their transfection, U2OS cells were grown in 24-well plates with #1.5 glass coverslip (0.16-0.19 mm) bottoms or 35 mm dishes with #1.5 glass coverslip bottoms from In Vitro Scientific (Sunnyvale, CA). Cells were then washed twice with live imaging media composed of HBSS (GIBCO®, Invitrogen) containing essential and nonessential MEM amino acids (Invitrogen), 2.5 g/L glucose, 2 mM glutamine, 1 mM sodium pyruvate, 20 mM HEPES (pH 7.4)), and transferred to a 37° C Okolab full-enclosure incubator (Ottaviano, Italy) with temperature control attached to a Intelligent Imaging Innovations (3I, Denver, CO) Marianas 200 Microscopy Workstation built on a Zeiss AxioObserver Z.1 stand (Jena, Germany) and driven by SlideBook 6.0 from 3I. All live cell epifluorescence images were acquired with a Zeiss Plan-Apochromat 63x/1.4NA oil objective, a Sutter DG4 light source (Novato, CA), and a Photometrics CoolSnap HQ2 CCD (Tucson, AZ). A

BrightLine Sedat filter set, optimized for DAPI, FITC, TRITC, and CY5 from Semrock (Rochester, NY) was used.

Z-scan FFS and analysis. The instrumental setup has been previously described (Hur and Mueller, 2015). All analysis steps were performed with programs written in Research Systems IDL 8.3 (Boulder, CO). The experimental two-photon spot or point spread function (PSF) of the two-photon microscope was described using a modified squared Gaussian-Lorentzian (mGL) model (Macdonald et al., 2010; Macdonald et al., 2013). A z-scan calibration procedure was performed as previously described to determine the radial and axial beam waists (w_0 and z_0) and the axial decay parameter (*y*) (Macdonald et al., 2010), which resulted in z_0 = 1.02 ± 0.1 µm, *y* = 2.30 ± 0.3 and w_0=0.45 ± 0.05 µm. Given that the NE is significantly thinner (~30-50 nm) (Franke et al., 1981) than the two-photon spot produced by our microscope (~1 µm), we model the NE as an infinitely thin “delta (δ)-layer” (Macdonald et al., 2010). Two δ-layers were used to represent the two NE layers (ventral and distal) along the scan path. Their locations are indicated by the coordinates z_V and z_D, respectively. The nucleoplasmic layer is modeled as a layer of finite thickness or “slab (*s*)-layer” (Macdonald et al., 2010). The s-layer represents a uniform fluorescent layer stretching along the optical axis from z_V to z_D. The intensity profile of a δ-layer located at height z_V is $F_\delta(z) = F_0 g_\delta(z, z_V)$. Similarly, the intensity profile of the s-

layer stretching from z_V to z_D is given by $F_s(z) = F_0 g_s(z, z_V, z_D)$. The functions g_δ and g_s describe the shape of the intensity profile, whereas F_0 accounts for the intensity amplitude of the layer (Smith et al., 2015a). The z-scan intensity profile of cells was described with a "δsδ" model to account for the fluorescence response of the ventral NE, the nucleus, and the dorsal NE, $F_{\delta s\delta}(z) = F_\delta^{(V)}(z) + F_s^{(N)}(z) + F_\delta^{(D)}(z)$. The experimental intensity profile $F(z)$ was fit to the "δsδ" model $F_{\delta s\delta}(z)$ to identify the fluorescence intensity contributions from each individual layer. Dividing the peak intensity $F_\delta^{(V)}(z_V)$ from the NE$_V$ at location z_V by the total intensity at the same location defines the intensity fraction $f_{NE}^{(V)}$ from the NE$_V$. Repeating the same procedure at the dorsal location ($z = z_D$) determines the intensity fraction $f_{NE}^{(D)}$ from the NE$_D$.

The photon counts collected from a z-scan were re-binned to a sampling time of $T_z = 4$ ms, which corresponds to a step size $\Delta z = v_z T_z = 19.3$ nm between adjacent binned photon counts k_z. The experimental fluorescence intensity profile, $F(z) = k_z / T_z$, is calculated and fit to a model using a Levenberg–Marquardt algorithm (Watson and Shapiro, 1982) with the PSF parameters z_0 and *y* fixed to the calibrated values. The standard error σ of k_z was determined from the standard deviation of the un-binned counts by $\sigma = \sigma_{unbinned}\sqrt{N_B}$ with the number N_B of samples being equal to 80.

Brightness analysis. The photon counts collected with the PSF centered on the NE layer were analyzed to extract Mandel's Q factor using previously described algorithms (Hur and Mueller, 2015; Sanchez-Andres et al., 2005). The brightness λ was related to Q by $Q = \gamma_2 \lambda T$ (Sanchez-Andres et al., 2005) because the speed of our data sampling time *T* was sufficiently fast to avoid under-sampling. The gamma factor γ_2 depends on the PSF and the sample geometry (Smith et al., 2014). For an mGL PSF centered on a δ layer γ_2 is 0.5 (Macdonald et al., 2010). Performing an FFS experiment in the nucleus of cells expressing EGFP establishes the raw brightness λ_{EGFP} as previously described (Chen et al., 2003). The *b* is defined by $b = \lambda / \lambda_{EGFP}$, a dimensionless number that describes the average oligomeric state of the labeled protein (Macdonald et al., 2013; Macdonald et al., 2014). For example, a homo-dimeric complex leads to *b* = 2. Brightness analysis for FFS experiments in the cytoplasm are performed as described above, but with an adjusted γ_2 to reflect the different geometry. The value of γ_2 has been determined using z-scan FFS as described earlier (Macdonald et al., 2010).

The number concentration *N* represents the average number of labeled protein monomers in the observation volume and is calculated by dividing the fluorescence intensity *F* by λ_{EGFP} (Chen et al., 2003). This procedure is valid for

FFS experiments in the cytoplasm as well as at the NE. The observation volume V_O is given by the overlap between the two-photon PSF and the fluorescent sample. Converting the number concentration into a molar concentration is achieved by $c = N/(V_O N_A)$, where N_A is Avogadro's number. The volume $V_O^{(C)}$ of a cytoplasmic FFS experiment is measured using a previously published procedure (Macdonald et al., 2010). In contrast, the volume $V_O^{(NE)}$ and therefore the labeled protein concentration of FFS experiments at the NE cannot be determined experimentally.

Brightness modeling. A monomer/dimer/trimer equilibrium reaction was used to model *b* as a function of *N*. The number of molecules of monomers, dimers, and trimers (N_1, N_2, N_3) was determined by the reactions $A + A \rightleftharpoons A_2$ and $A + A_2 \rightleftharpoons A_3$ with the dissociation coefficients K_{MD} and K_{DT}, respectively. The *b* of an *n*-mer is given by $b = n$. The brightness of this mixture of species is $b = \sum_{i=1}^{3} b_i^2 N_i \Big/ \sum_{i=1}^{3} b_i N_i$. The total number of monomeric proteins in the observation volume is $A_0 = A + 2A_2 + 3A_3$. The presence of an unlabeled endogenous protein that can interact with the exogenous labeled protein population was treated by considering a fluorescent and a non-fluorescent species of A. The sum of the total number of non-fluorescent molecules (A_{0N}) and fluorescent molecules (A_{0F}) equals the total number of molecules $A_0 = A_{0F} + A_{0N}$. The brightness of non-

fluorescent molecules is set to zero, and the probability that a given molecule of A is labeled is $p = A_{0F}/A_0$. The *b* was evaluated for the monomer / dimer / trimer equilibrium reaction with a fraction p of the molecules being fluorescent. The same analysis was performed for other binding equilibrium models, such as the monomer/trimer reaction $3A \rightleftharpoons A_3$ with a dissociation coefficient defined by $K_{MT}^2 = [A]^3/[A_3]$. Fitting of the experimental data to *b* binding models was accomplished using bootstrapping (Efron, 1992). Confidence intervals of the estimated parameters were also determined from the bootstrap algorithm.

The observation volume $V_O^{(NE)}$ of NE measurements is small compared to the observation volume $V_O^{(C)}$ of cytoplasmic FFS experiments, which is reflected in the measured *N*. To facilitate the comparison of *b* changes with concentration of a protein in both compartments, it is useful to translate between the measured *N* in both environments. This is achieved by the molar concentration defined by *c* = $N^{(C)}/(V_O^{(C)}N_A) = N^{(NE)}/(V_O^{(NE)}N_A)$, which demonstrates that the values of *N* in the cytoplasm and the NE are proportional to one another, $N^{(C)} = N^{(NE)}V_O^{(C)}/V_O^{(NE)}$. While the observation volume at the NE cannot be measured, it can be modeled as the product of the cross-sectional area of the PSF and the thickness *h* of the NE layer, $V_O^{(NE)} = \frac{\pi w_0^2}{4} h$. Given previously published measurements of NE thickness using electron microscopy (Franke et al., 1981), we assume that the

NE has an average thickness h = 40 nm and thus a volume of 6.9 10^{-3} fl. The observation volume in the cytoplasm with a fully embedded PSF was determined to be 0.23 fl.

Chapter 3

TorsinA controls TAN line assembly and the retrograde flow of dorsal perinuclear actin cables during rearward nuclear movement.

This chapter has been accepted for publication in the Journal of Cell Biology as DOI 10.1083/jcb.201507113 Cosmo A. Saunders, Nathan J. Harris, Patrick T. Willey, Brian M. Woolums, Yuexia Wang, Alex J. McQuown, Amy Schoenhofen, Howard J. Worman, William T. Dauer, Gregg G. Gundersen, and G.W. Gant Luxton “TorsinA controls TAN line assembly and the retrograde flow of dorsal perinuclear actin cables during rearward nuclear movement.”

Synopsis

The nucleus is positioned towards the rear of most migratory cells. In fibroblasts and myoblasts polarizing for migration, retrograde actin flow moves the nucleus rearward resulting in the orientation of the centrosome in the direction of migration. Here, we report that the nuclear envelope localized AAA+ ATPase torsinA and its activator, the inner nuclear membrane protein LAP1, are required for rearward nuclear movement during centrosome orientation in migrating fibroblasts. We show that both torsinA and LAP1 contributed to the assembly of transmembrane actin-associated nuclear (TAN) lines, which couple the nucleus to dorsal perinuclear actin cables undergoing retrograde flow. In addition, we reveal that torsinA localized to TAN lines and was necessary for the proper mobility of EGFP-mini-nesprin-2G, a functional TAN line reporter construct, within the nuclear envelope. Furthermore, torsinA and LAP1 were indispensible for the retrograde flow of dorsal perinuclear actin cables, supporting the recently proposed function for the nucleus in spatially organizing actin flow and cytoplasmic polarity. Taken together, these results identify torsinA as a key regulator of actin-dependent rearward nuclear movement during centrosome orientation.

INTRODUCTION

A hallmark of cell polarity in many migratory cell types is the orientation of the centrosome to a position between the nucleus and leading edge (Gundersen and Worman, 2013; Luxton and Gundersen, 2011). The inability of cells to establish and maintain anterior centrosome orientation results in inefficient migration. Direct imaging of the centrosome in fibroblasts demonstrates that productive protrusion and migration occurs only after anterior centrosome orientation is achieved (Gomes et al., 2005). In wounded monolayers of fibroblasts and myoblasts polarizing for migration, anterior centrosome orientation is established by coordinated positioning of the nucleus and centrosome. During this process, retrograde actin flow moves the nucleus towards the cell rear, whereas the centrosome is maintained at the cell center (Chang et al., 2015a; Gomes et al., 2005). In fibroblasts, the maintenance of the centrosome at the cell center depends upon the polarity proteins Par3, Par6, and PKCζ, the minus-end directed microtubule motor protein dynein, and dynamic microtubules (Gomes et al., 2005; Palazzo et al., 2001; Schmoranzer et al., 2009).

In fibroblasts and myoblasts, the forces generated by the retrograde flow of dorsal perinuclear actin cables are harnessed by the nucleus through TAN lines (Chang et al., 2015a; Luxton et al., 2010). TAN lines are composed of the outer nuclear membrane (ONM) and inner nuclear membrane (INM) proteins nesprin-

2G (N2G) and SUN2, respectively. N2G is an ~800 kD spectrin repeat-containing protein, the majority of which extends into the cytosol (Luxton and Starr, 2014). N2G interacts with dorsal perinuclear actin cables through its N-terminal actin-binding calponin homology domains resulting in the organization of N2G into TAN lines (Luxton et al., 2010; Zhen et al., 2002). The C-terminus of N2G contains the conserved KASH (Klarsicht, ANC-1, Syne homology) domain, which consists of a transmembrane domain (TMD) followed by a ~20-30 amino acid KASH peptide that directly interacts with the conserved *Sad1*/*UNC-84* (SUN) domain found at the C-terminus of SUN2 (Sosa et al., 2013; Östlund et al., 2009). The N-terminus of SUN2 projects into the nucleoplasm and interacts with the nuclear lamina as well as chromatin (Crisp et al., 2006; Sosa et al., 2013; Tapley and Starr, 2013). The anchorage of TAN lines by A-type lamins is essential for rearward nuclear movement (Chang et al., 2015a; Folker et al., 2011). The fundamental significance of rearward nuclear movement during cell migration is illustrated by the fact that both N2G and SUN2 are required for efficient fibroblast migration (Luxton et al., 2010). Furthermore, N2G-depletion inhibits myoblast migration and decreases the efficiency of their fusion into myotubes (Chang et al., 2015a). Despite their importance, the mechanisms of TAN line assembly remain poorly defined.

The KASH-SUN interaction forms an evolutionarily conserved molecular bridge across the perinuclear space termed the linker of nucleoskeleton and

cytoskeleton (LINC) complex (Chang et al., 2015b; Tapley and Starr, 2013). The crystal structure of SUN2 reveals a mushroom-like trimer with a cap composed of SUN domains and a stalk of three coiled-coils (Sosa et al., 2012; Sosa et al., 2013; Zhou et al., 2012). Each SUN2 trimer binds three KASH peptides in grooves that are formed between adjacent SUN domains. LINC complexes are typically depicted as being evenly distributed throughout the nuclear envelope (Starr and Fridolfsson, 2010). However, the identification of TAN lines argues that LINC complexes are dynamic within nuclear membranes. This idea is further supported by the observed reorganization of LINC complexes into focal accumulations during meiosis in *C. elegans* and during nuclear centering in the fission yeast, *S. pombe* (King et al., 2008; Sato et al., 2009). Therefore, a molecular mechanism for the regulation of LINC complex dynamics within the nuclear envelope must exist, although currently it is unknown.

Several lines of evidence implicate the conserved ATP-binding protein torsinA as a key regulator of LINC complex dynamics (Atai et al., 2012; Gerace, 2004; Saunders and Luxton, 2016). TorsinA was originally identified as the protein product encoded by the *TOR1A* gene, which causes the childhood movement disorder DYT1 dystonia when mutated (Ozelius et al., 1997). The mutation is an in-frame deletion that removes a single glutamic acid (ΔE302/303, or ΔE) that impairs torsinA function, in part by impairing the interaction of torsinA with its major interacting proteins: lamina-associated polypeptide 1 (LAP1) and lumenal

domain-like LAP1 (LULL1) (Goodchild and Dauer, 2005; Naismith et al., 2009; Zhao et al., 2013). While LAP1 is an INM protein (Senior and Gerace, 1988), LULL1 is distributed throughout the ER and consequently the ONM (Goodchild et al., 2005; Goodchild et al., 2015; Watson, 1955).

TorsinA is a member of the AAA+ ATPase superfamily, members of which typically function as ring-shaped hexameric molecular chaperones that utilize energy derived from ATP-hydrolysis to remodel protein complexes (Hanson and Whiteheart, 2005; Ozelius et al., 1997; Vale, 2000). Reports of torsinA exhibiting chaperone-like behaviors both *in vitro* and *in vivo* are consistent with the hypothesis that like AAA+ proteins, torsinA may act as a molecular chaperone (Burdette et al., 2010; Nery et al., 2011).

Torsin proteins themselves have negligible ATPase activity *in vitro* (Zhao et al., 2013). However, their activity is stimulated by a direct interaction with the ~60% identical lumenal domain (LD) of LAP1 ($LAP1^{LD}$) or LULL1 ($LULL1^{LD}$) (Brown et al., 2014; Goodchild and Dauer, 2005; Sosa et al., 2014; Zhao et al., 2013). The $LAP1^{LD}$ possesses an atypical AAA+ fold in which R442 is positioned similar the arginine finger of canonical AAA+ proteins (Brown et al., 2014; Sosa et al., 2014). Arginine fingers are structural features of AAA+ proteins thought to coordinate nucleotide hydrolysis (Hanson and Whiteheart, 2005). Since torsinA lacks identifiable arginine fingers, the torsinA-LAP1 interaction was postulated to result

in the formation of an alternating (LAP1-torsinA)$_3$ hetero-hexamer through which R442 of LAP1 could coordinate ATP-hydrolysis with an adjacent torsinA (Brown et al., 2014; Sosa et al., 2014). This proposed mechanism was supported by the reduced ability of LAP1^{LD} constructs lacking the proposed arginine finger to stimulate the ATPase activity of torsinA *in vitro* (Brown et al., 2014; Sosa et al., 2014).

Moreover, torsinA and the four additional mammalian torsin proteins (torsinB, torsin2A, torsin3A, and torsin4A) are the only AAA+ proteins known to reside within the ER lumen and contiguous perinuclear space (Goodchild and Dauer, 2004; Jungwirth et al., 2010; Kim et al., 2010; Naismith et al., 2004). While the functional relevance is unclear, torsinA is known to interact with torsinB (Hewett et al., 2004). Amongst the torsins, torsin4A is unique due to the presence of a predicted TMD (Rose et al., 2015). Despite these important advances in our understanding of the biochemical mechanism of torsin activity, the protein substrates remodeled by the torsins within the shared ER/perinuclear space remain unknown.

Experimental data suggest that torsinA has affinity for the KASH domains from nesprin-1, -2, and -3 (Nery et al., 2008), hinting that it might remodel LINC complexes within the nuclear envelope. Studies of the effects of torsinA inhibition on the architecture of the nuclear envelope provide indirect evidence of torsinA-

mediated LINC complex regulation (Goodchild et al., 2005; Naismith et al., 2004), as both torsinA and LINC complexes have been implicated in maintenance of the typical 30-50 nm distance between the INM and ONM (Cain and Starr, 2015; Crisp et al., 2006; Naismith et al., 2004). Furthermore, cells lacking torsinA redistribute nesprin-3α from the nuclear envelope to the ER; whereas cells with elevated levels of torsinA exhibit disrupted nuclear envelope localization of N2G, nesprin-3, and SUN2 (Nery et al., 2008; Vander Heyden et al., 2009). Finally, the *Caenorhabditis elegans* torsinA homologue OOC-5 is required for the proper localization of the nesprin homologue ZYG-12 in the nuclear envelope of germ cell nuclei (VanGompel et al., 2015). Together, these data suggest that torsinA regulates the LINC complex from within the nuclear envelope.

While torsinA has been implicated in centrosome orientation in migrating fibroblasts (Nery et al., 2011; Nery et al., 2014), the mechanism responsible for its role in this process is unclear as neither centrosome nor nuclear positioning were analyzed in these studies. Furthermore, the participation of the other torsin proteins, as well as LAP1 and LULL1, in centrosome orientation is unexplored. Therefore, we sought to elucidate the mechanism of torsinA-mediated centrosome orientation in migrating fibroblasts, hypothesizing that torsinA was either required for rearward nuclear movement or centrosome centration during centrosome orientation.

RESULTS

TorsinA is required for rearward nuclear movement during centrosome orientation. To begin to determine the mechanism of torsinA-dependent centrosome orientation, we first asked if acute siRNA-mediated depletion of torsinA inhibited lysophosphatidic acid (LPA)-stimulated centrosome orientation in serum-starved wound edge NIH3T3 fibroblasts (Luxton et al., 2010; Palazzo et al., 2001). We tested the ability of four independent siRNAs to efficiently knockdown torsinA mRNA and protein levels relative to control cells treated with previously characterized GAPDH and non-coding (NC) siRNAs (Kutscheidt et al., 2014; Luxton et al., 2010). All four torsinA-targeting siRNAs significantly depleted torsinA protein levels (Fig. 20A). Each of the torsinA-targeting siRNAs significantly inhibited centrosome orientation and rearward nuclear positioning in NIH3T3 fibroblasts relative to controls without rearward displacement of the centrosome (Figs. 19B-D and 20B-C). Importantly, the expression of a previously described construct encoding wild type (WT) torsinA with EGFP inserted after its signal sequence (SS-EGFP-TA^{WT}) (Goodchild and Dauer, 2004) rescued the centrosome orientation and rearward nuclear positioning defects observed in cells treated with siRNA TA.1 indicating that these defects were specifically due to torsinA-depletion (Figs. 19A-D). For the remainder of this work, we will use siRNA TA.1 to deplete torsinA. Similar results were obtained following LPA-stimulation of serum-starved mouse embryonic fibroblasts (MEFs) from *Tor1A*$^{-/-}$

mice (Goodchild et al., 2005) (Figs. 20D and 19B-D). Again, both centrosome

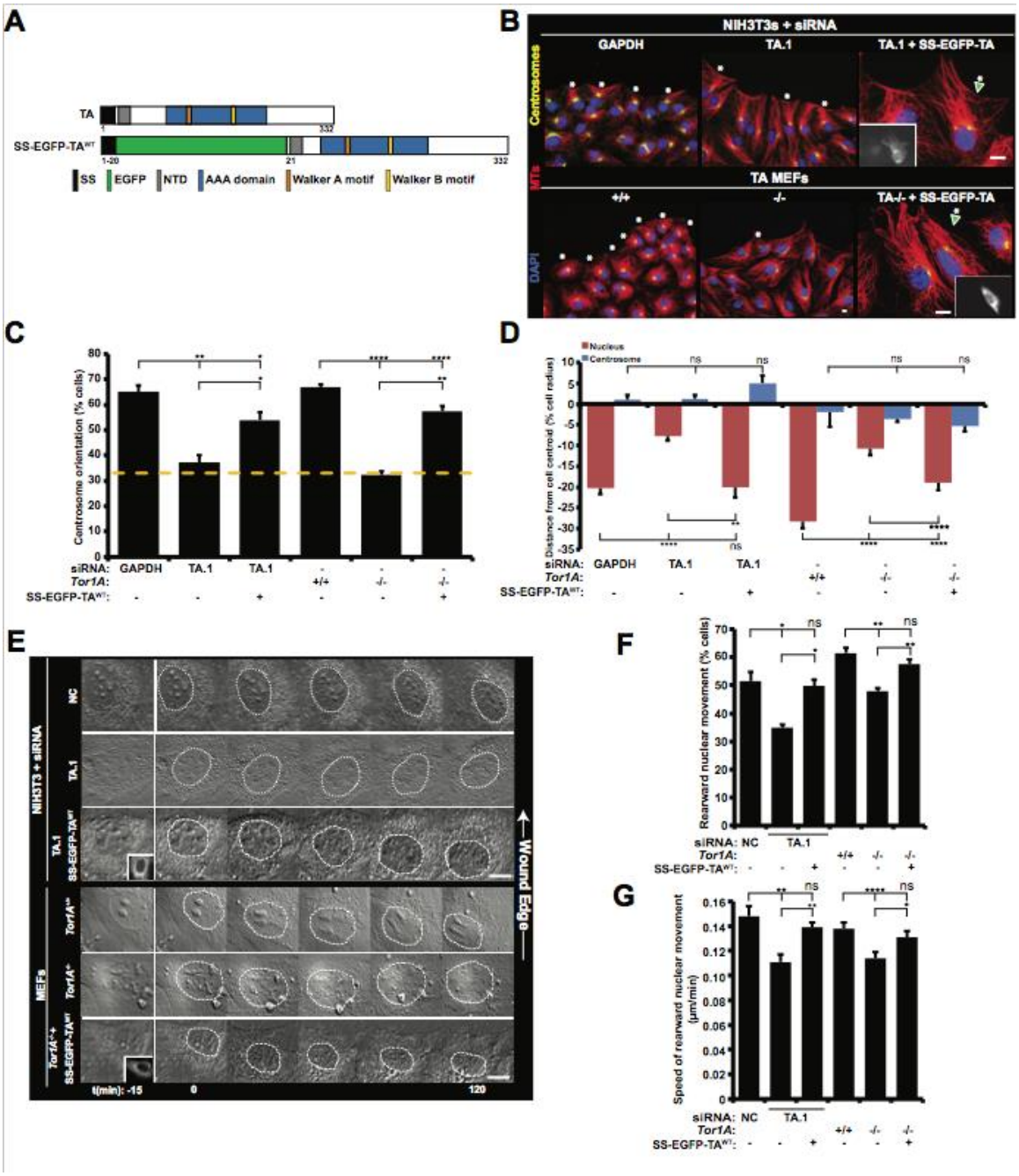

Figure 19: TorsinA-depletion inhibits rearward nuclear movement during centrosome orientation.

Figure 19: TorsinA-depletion inhibits rearward nuclear movement during centrosome orientation. (A) Diagrams of the human torsinA protein and SS-EGFP-TA^{WT}. Protein domains were identified using the SMART platform (Schultz et al., 1998). NTD: N-terminal domain (Vander Heyden et al., 2011)**. (B)** Representative epifluorescence images of centrosome orientation in NIH3T3 fibroblasts treated with GAPDH or TA.1 siRNA as well as *Tor1A*$^{+/+}$ and *Tor1A*$^{-/-}$ MEFs. A torsinA-depleted NIH3T3 fibroblast and *Tor1A*$^{-/-}$ MEF expressing SS-EGFP-TA^{WT} are also shown (arrowheads and inserts). Asterisk: oriented centrosomes. **(C)** Centrosome orientation in the cells described in B. The dashed yellow line denotes random orientation, which is ~33% (Palazzo et al., 2001). **(D)** Average centrosome and nucleus positions from the cells described in B. The cell center is defined as "0". Positive values are toward the leading edge; negative values, away. N ≥ 251. **(E)** Representative montages of DIC images of nuclear movement during centrosome orientation in wound-edge NIH3T3 fibroblasts treated with NC or TA.1 siRNA as well as *Tor1A*$^{+/+}$ and *Tor1A*$^{-/-}$ MEFs. A DIC montage of wound-edge cells expressing SS-EGFP-TA^{WT} (insert) is also provided. Nuclei are outlined by dashed white lines. Time is relative to the addition of LPA (0 min). **(F)** Percentage of the cells described in E with rearward moving nuclei. **(G)** Average velocity of nuclear movement from cells described in E. N≥ 14. Scale bars, B and E**:** 10 µm. ns: non-significant, C,D, F, and G.

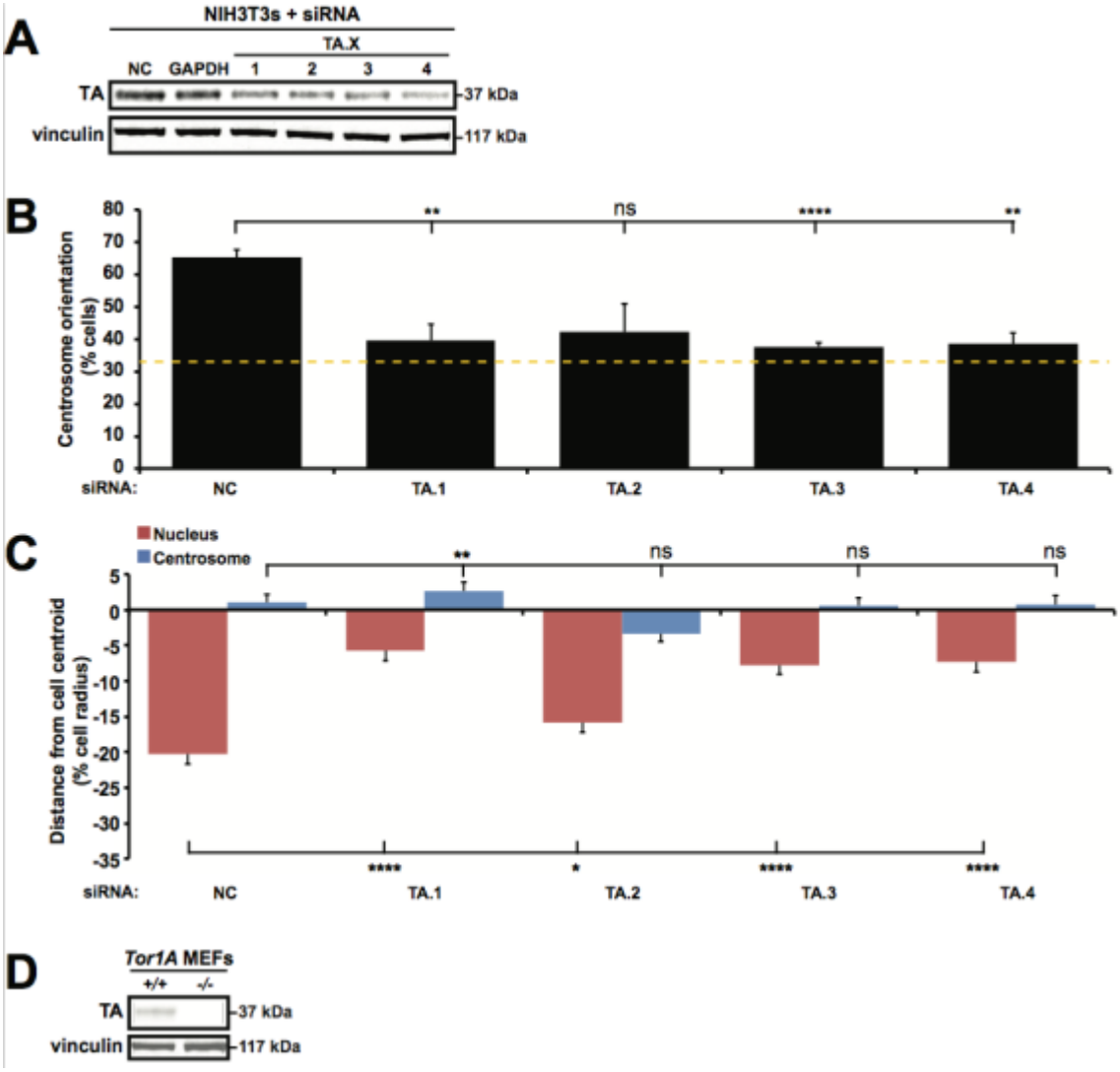

Figure 20: Validation of torsin protein depletion from NIH3T3 fibroblasts by various siRNAs

Figure 20: Validation of torsin protein depletion from NIH3T3 fibroblasts by various siRNAs. (A) Representative western blot of lysates from cells treated with siRNA probed with the indicated antibodies. **(B)** Centrosome orientation in wound-edge cells treated with the indicated siRNAs. The dashed yellow line denotes random centrosome orientation. **(C)** Average centrosome and nucleus positions measured from the cells described in B. N ≥ 183. **(D)** Representative western blot of lysates from *Tor1A*$^{+/+}$ and *Tor1A*$^{-/-}$ MEFs probed with the indicated antibodies. ns: non-significant, B and C.

orientation and rearward nuclear positioning in *Tor1A*$^{-/-}$ MEFs were rescued by SS-EGFP-TA^{WT} expression (Figs. 19B-D).

To determine whether the nuclear-positioning defect was due to a lack of rearward nuclear movement, we performed live-cell differential interference contrast (DIC) imaging in LPA-stimulated wound edge torsinA-depleted and control NIH3T3 fibroblasts. We found that the percentage of cells with rearward-moving nuclei and the speed of rearward nuclear movement were significantly reduced in cells depleted of torsinA relative to controls (Figs. 19E-G). Importantly, the expression of SS-EGFP-TA^{WT} in the torsinA-depleted cells restored both of these defects to control levels. Also consistent with torsinA-depleted NIH3T3 fibroblasts, live-cell DIC imaging of *Tor1A*$^{-/-}$ MEFs confirmed that torsinA was required for proper rearward nuclear movement as both the percentage of cells with rearward-moving nuclei and the speed of nuclear movement were impaired in *Tor1A*$^{-/-}$ relative to *Tor1A*$^{+/+}$ MEFs (Figs. 19E-G). Moreover, both of these defects could be rescued by SS-EGFP-TA^{WT} expression. Collectively, these results demonstrate that torsinA functions during centrosome orientation to promote rearward nuclear movement.

The redox-regulated ATPase activity of torsinA is required for rearward nuclear movement during centrosome orientation. To address the molecular mechanism responsible for torsinA-dependent rearward nuclear movement and

centrosome orientation, we expressed a torsinA construct encoding a mutation in the conserved Walker B motif (SS-EGFP-TA^{E171Q} (Fig. 21A) (Goodchild and Dauer, 2005)) in wound-edge NIH3T3 fibroblasts, which were then stimulated with LPA. TorsinA^{E171Q} does not hydrolyze ATP in the presence of the LD of LAP1 or LULL1 (Zhao et al., 2013) and similar ATP-hydrolysis-impaired Walker B mutations are often used as dominant negative constructs to disrupt AAA+ protein function (Hanson and Whiteheart, 2005). Unlike cells expressing SS-EGFP-TA^{WT}, those expressing SS-EGFP-TA^{E171Q} were significantly reduced in their ability to orient their centrosomes and in rearward nuclear positioning (Figs. 21B-D). Knowing that SS-EGFP-TA^{E171Q} acts in a dominant negative fashion to inhibit centrosome orientation, we next asked if a similar approach could be used to test if torsinB, torsin2, and torsin3 also functioned during this process. However, expression of SS-EGFP-tagged WT or Walker B mutant constructs of torsinB, torsin2, and torsin3 had no effect on centrosome orientation or rearward nuclear positioning in LPA-stimulated wound edge cells (Fig. 22). These results further support the requirement for torsinA-mediated rearward nuclear positioning during centrosome orientation in migrating fibroblasts and they suggest that the three other luminal torsins are not critically involved in this process.

To further test the requirement for the ATPase activity of torsinA during centrosome orientation, we asked if expressing SS-EGFP-TA^{E171Q} or SS-EGFP-TA^{K108A}, a construct encoding a mutation within the AAA+ Walker A domain

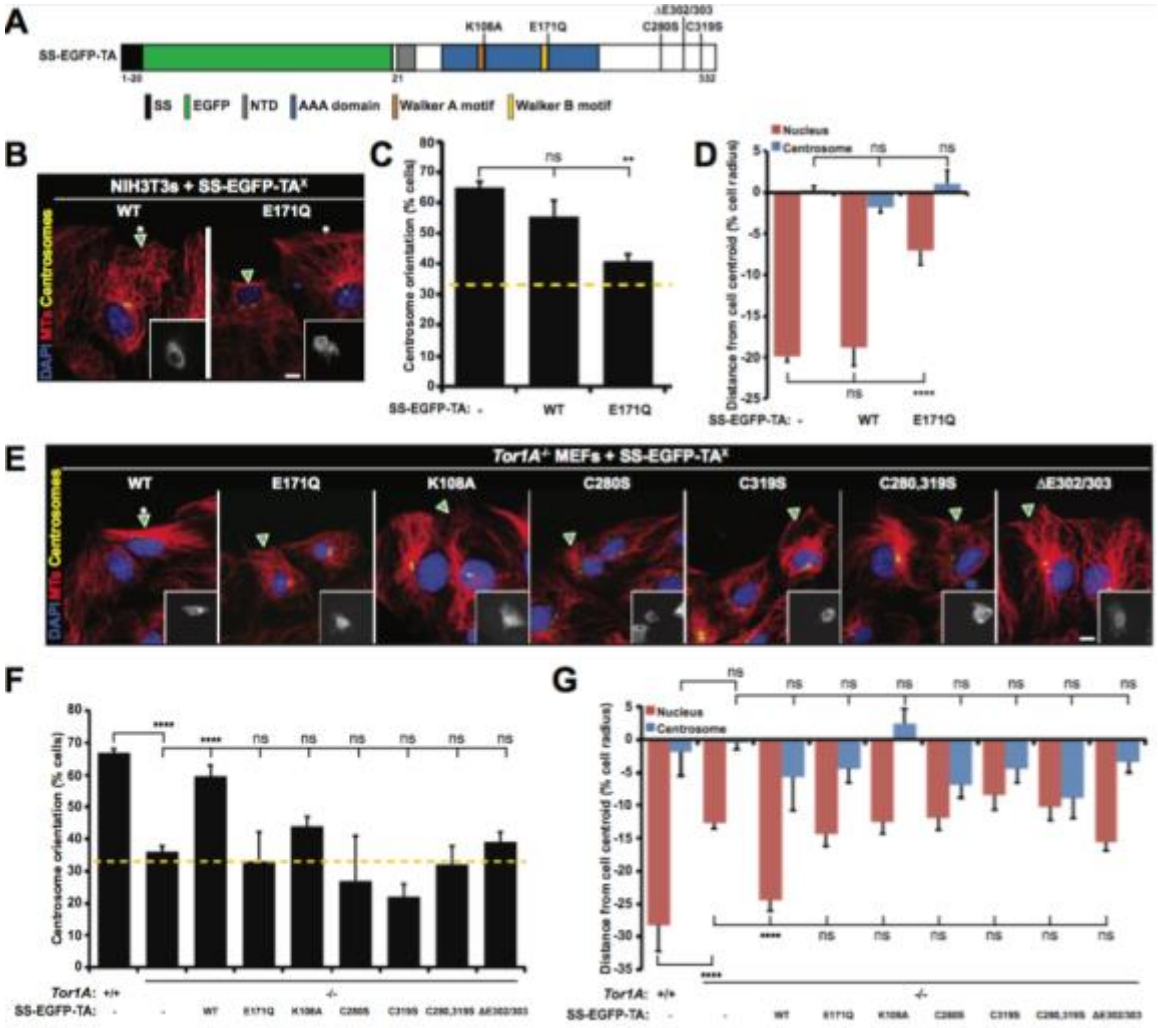

Figure 21: The redox-regulated ATPase activity of torsinA is required for rearward nuclear positioning and centrosome orientation.

Figure 21: The redox-regulated ATPase activity of torsinA is required for rearward nuclear positioning and centrosome orientation. **(A)** Diagram indicating the location of the designated mutations in the torsinA constructs used in this figure. **(B)** Representative epifluorescence images of centrosome orientation in wound-edge NIH3T3 fibroblasts expressing the indicated construct (arrowheads and inserts). **(C)** Centrosome orientation in the cells described in B. **(D)** Average centrosome and nucleus positions in the cells described in B. N ≥ 69. **(E)** Representative epifluorescence images of centrosome orientation in *Tor1A*$^{-/-}$ MEFs expressing the indicated SS-EGFP-TA^{X} construct (arrowheads and inserts). **(F)** Centrosome orientation in the cells described in E. **(G)** Average centrosome and nucleus positions in the cells described in E. N ≥ 115. The dashed yellow lines in C and F denote random centrosome orientation. Scale bars, B and E**:** 10 μm. Asterisk: oriented centrosomes, B and E. ns: non-significant, C,D, F, and G.

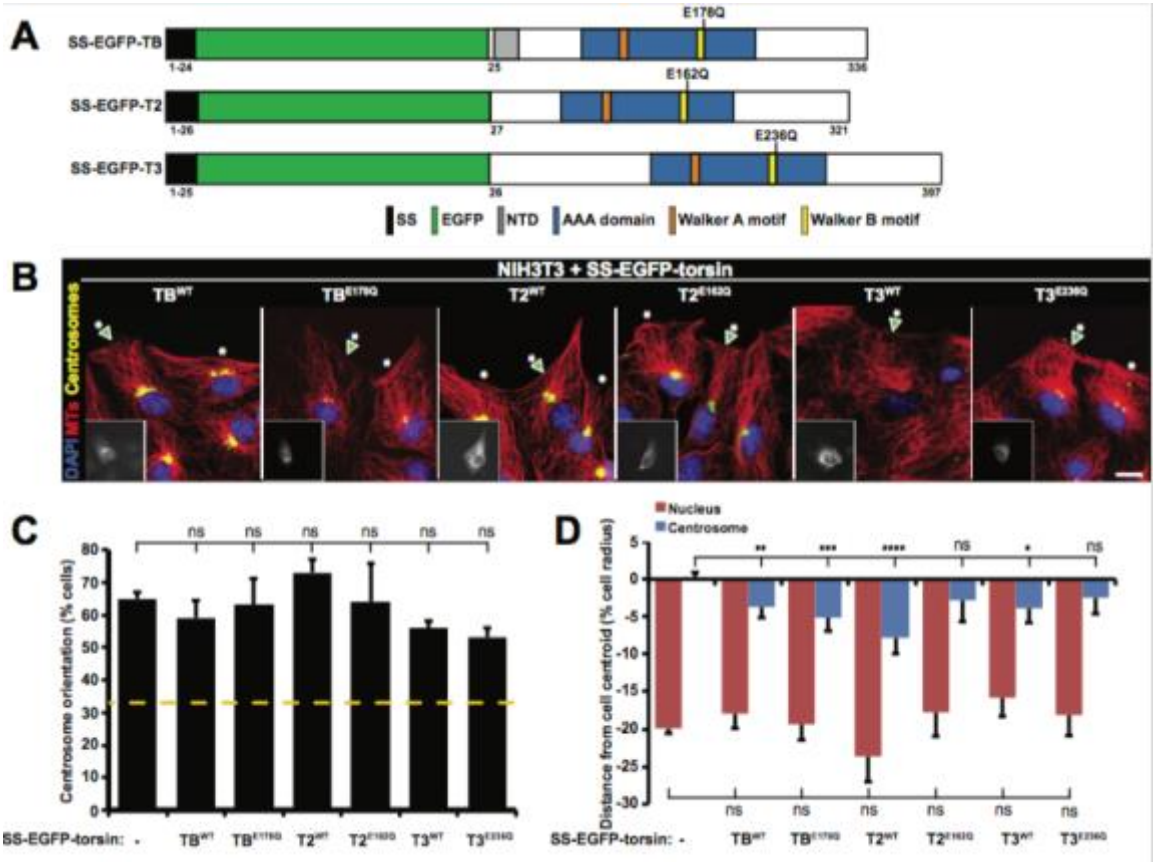

Figure 22: Testing the roles of torsinB, torsin2, and torsin3 during rearward nuclear positioning and centrosome orientation in NIH3T3 fibroblasts. (A) Diagram of the SS-EGFP-torsinB (TB), -torsin2 (T2), and torsin3 (T3) constructs used in this figure. Protein domains were identified using the SMART platform (Schultz et al., 1998). (B) Representative epifluorescence images of centrosome orientation in cells expressing the indicated SS-EGFP-torsin construct (arrowheads and inserts). Scale bar: 10 μm. Asterisk: oriented centrosomes. (C) Centrosome orientation in the cells described in B. The dashed yellow line denotes random centrosome orientation. (D) Average centrosome and nucleus positions measured from the cells described in B. N ≥ 71. ns: non-significant, C and D.

predicted to prevent ATP-binding (Goodchild and Dauer, 2004; Hanson and Whiteheart, 2005), could rescue centrosome orientation and rearward nuclear positioning in *Tor1A*$^{-/-}$ MEFs (Figs. 21A, E-G). Neither of these constructs, nor SS-EGFP-TA$^{\Delta E}$, which encodes the ATPase-defective DYT1 dystonia-causing ΔE mutation (Zhao et al., 2013), were able to rescue the centrosome orientation and nuclear positioning defects observed in the *Tor1A*$^{-/-}$ MEFs (Figs. 21A, E-G). Next, we tested the requirement for the C-terminal redox-sensitive sensor II motif (RSS), which is composed of two conserved disulfide-bond forming cysteine residues, C280 and C319, and is required for the nucleotide- and partner-binding functions of torsinA (Zhu et al., 2008; Zhu et al., 2010). We mutated each cysteine in the RSS to serine in SS-EGFP-TA either independently (SS-EGFP-TA^{C280S} and SS-EGFP-TA^{C319S}) or together (SS-EGFP-TA^{C280,319S}) and expressed the resulting constructs in *Tor1A*$^{-/-}$ MEFs (Figs. 23A and E-G). None of the cysteine mutants rescued centrosome orientation or rearward nuclear positioning (Figs. 23A, E-G). These results demonstrate that the redox-regulated ATPase activity of torsinA is required for rearward nuclear positioning during centrosome orientation in wound edge fibroblasts.

LAP1 is required for rearward nuclear movement during centrosome orientation. To determine if LAP1 or LULL1 contributed to rearward nuclear movement during centrosome orientation, we depleted each protein from NIH3T3 fibroblasts with siRNA (Figs. 24A-C). LAP1-depletion negatively impacted both centrosome

orientation and rearward nuclear positioning in cells following LPA-stimulation, while no significant effect was observed with LULL1-depletion (Figs. 23A-C). We obtained similar results with independent siRNAs directed against LAP1 and LULL1 (Figs. 24A-E). Expression of EGFP-tagged LAP1 (EGFP-LAP1^{WT}) in LAP1-depleted cells rescued centrosome orientation and rearward nuclear positioning (Figs. 23A-C). Live-cell DIC imaging revealed that the percentage of LAP1-depleted cells that displayed rearward nuclear movement and the speed of rearward nuclear movement were significantly reduced relative to controls (Figs. 23D-F). Both of these parameters were rescued by EGFP-LAP1^{WT} expression in the LAP1-depleted cells (Figs. 23D-F). Thus these results indicate that LAP1, like torsinA, is required for rearward nuclear movement during centrosome orientation and suggest that LULL1 is largely dispensable for this process.

To begin to explicate the mechanism of LAP1 function during centrosome orientation, we tested the ability of various EGFP-tagged LAP1 constructs to rescue rearward nuclear positioning during centrosome orientation in LAP1-depleted NIH3T3 fibroblasts (Figs. 24F). Neither the nucleoplasmic domain (ND) (EGFP-LAP1ND) nor the luminal domain (LD) plus TM domain (EGFP-LAP1^{LD}) of LAP1 rescued centrosome orientation (Figs. 23G-I). However, EGFP-LAP1^{LD} expression partially rescued rearward nuclear positioning in LAP1-depeleted cells (Figs. 23G-I). To further explore this result and to test the role of LAP1-

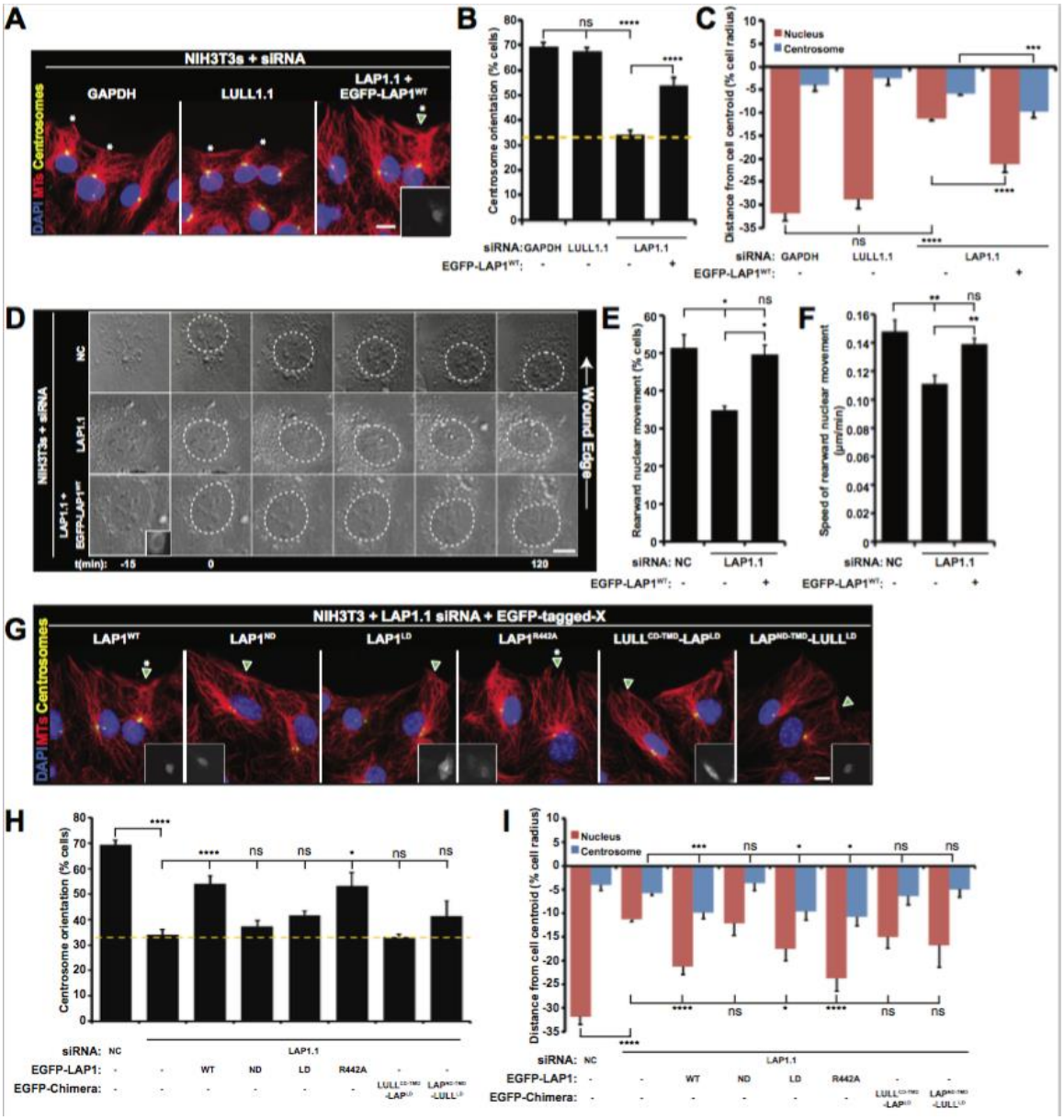

Figure 23: LAP1 is required for rearward nuclear movement during centrosome orientation.

Figure 23: LAP1 is required for rearward nuclear movement during centrosome orientation. (A) Representative epifluorescence images of centrosome orientation in NIH3T3 fibroblasts treated with siRNA. A LAP1-depleted cell expressing EGFP-LAP1^{WT} is shown (arrowhead and insert). **(B)** Centrosome orientation in the cells described in A. **(C)** Average centrosome and nucleus positions in the cells described in B. N ≥ 139. **(D)** Representative montages of DIC images of nuclear movement during centrosome orientation in NIH3T3 fibroblasts treated with NC or LAP1.1 siRNA. A DIC montage of LAP1-depleted cells expressing EGFP-LAP1^{WT} (insert) is provided. **(E)** Percentage of the cells described in D with rearward moving nuclei. **(F)** Average velocity of nuclear movement from cells described in D. **(G)** Representative epifluorescence images of centrosome orientation in LAP1-depleted NIH3T3 fibroblasts expressing the indicated EGFP-LAP1^{X} construct (arrowheads and inserts). **(H)** Centrosome orientation in the cells described in G. **(I)** Average centrosome and nucleus positions in the cells described in G. N ≥ 11. The dashed yellow lines in B and H denote random centrosome orientation. Scale bars, A and D**:** 10 µm. Asterisk: oriented centrosomes, A and G. ns: non-significant, B, C, E, F, H, and I.

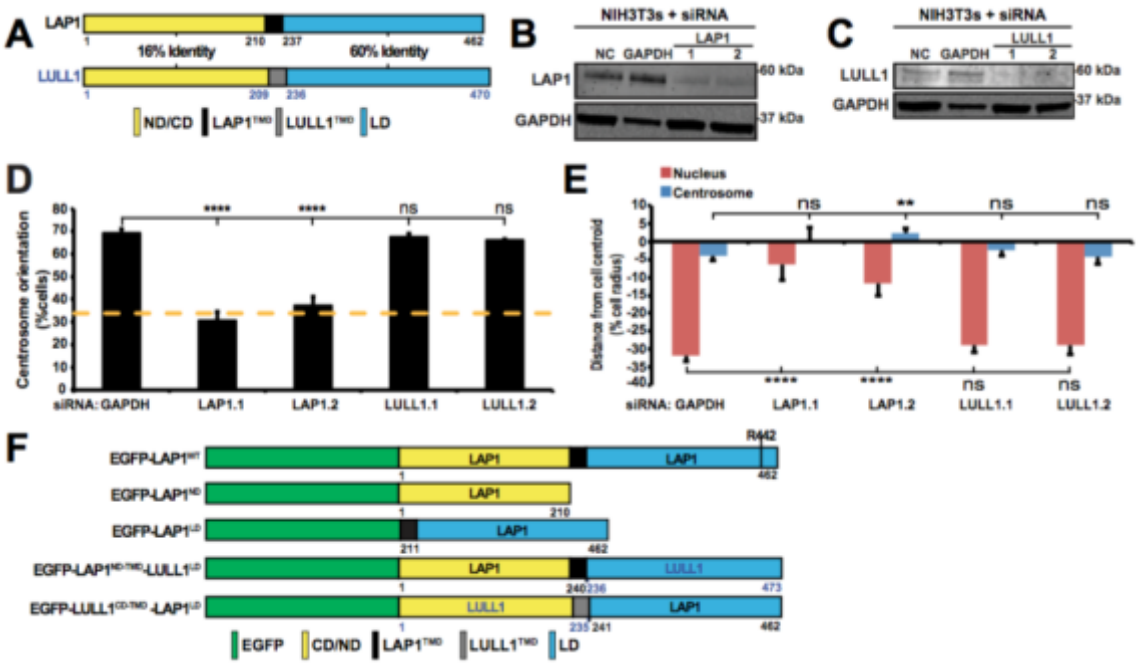

Figure 24: Validation of LAP1 and LULL1 depletion from NIH3T3 fibroblasts by various siRNAs. (A) Diagrams of the human LAP1 and LULL1 proteins. (B and C) Representative western blot of lysates from cells treated with the indicated siRNAs and probed with the indicated antibodies. (D) Centrosome orientation in cells treated with the indicated siRNAs. (E) Average centrosome and nucleus positions from the cells described in D. N ≥ 100. (F) Diagrams of the EGFP-LAP1 constructs and EGFP-tagged LAP1/LULL1 chimeric constructs used in Figs. 3H,I.

mediated stimulation of the ATPase activity of torsinA during this process, we attempted to rescue LAP1-depleted cells by expressing a LAP1 construct lacking the conserved arginine critical for stimulating the ATPase activity of torsinA (EGFP-LAP1^{R442A}) (Brown et al., 2014; Sosa et al., 2014) (Figs. 24F and 23G-I). Since EGFP-LAP1^{R442A} expression rescued both centrosome orientation and rearward nuclear positioning in LAP1-depleted cells (Figs. 23G-I), these results suggest that LAP1 promotes rearward nuclear positioning during centrosome orientation in a manner that is independent of its ability to stimulate the ATPase activity of torsinA.

As a final test of the differential requirement for LAP1 and LULL1 during centrosome orientation and rearward nuclear positioning, we fused the LULL1^{LD} to the LAP1^{ND-TMD} (EGFP-LAP1^{ND-TMD}-LULL1^{LD}) and attached the LAP1^{LD} to the cytoplasmic domain (CD) of LULL1 (EGFP-LULL1^{CD-TMD}-LAP^{LD}) (Figs. 24F). Similar constructs were previously used to show that the LAP1 ND and LULL1 CD mediate the subcellular localization of LAP1 to the INM and LULL1 to the ONM/ER, respectively (Naismith et al., 2009). Neither chimera rescued centrosome orientation or rearward nuclear positioning in the LAP1-depleted cells (Figs. 23G-I). Thus, these results show that despite being ~60% identical (Goodchild and Dauer, 2005), the LAP1^{LD} and LULL1^{LD} are not functionally equivalent. Moreover, these results suggest that the LAP1^{LD} needs to be localized at the INM in order to function during centrosome orientation.

TorsinA and LAP1 are required for TAN line assembly and persistence. Rearward nuclear movement requires N2G and SUN2 assembly into TAN lines, so we first tested whether torsinA- or LAP1-depletion affected the nuclear envelope localization and/or total protein levels of N2G and SUN2. Quantitative immunofluorescence microscopy revealed that the steady-state levels of the TAN line proteins N2G or other nuclear envelope proteins (lamin A/C, nesprin-3, SUN1) were unchanged in the nuclear envelope of torsinA- or LAP1-depleted NIH3T3 fibroblasts stimulated with LPA (Figs. 25A-D). However, a significant increase in the level of SUN2 in the nuclear envelope was observed in LAP1-depleted cells compared to controls (Figs. 25C,D). In addition, we measured a significant reduction in the nuclear envelope levels of SUN1 and N2G in *Tor1A*$^{-/-}$ relative to *Tor1A*$^{+/+}$ MEFs (Figs. 25E-F). In contrast, no significant differences were observed in the total protein levels of N2G, nesprin-3, SUN1, and SUN2 in NC-, GAPDH-, torsinA-, or LAP1-depleted cells (Figs. 25G-J). Similar results were obtained in *Tor1A*$^{+/+}$ vs. *Tor1A*$^{-/-}$ MEFs, though there was a significant decrease in N2G and SUN1 as well as a slight increase in SUN2 levels in the absence of torsinA (Figs. 25K-L). Together, these results indicate that the role of torsinA and LAP1 during rearward nuclear movement might be separate from its role in regulating the levels or localization of LINC complex components.

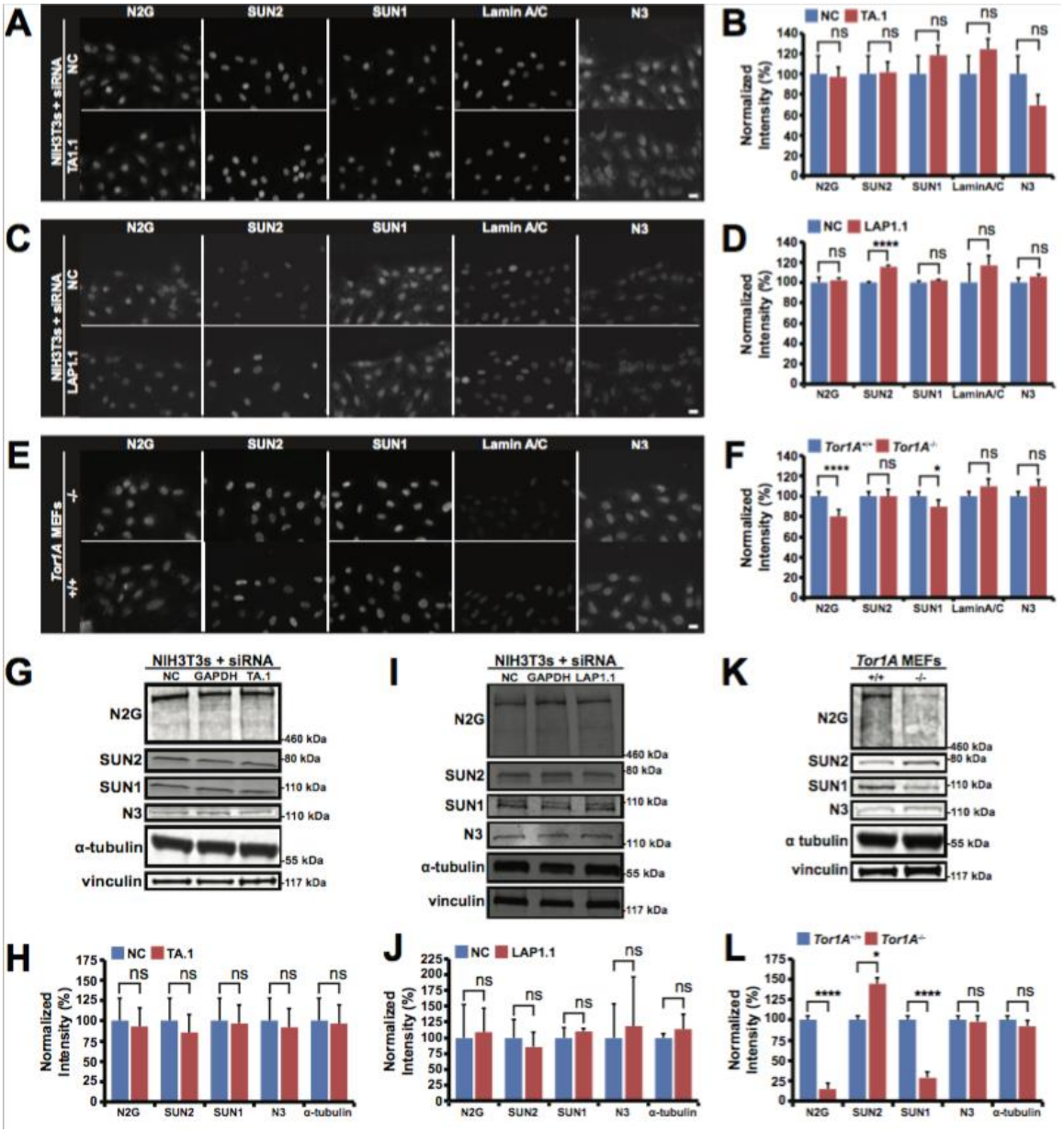

Figure 25: Quantification of the nuclear and biochemical levels of TAN line components in torsinA- and LAP1-depleted NIH3T3 fibroblasts as well as Tor1A-/- MEFs.

Figure 25: Quantification of the nuclear and biochemical levels of TAN line components in torsinA- and LAP1-depleted NIH3T3 fibroblasts as well as *Tor1A*$^{-/-}$ MEFs. (A, C, and E) Representative epifluorescence images of cells treated with siRNA and stained with the indicated antibodies. Scale bars, A, C, and E: 20 μm. **(B, D, F)** Quantification of the nuclear envelope protein levels from the cells described in A, C, and E, respectively. N ≥ 3. **(G, I, K)**. Representative western blots of lysates from the indicated cells probed with the indicated antibodies. **(H, J, and L)** Quantification of protein levels from the experiments described in G, J, and K, respectively. ns: non-significant, B, D, F, H, J, and L.

We next examined the effect of torsinA- and LAP1-depletion on the ability of wound edge NIH3T3 fibroblasts to assemble TAN lines. We expressed the TAN line marker, EGFP-mini-N2G, in torsinA-depleted or control cells stimulated with LPA. Linear arrays of EGFP-mini-N2G are considered TAN lines if they co-localize with dorsal perinuclear actin cables (Fig. 26A) (Luxton et al., 2010). Significantly fewer torsinA- and LAP1-depleted cells exhibited TAN lines as compared to control cells (Figs. 26A-B). The number of TAN lines observed per cell was also reduced when either torsinA or LAP1 were depleted (Fig. 26C). In addition, live-cell imaging revealed that the persistence of the TAN lines was significantly reduced in torsinA- and LAP1-depleted cells relative to controls (Figs. 26D-E). This impaired persistence was not due to the inability of SUN2 to properly localize to linear arrays of mini-N2G in the absence of torsinA function, as the percentage of TAN lines containing endogenous SUN2 was unaffected by torsinA-depletion or the expression of SS-EGFP-TA^{E171Q} (Fig. 27). Thus, these results demonstrate that both torsinA and LAP1 are required for the assembly of stable TAN lines.

To determine if TAN lines themselves may be sites of torsinA function, we asked if SS-EGFP-TA^{E171Q} preferentially localized to TAN lines in comparison to SS-EGFP-TA^{WT}, since similar ATP-hydrolysis defective Walker B motif mutations are often used to trap the interaction between AAA+ proteins and their substrates (Hanson and Whiteheart, 2005). Quantification of the localization of either

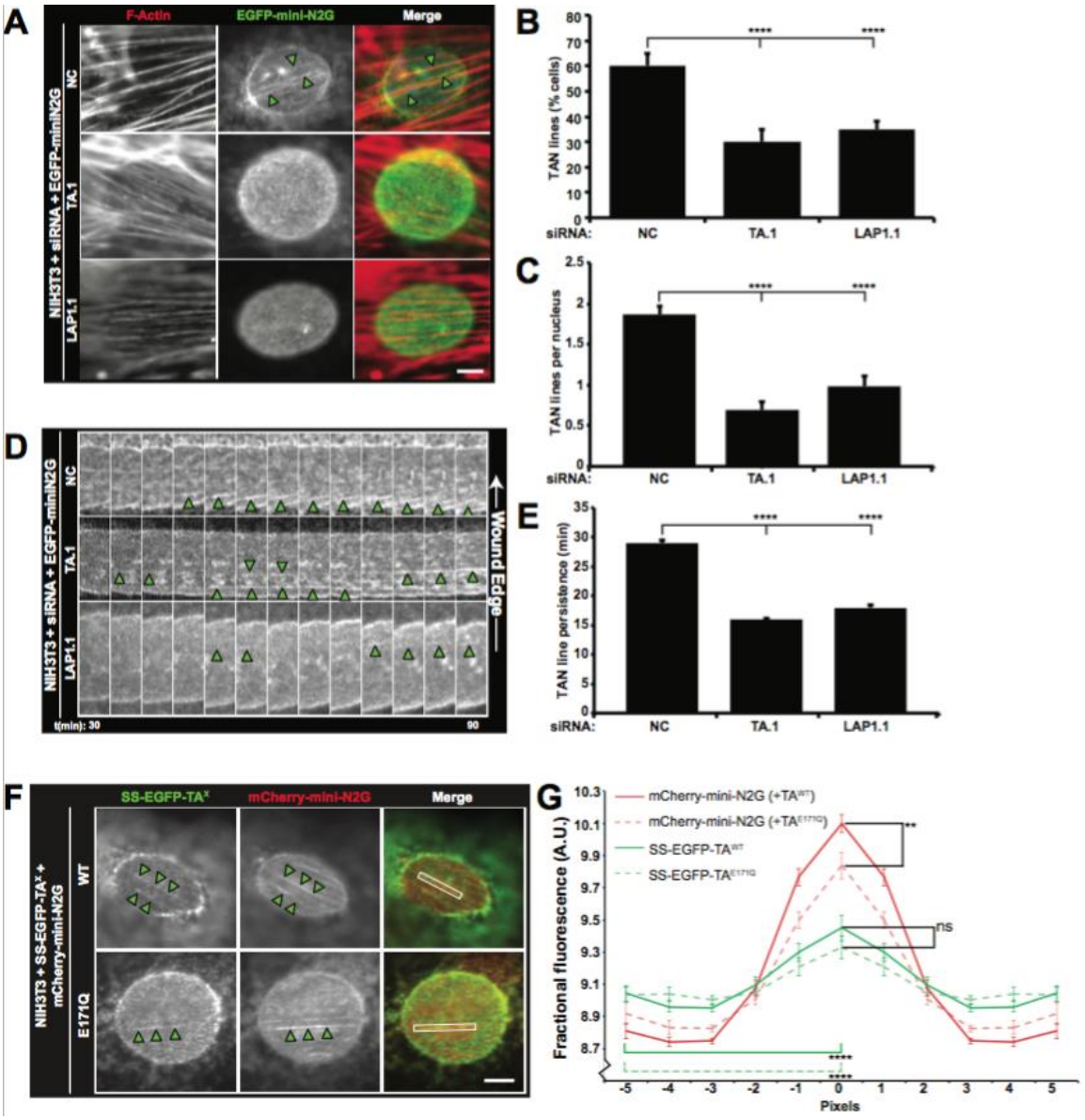

Figure 26: The assembly of stable TAN lines requires both torsinA and LAP1.

Figure 26: The assembly of stable TAN lines requires both torsinA and LAP1. (A) Representative epifluorescence images of nuclei in wound-edge NIH3T3 fibroblasts treated with siRNA and expressing EGFP-mini-N2G taken 1 hr. following LPA-stimulation. Cells were stained for F-actin (red) and EGFP (green). Arrowheads: TAN lines. **(B)** Average number of cells with TAN lines quantified from the cells described in A. N ≥ 150. **(C)** Average number of TAN lines per nucleus quantified from the cells described in A. **(D)** Representative kymographs of EGFP-mini-N2G fluorescence in wound-edge NIH3T3 fibroblasts treated with siRNA. Each panel is 0.2 μm. Arrowheads: TAN lines. Time after LPA addition is in mins. **(E)** Average TAN line persistence quantified from the experiments described in D. N ≥ 13. **(F)** Representative epifluorescence images of mCherry-mini-N2G TAN lines in NIH3T3 fibroblasts also expressing the indicated SS-EGFP-TA^{X} construct. Scale bars, A and F: 5 μm. **(G)** Quantification of SS-EGFP-TA^{X} recruitment to TAN lines by line-scan analysis. ns: non-significant, B, C, F, and G.

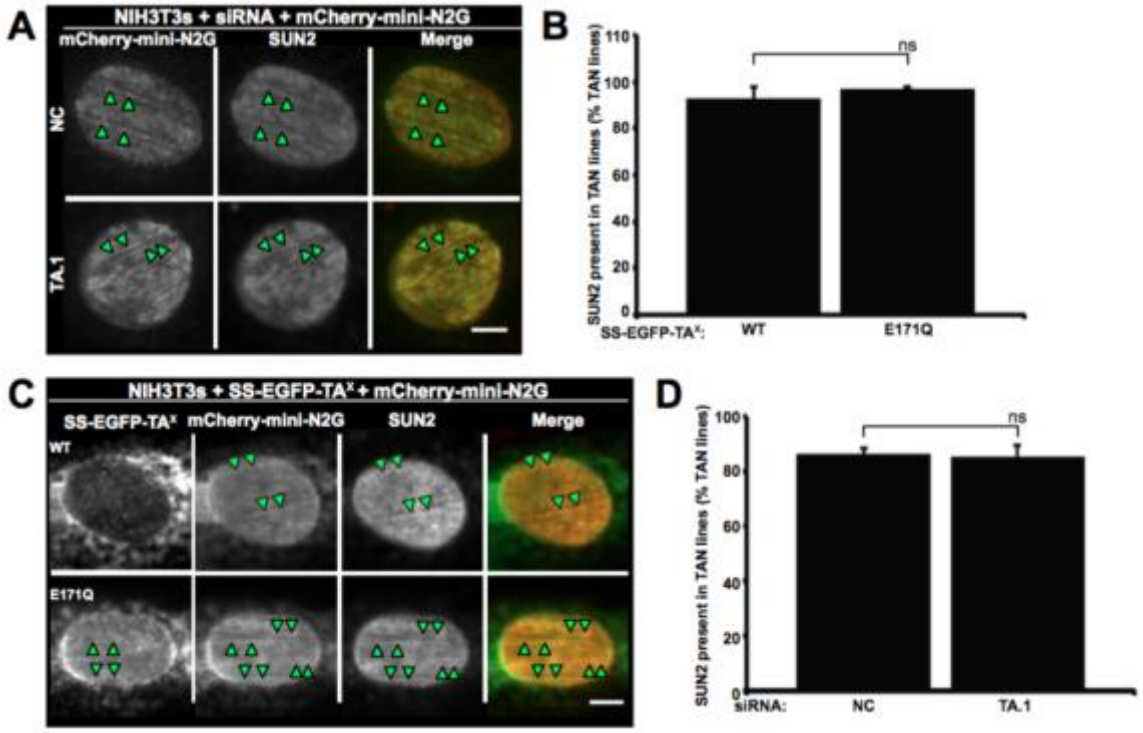

Figure 27: Quantification of endogenous SUN2 recruitment to TAN lines in NIH3T3 fibroblasts with impaired TA function. (A) Representative epifluorescence images of cells treated with the indicated siRNAs and expressing mCherry-mini-N2G. (B) Quantification of the percentage of TAN lines with SUN2 recruitment from the cells described in A. N ≥ 81. (C) Representative epifluorescence images of cells expressing mCherry-mini-N2G along with the indicated SS-EGFP-TA construct. Representative epifluorescence images of cells treated with the indicated siRNAs and expressing mCherry-mini-N2G. (D) Quantification of the percentage of TAN lines with SUN2 recruitment from the cells described in C. N ≥ 84. Scale bars in A and C: 5 μm.

construct to mCherry-mini-N2G TAN lines in serum-starved wound edge cells stimulated with LPA demonstrated a significant enrichment of torsinA^{WT} and torsinA^{E171Q} on TAN lines relative to an adjacent TAN line-free area on the nuclear envelope (Figs. 26F-G). In addition, we found that the presence of SS-EGFP-TA^{E171Q} resulted in a significant reduction in the amount of mCherry-mini-N2G signal measured in TAN lines as compared to TAN lines with SS-EGFP-TA^{WT} (Fig. 26G). These results imply that TAN lines may contain substrates of torsinA, the remodeling of which is necessary for TAN line assembly and persistence.

TorsinA is required for the dynamics of N2G and SUN2 within the nuclear envelope. To assess how torsinA might contribute to TAN line assembly and persistence, we performed fluorescence recovery after photobleaching (FRAP) to measure the mobility and dynamics of previously described constructs encoding EGFP-tagged LINC complex components mini-N2G, nesprin-3α, nesprin-3β, SUN1, and SUN2 within the nuclear envelope of *Tor1A*$^{+/+}$ and *Tor1A*$^{-/-}$ MEFs (Fig. 28A) (Luxton et al., 2010; Wilhelmsen et al., 2005; Östlund et al., 2009). Of the five constructs tested, only EGFP-mini-N2G exhibited a difference in the absence of torsinA. Specifically, the $t_{1/2}$ of EGFP-mini-N2G recovery after photobleaching was significantly increased in *Tor1A*$^{-/-}$ MEFs relative to controls (Fig. 28B). Consequently, these results suggest that torsinA is required for the proper mobility of EGFP-N2G within the nuclear envelope.

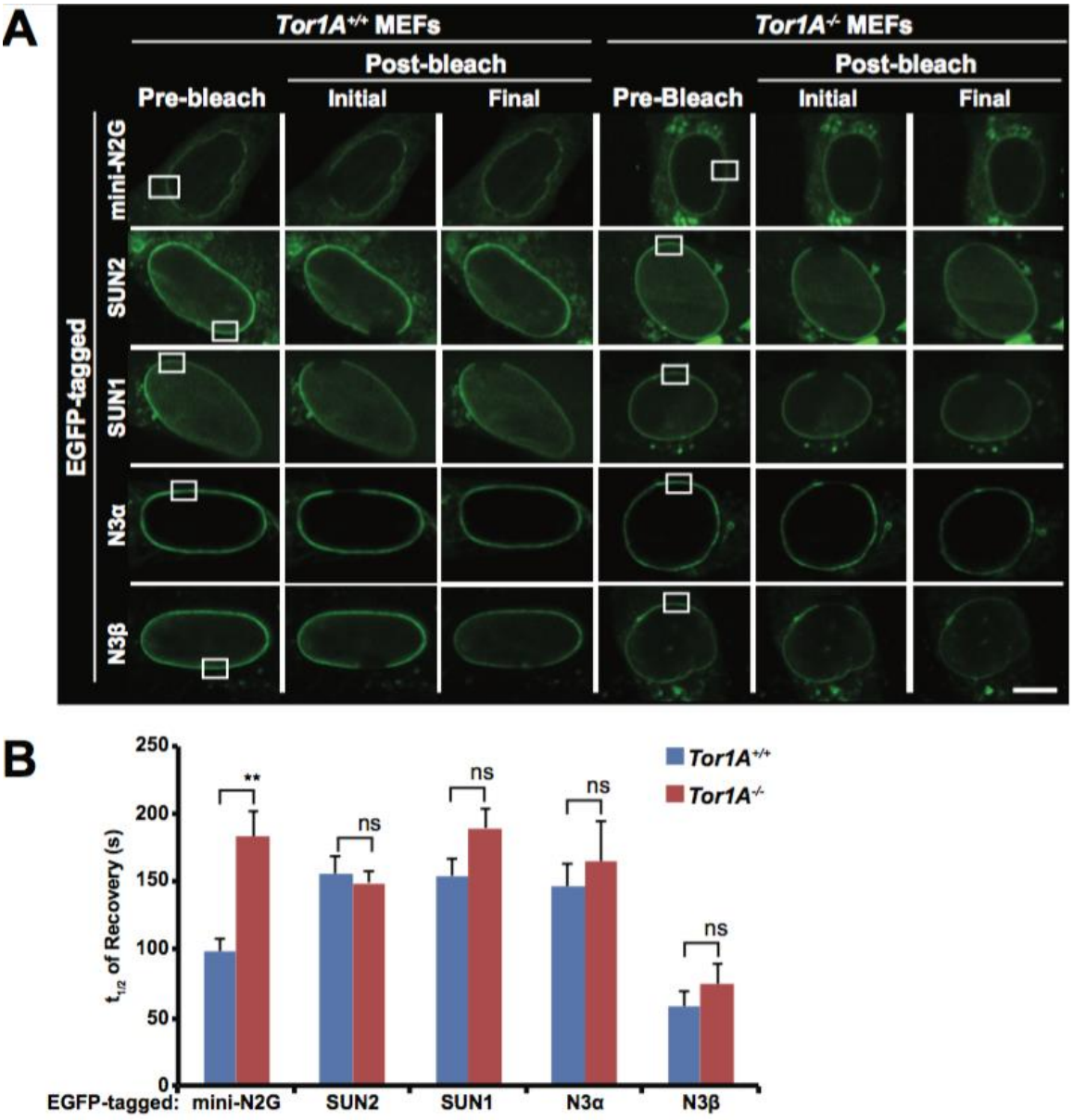

Figure 28: TorsinA affects the dynamics of EGFP-mini-N2G in the nuclear envelope.

Figure 28: TorsinA affects the dynamics of EGFP-mini-N2G in the nuclear envelope. (A) Representative confocal fluorescence images of *Tor1A*$^{+/+}$ and *Tor1A*$^{-/-}$ MEFs expressing the indicated construct and subjected to FRAP. The white box indicates the bleached region of interest. Scale bar**:** 10 µm. (**B)** t1/2 of Recovery quantification from the experiments described in A. N3: nesprin-3. N ≥ 3. ns: non-significant.

TorsinA and LAP1 are required for the retrograde flow of dorsal perinuclear actin cables. Since the reorganization of N2G and SUN2 into TAN lines requires the formation of dorsal perinuclear actin cables, which do not require either N2G or SUN2 (Folker et al., 2011; Luxton et al., 2010), we tested the effect of torsinA-depletion on the assembly of these cables in LPA-stimulated NIH3T3 fibroblasts. We did not detect a significant difference in the number of dorsal perinuclear actin cables in torsinA-depleted or control cells at 0, 60, or 120 minutes following LPA stimulation (Figs. 29A-B). While similar results were obtained in LAP1-depleted cells, they exhibited a significant reduction in cable numbers at the 0 minute time point relative to control cells. Thus, neither torsinA nor LAP1 were required for the assembly of the actin cables responsible for rearward nuclear movement.

We then tested the ability of dorsal perinuclear actin cables in torsinA- or LAP1-depleted NIH3T3 fibroblasts to undergo retrograde flow by monitoring actin cables with the live cell actin probe, Lifeact-mCherry (Riedl et al., 2008). The speed of retrograde flow of the dorsal perinuclear actin cables was reduced over 50% in torsinA- and LAP1-depleted cells relative to control cells, while retrograde flow of wound-edge actin cables was unaffected (Figs. 29C-D). Because overexpression of SS-EGFP-TA^{E171Q} inhibited rearward nuclear positioning in NIH3T3 fibroblasts, we tested the effect of its expression on retrograde actin flow in these cells. Similar to what we observed in torsinA- or LAP1-depleted cells, the

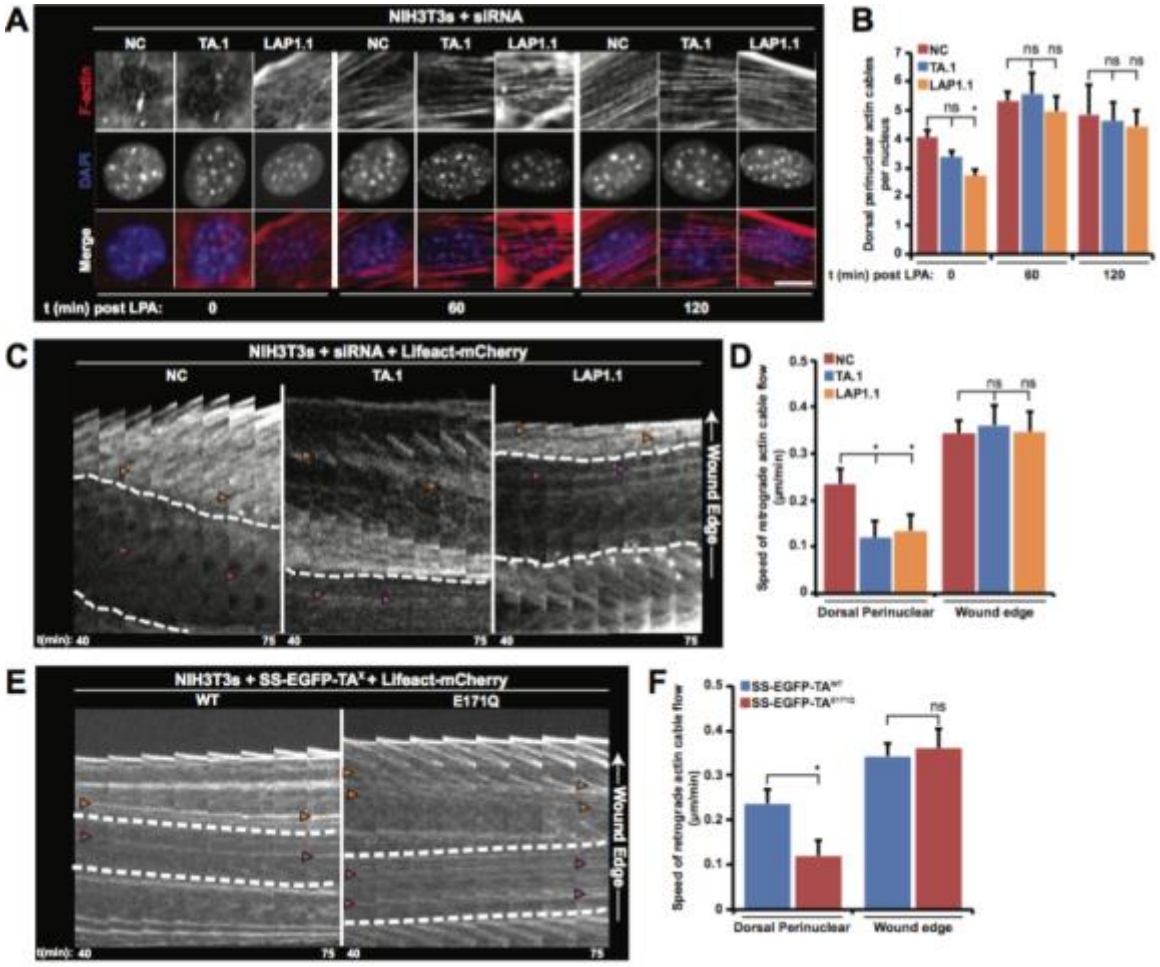

Figure 29: The retrograde flow of dorsal perinuclear actin cables during rearward nuclear movement requires torsinA and LAP1.

Figure 29: The retrograde flow of dorsal perinuclear actin cables during rearward nuclear movement requires torsinA and LAP1. (A) Representative epifluorescence images of nuclei in NIH3T3 fibroblasts treated with indicated siRNA taken at 0, 60, and 120 min after LPA-treatment. Scale bar: 10 μm. **(B)** Quantification of the number of dorsal perinuclear actin cables from the cells described in A. N ≥ 3. **(C)** Kymographs of retrograde actin cable flow in wound-edge NIH3T3 fibroblasts treated with indicated siRNA and expressing Lifeact-mCherry. The dashed line represents the edges of the nucleus. Each panel is 0.2 μm. Time after LPA addition is in mins. **(D)** Speed of actin cable retrograde flow quantified from the cells described in C. N ≥ 15. **(E)** Kymographs of retrograde actin flow in NIH3T3 fibroblasts expressing the indicated construct. Time after LPA addition is in mins. Each panel is 0.2 μm. **(F)** Speed of actin cable retrograde flow determined from the cells described in E. N ≥ 10. Yellow arrowheads (C and E): actin cables at the leading edge. Pink arrowheads (C and E): dorsal perinuclear actin cables. ns: non-significant, B, D, and F.

DISCUSSION

We show rearward nuclear movement during centrosome orientation requires torsinA and its activator LAP1. Together, torsinA and LAP1 promote TAN line assembly and the retrograde flow of dorsal perinuclear actin cables, both of which are critical for rearward nuclear movement (Fig. 30). We also demonstrate that torsinA is necessary for the proper accumulation of EGFP-mini-N2G in TAN lines, perhaps because without torsinA, the mobility of EGFP-mini-N2G within the nuclear envelope is reduced. Thus, our results establish torsinA as a key regulator of LINC complex-dependent nuclear-cytoskeletal coupling and actin retrograde flow.

Functional specification of torsin proteins. While we cannot formally conclude that the other lumenal torsins we tested are not required for centrosome orientation, our data suggests that torsinA plays a more significant role than torsinB, torsin2, or torsin3 during this process. This functional specificity for torsinA is unexpected, as torsinA and torsinB are known to function redundantly to maintain normal nuclear membrane morphology in non-neuronal cells (Kim et al., 2010). In addition, torsinB, torsin2, and torsin3 all interact with LAP1 (Hewett et al., 2004; Jungwirth et al., 2010; Kim et al., 2010). However, it is highly likely that different torsins perform specialized cellular functions as indicated by the fact that ATP-hydrolysis-defective, substrate-trap torsinB, torsin2, and torsin3

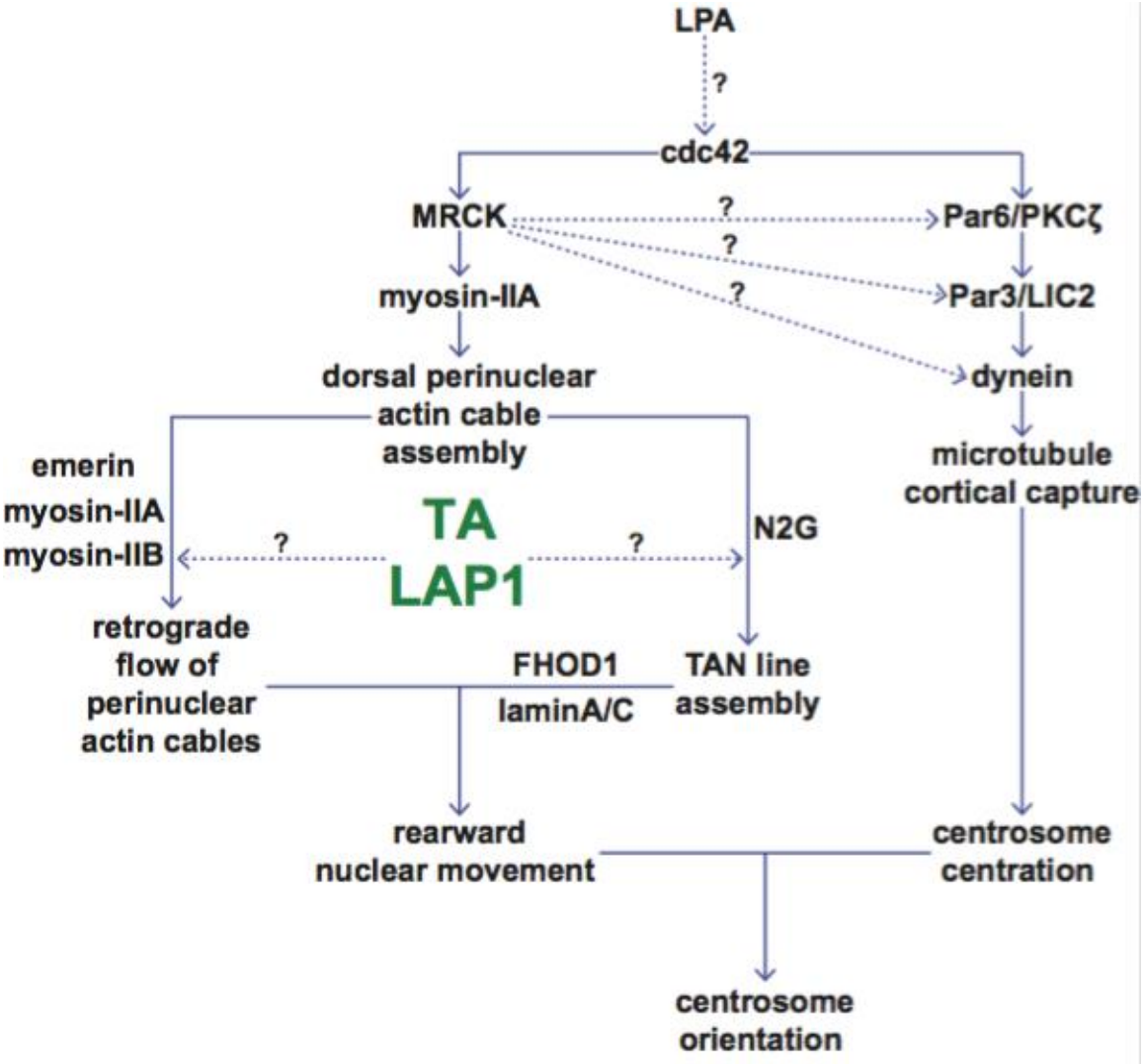

Figure 30: TorsinA and LAP1 are critical regulators of rearward nuclear movement. Model displaying the potential positions of torsinA and LAP1 within the two pathways known to contribute to proper centrosome orientation (Gomes et al., 2005; Luxton et al., 2010; Schmoranzer et al., 2009). MRCK is sufficient to stimulate centrosome orientation and so may also regulate the centrosome centration pathway (dotted arrows) (Gomes et al., 2005).

mutants accumulate to varying degrees within the perinuclear space (Hewett et al., 2004; Jungwirth et al., 2010; Kim et al., 2010). Moreover, the ATPase activity of these torsins is differentially stimulated by LAP1^{LD} or LULL1^{LD} *in vitro* (Zhao et al., 2013). The significant, rearward displacement of the centrosome we observed in NIH3T3 fibroblasts following the over-expression of SS-EGFP-tagged torsinB^{WT}, torsinB^{E178Q}, torsin2^{WT}, and torsin3^{WT} may also hint at functional specificity between torsin proteins. We hypothesize that torsinB, torsin2, or torsin3 may act to control microtubule dynamics, which are critical for proper centrosome positioning in migrating fibroblasts (Gomes et al., 2005; Schmoranzer et al., 2009). Specifically, these torsins may regulate a growing list of known microtubule- or microtubule motor-associated membrane proteins that traverse the ER/ONM (Gurel et al., 2014).

TorsinA-LAP1 holoenzyme-mediated rearward nuclear movement. We show that the redox-regulated ATPase activity of torsinA is required for rearward nuclear movement during centrosome orientation. We also demonstrate that mutations in torsinA (ΔE and RSS) that impair LAP1- or LULL1-binding (Naismith et al., 2009; Zhao et al., 2013; Zhu et al., 2010) are unable to rescue rearward nuclear movement in *Tor1A*$^{-/-}$ MEFs. The small amount of centrosome orientation we observed following expression of SS-EGFP-TA^{E171Q} in NIH3T3 fibroblasts vs. the inability of this construct to rescue centrosome orientation in *Tor1A*$^{-/-}$ MEFs above back ground levels, may be explained by the fact that AAA+ proteins

typically act as ring-shaped hexamers (Hanson and Whiteheart, 2005). Therefore, the presence of torsinA^{WT} in NIH3T3 fibroblasts could compensate for the ATP-hydrolysis-defective E171Q mutation depending on the ratio of torsinA^{WT} to torsinA^{E171Q} in a single ring. However, expression of SS-EGFP-TA^{E171Q} in the *Tor1A*$^{-/-}$ would result in all torsinA rings being solely composed of ATP-hydrolysis defective torsinA and hence non-functional.

In addition, we provide evidence for the lack of functional redundancy between LAP1 and LULL1 during rearward nuclear movement despite the ability of both of their LDs to stimulate the ATPase activity of torsinA *in vitro* (Zhao et al., 2013). The requirement for LAP1 during rearward nuclear movement necessitated that its LD be tethered at the INM. Unexpectedly, we found that the critical arginine finger in the LAP1^{LD} (R442) was dispensable for LAP1 function during rearward nuclear movement. However, it is important to note that the effect of the arginine finger on the ability of the LAP1^{LD} to stimulate torsinA's ATPase activity *in vitro* varied greatly between two independent reports (Brown et al., 2014; Sosa et al., 2014). Since these measurements were performed in the absence of a torsinA substrate, they may not accurately reflect of torsinA activity in cells.

Our *in vivo* results concerning the critical nature of this conserved LAP1 arginine implies that LAP1 may perform other functions in addition to its ability to stimulate torsinA ATPase activity. It is possible that the stimulation of torsinA by the

LAP1^{LD} is not important for rearward nuclear movement. Unidentified substrates and/or an additional activator within the perinuclear space may stimulate torsinA within this subcellular compartment, which would be consistent with the inability of either SS-EGFP-TA^{E171Q} or SS-EGFP-TA^{K108A} to rescue rearward nuclear positioning or centrosome orientation in *Tor1A*$^{-/-}$ MEFs. Another possible explanation for our results would be that EGFP-LAP1^{R442A} retains enough activity to stimulate ATP hydrolysis by torsinA in LAP1-depleted NIH3T3 fibroblasts. This would be in line with the modest effect of mutating the conserved arginine to alanine reported by Sosa et al. in their *in vitro* experiments (Sosa et al., 2014). Recently, a high-resolution crystal structure of torsinA in complex with the LULL1^{LD} was solved, which will provide a critical structural framework for future experiments designed to further test the structure-function relationship between torsinA and LAP1 (Demircioglu et al., 2016).

TorsinA and TAN line assembly. TorsinA has been proposed as a regulator of LINC complex assembly and function (Atai et al., 2012; Gerace, 2004; Saunders and Luxton, 2016). However, the mechanism underlying this proposed function remain unclear aside from the reports of an interaction between torsinA and the KASH domains from nesprin-1, -2, and -3 (Nery et al., 2008) as well as the sensitivity of N2G, nesprin-3, and SUN2 nuclear envelope localization to the levels of torsinA (Nery et al., 2008; Vander Heyden et al., 2009). While we detected a significant reduction in the nuclear envelope localization of SUN1 and

N2G, we did not detect altered levels of nesprin-3, and SUN2 in the complete absence of torsinA. Furthermore, we were unable to detect any changes in either the nuclear envelope localization or levels of these proteins following torsinA- or LAP1-depletion, with the exception of elevated nuclear envelope SUN2 levels following LAP1-depletion. Our inability to detect a significant reduction in the levels of N2G and SUN1 in torsinA-depleted NIH3T3 fibroblasts may result from an incomplete knockdown, consistent with previous reports of torsinA being a very stable protein (Giles et al., 2008). Since centrosome orientation and rearward nuclear movement were both inhibited in the *Tor1A*$^{-/-}$ MEFs as well as torsinA- or LAP1-depleted NIH3T3 fibroblasts, we do not believe that the changes in N2G, SUN1, or SUN2 levels reflect a general function for torsinA in controlling the stability or localization of these proteins. Instead, we propose that torsinA regulates the mobility of N2G by acting as a molecular chaperone to structurally remodel N2G-containing protein complexes within the nuclear envelope.

This hypothesis is supported by our results demonstrating that torsinA and LAP1 are required for the assembly of stable TAN lines, which are linear arrays of LINC complexes composed of N2G and SUN2 (Luxton et al., 2010; Luxton et al., 2011). In addition, the localization of torsinA to TAN lines further strengthens the connection between torsinA and N2G-containing protein complexes and raises the possibility that torsinA may act directly in the assembly of TAN lines. While

we did measure a significant enrichment of torsinA levels in TAN lines as compared to adjacent TAN line-free regions of the nuclear envelope, we did not see a preferential accumulation of torsinA^{E171Q} relative to torsinA^{WT} in TAN lines. Instead, we found a slight but significant decrease in the amount of torsinA^{E171Q} present in TAN lines as compared to torsinA^{WT}. This result indicates that the ability of torsinA to localize to TAN lines may be somewhat sensitive to its nucleotide state and that TAN lines themselves may not be substrates for torsinA. Nevertheless, the presence of torsinA^{E171Q} in TAN lines did result in a significant reduction of the amount of mini-N2G in these structures relative to the mini-N2G levels measured in the presence of torsinA^{WT}.

We offer the following potential explanation for the effect of torsinA^{E171Q} on mini-N2G levels in TAN lines. TorsinA^{E171Q} may preferentially interact with and structurally remodel a previously unidentified torsinA substrate important for controlling the mobility of N2G within the nuclear envelope and hence the assembly of stable TAN lines. We predict that this substrate is either N2G itself, which would be consistent with the previous report of an interaction between torsinA and the KASH domains from nesprin-1, -2, and -3 (Nery et al., 2008), or another N2G-interacting protein. Supporting evidence for this hypothesis is provided by our FRAP experiments, which revealed a significantly increased $t_{1/2}$ of recovery for EGFP-mini-N2G in the absence of torsinA, suggesting that torsinA

is needed for the proper assembly dynamics of N2G-containing LINC complexes required for TAN line assembly.

Previously, we showed that the KASH peptide was necessary and sufficient to immobilize EGFP-mini-N2G in the nuclear envelope of MEFs (Östlund et al., 2009). In addition, we demonstrated that SUN2-depletion significantly decreased the *t1/2* of EGFP-mini-N2G recovery while SUN1-depletion had no effect (Östlund et al., 2009). Although the total levels of N2G, SUN1, and SUN2 were significantly altered in the *Tor1A*$^{-/-}$ MEFs, we do not believe that these alterations are responsible for the increased $t_{1/2}$ of EGFP-mini-N2G we measured in these cells. For example, if reduced N2G levels were to create free binding sites within the perinuclear space for EGFP-mini-N2G, then this would apply to all nesprin proteins given the promiscuous ability of KASH peptides to interact with SUN1 and SUN2 (Stewart-Hutchinson et al., 2008). A similar argument could apply to the elevated SUN2 levels we observed in the *Tor1A*$^{-/-}$ MEFs, as this would also increase the number of potential nesprin-binding sites. Our inability to detect significant differences in EGFP-nesprin-3α/β mobility in the *Tor1A*$^{-/-}$ MEFs, which also interact with SUN1 and SUN2 (Ketema et al., 2007), strongly suggests that torsinA selectively regulates the mobility of N2G within the perinuclear space. Further, the lack of change in EGFP-SUN1 or EGFP-SUN2 mobility demonstrates that the absence of torsinA does not influence the number of

EGFP-mini-N2G binding sites despite elevated SUN2 and decreased SUN1 levels.

Based on these results, we postulate two potential direct mechanisms for how torsinA controls TAN line assembly. In the first, torsinA may promote the turnover of N2G-containing LINC complexes by dissociating the lumenal N2G KASH peptide from SUN2. In the second, the previously reported torsinA-KASH domain interaction (Nery et al., 2008) may preclude SUN protein-binding, which would contribute to N2G mobility within the nuclear envelope. It is important to note that in order for either of these hypotheses to be feasible, torsinA would have to act from a position near the ONM. However, using our EGFP-tagged LAP1/LULL1 chimeric constructs, we show that the $LAP1^{LD}$ needs to be anchored at the INM via the $LAP1^{ND\text{-}TMD}$ in order to rescue rearward nuclear positioning and centrosome orientation in LAP1-depleted NIH3T3 fibroblasts. Since the distance between the ONM and INM is ~30-50 nm (Cain and Starr, 2015; Crisp et al., 2006; Naismith et al., 2004), this would necessitate torsinA being able to dissociate from the inner leaflet of the INM and then diffuse to the ONM where it could access the N2G KASH domain and/or the SUN domain of SUN2. Interestingly, a small population of torsinA has been shown to be soluble within the ER lumen/perinuclear space in addition to a large membrane-associated population of torsinA using cellular fractionation (Vander Heyden et al., 2009; Vander Heyden et al., 2011). Furthermore, torsinA was recently shown to

undergo a proteolytic processing event during B cell activation, resulting in the cleavage of its hydrophobic N-terminus, which mediates the monotopic association of torsinA with the inner leaflet of ER/nuclear envelope membrane (Zhao et al., 2016). We hypothesize that in addition to stimulating the ATPase activity of torsinA, the interaction between torsinA and the LAP1^{LD} or the LULL1^{LD} may serve to regulate the membrane-association of torsinA thereby allowing it access to the ONM.

Alternatively, torsinA may indirectly influence TAN line assembly by its recently described role in regulating lipid metabolism (Grillet et al., 2016). For example, changes in the lipid composition of the nuclear envelope could potentially explain the reduced mobility of EGFP-mini-N2G we observed in the *Tor1A*$^{-/-}$ MEFs. However, such a global alteration in the biophysical nature of the nuclear envelope would most likely cause pleiotropic effects on the mobility of multiple nuclear envelope membrane proteins. While we did not find alterations in the mobility of the five other nuclear envelope membrane proteins we measured here, it remains a formal possibility that torsinA regulates the metabolism of lipids that are specifically involved in N2G mobility. Clearly, future *in vitro* biochemical experiments are necessary to differentiate between these direct and indirect potential mechanisms of torsinA-mediated regulation of N2G.

TorsinA is a novel regulator of dorsal perinuclear retrograde actin flow. Previously, torsinA had been implicated in the regulation of the actin cytoskeleton (Hewett et al., 2006; Muraro and Moffat, 2006). Our finding that torsinA is required for the retrograde flow of dorsal perinuclear actin cables and not their assembly extends these results and offers two new insights: 1) torsinA controls the actin cytoskeleton from within the perinuclear space; and/or 2) retrograde actin flow at different subcellular locations is subject to differential regulation. To control retrograde actin flow from its lumenal residence, torsinA must interact with and regulate a transmembrane ER or ONM protein involved in the regulation of the actin cytoskeleton. LAP1 is a strong candidate since our results show that it is also required for this process. Recently, LAP1ND was reported to directly interact with the ND of emerin, which is primarily concentrated in the INM but also found at the ONM (Chang et al., 2013; Salpingidou et al., 2007; Shin et al., 2013). Emerin interacts with actin and non-muscle myosin IIB within the cytoplasm and is also required for rearward nuclear movement during centrosome orientation in migrating fibroblasts (Chang et al., 2013). Future efforts towards mapping the emerin-binding site(s) in LAP1ND will enable the role of the LAP1-emerin interaction during centrosome orientation to be addressed. Alternatively, torsinA may control the actin cytoskeleton through a different LAP1-binding partner or a non-LAP1 nuclear membrane protein. Analysis of the recently published LAP1 interactome (Serrano et al., 2016) together with proteomics-based approaches to identify novel LAP1- and torsinA-interacting

proteins should help lead to the identification of potential torsinA substrates required for rearward nuclear movement during centrosome orientation.

TorsinA-mediated cell polarity and DYT1 dystonia. In summary, our data support the hypothesis that torsinA plays a critical evolutionarily conserved role in the establishment and/or maintenance of cell polarity (Basham and Rose, 1999; Nery et al., 2008). When considered together with the recent report of fibroblasts derived from DYT1 dystonia patients being defective centrosome orientation and directional migration (Nery et al., 2014), our results highlight the possible connection between defective cell polarity and DYT1 dystonia. While DYT1 dystonia is caused by neuronal dysfunction (Liang et al., 2014), fibroblasts may provide an experimental model for investigating the molecular and cellular mechanisms underlying torsinA-dependent cell polarity. Ultimately, a better understanding of these mechanisms will guide the rational design of potential therapeutics that may be used to combat DYT1 dystonia pathogenesis.

MATERIALS AND METHODS

Antibodies. β-catenin mouse mAb and rabbit polyclonal antibody were purchased from Zymed (San Francisco, CA). GAPDH mouse mAb was from

Sigma-Aldrich. TorsinA rabbit polyclonal antibody was from Abcam. EGFP mouse mAb and dsRed rabbit polyclonal antibody were purchased from Sigma-Aldrich and Clontech (Mountain View, CA), respectively. Lamin A/C (MANLAC1) mouse mAb was a kind gift from G.E. Morris (The Wolfson Centre for Inherited Neuromuscular Disease, Shropshire, UK). LAP1 and LULL1 rabbit polyclonal antibody were previously described (Goodchild and Dauer, 2005). Pericentrin mouse mAb and rabbit polyclonal antibody were purchased from Covance (Princeton, NJ) or BD Biosciences (San Jose, CA). The N2G rabbit polyclonal antibody was previously described (Luxton et al., 2010) as was the nesprin-3 rabbit polyclonal antibody (Morgan et al., 2011), which was a kind gift from D. Starr (University of California, Davis, CA). Tyrosinated α-tubulin rat monoclonal antibody (mAb) (YL1/2) was collected in house from supernatant generated by hybridomas purchased from the European Collection of Animal Cell Cultures (Salisbury, UK). SUN1 and SUN2 Rabbit polyclonal antibodies were purchased from Abcam (Cambridge, MA). Vinculin mouse mAb was from Sigma-Aldrich. Secondary antibodies were from two different sources. From Jackson ImmunoResearch Laboratories (West Grove, PA), we purchased goat anti-mouse secondary antibodies conjugated to AlexaFluor 488 or 650 as well as rhodamine. We purchased goat anti-rat and anti-rabbit secondary antibodies conjugated to Dylight 488, 561, or 649 from Thermo Fischer Scientific (Waltham, MA).

Cell culture and monolayer wounding. NIH3T3 fibroblasts were cultured in DMEM with 10% bovine calf serum purchased from Thermo Fischer Scientific; serum starved for 2 days, wounded and stimulated with 10 µM LPA as previously described (Gomes et al., 2005; Palazzo et al., 2001). MEFs were grown in DMEM with 15% bovine calf serum, serum starved for 3 days, wounded and stimulated with 10 µM LPA.

DNA constructs. The Lifeact-mCherry plasmid was a kind gift from R. Wedlich-Soldner (Max Planck Institute of Biochemistry, Martinsried, Germany) (Riedl et al., 2008). The previously described EGFP-N3α and -N3β constructs (Wilhelmsen et al., 2005) were kind gifts from A. Sonnenberg (Netherlands Cancer Institute, Amsterdam, Netherlands). We have previously described the SS-EGFP-TA^{WT}, -TA^{K108A}, -TA^{E171Q}, -TA$^{\Delta E302/303}$, TB^{WT}, TB^{E178Q}, T2^{WT}, T2^{E162Q}, T3^{WT}, T3^{E236Q}, and -mini-N2G constructs (Goodchild and Dauer, 2004; Kim et al., 2010; Luxton et al., 2010).

The following constructs were generated during the course of this investigation using the primers described in Table S1. All constructs were confirmed by sequencing performed at the University of Minnesota Genomics Center (Minneapolis, MN). The following mutations were introduced into SS-EGFP-TA^{WT}: C280S, C319S, and C280,319S using QuikChange (Agilent Technologies) as directed by manufacturer. SS-EGFP-TA^{C280S} was created using the TA^{C280S}-F and TA^{C280S}-R primer pair, while the primer pair TA^{C319S}-F and

TA^{C319S}-R was used to create SS-EGFP-TA^{C319S}. SS-EGFP-TA^{C280,319S} was generated using the TA^{C319S}-F and TA^{C319S}-R primer pair to mutagenize SS-EGFP-TA^{C280S}. To make the EGFP-LAP1^{WT} construct, we used PCR to amplify EGFP from pEGFP-N1 using the primers EGFP-LAP1^{WT}-F and EGFP-LAP1^{WT}-R, both of which contain *Kpn*I cut sites. The resulting PCR product was then purified and digested along side the previously described myc-LAP1 construct (Goodchild and Dauer, 2005) with RE1 and RE2. The digested PCR product and plasmid were then purified and ligated to make EGFP-LAP1^{WT}. EGFP-LAP1^{R442A} was created via Kinase, Ligase, *Dpn*I (KLD) treatment where 2µL of PCR product amplified using the primer pair EGFP-LAP1^{R442A}-F EGFP-LAP1^{R442A}-R was treated with T4 ligase, T4 PNK, and DpnI in T4 ligase buffer in a 20µL reaction for 20 minutes at room temperature.

The chimeric EGFP-LAP1^{ND-TMD}-LULL1^{LD} and EGFP-LULL1^{CD-TMD}-LAP1^{LD} constructs were generated as follows. The first step towards creating EGFP-LAP1^{ND-TMD}-LULL1^{LD} was to amplify by PCR the ND through the transmembrane domain of LAP1 using the primer pair LAP1^{ND-TMD}-F and LAP1^{ND-TMD}-R. After purification, the PCR product was used in combination with the LAP1^{LD}-R primer to amplify by PCR the LULL1^{LD} from a previously described myc-LULL1 construct (Goodchild and Dauer, 2005). The resulting PCR product was then purified, digested with *Hind*III and *Bam*HI, and cloned into pEGFP-C1, which was digested with the same restriction enzymes. A similar protocol was followed to generate EGFP-LULL1^{CD-TMD}-LAP1^{LD}. However, the first PCR product was

produced using the primer pair LULL1CD-TMD-F and LULL1CD-TMD-R and myc-LULL1 as a template. The second PCR product was then generated using the first PCR product and $LAP1^{LD}$-R as primers and myc-LAP1 as a template. After purification, the second PCR product was digested with *Hind*III and *Bam*HI, and cloned into pEGFP-C1, which was digested with the same restriction enzymes.

DNA microinjections. Plasmid DNA was purified using Plasmid Midi Kit (Qiagen, Valencia, California) and was microinjected into nuclei at concentrations between 5-30 μg/ml as previously described (Gomes et al., 2005). Injections were performed on a Nikon (Melville, New York) TS100 microscope equipped with a CFI Achro LWD ADL 20X/NA0.4 WD 3.0mm objective and a Nikon Narishige NT-88 Manipulator set.

Fixed cell fluorescence imaging. All fixed cell imaging was performed on a Nikon Eclipse NI-E microscope driven by NIS-Elements software using an oil immersion 40X/1.30 NA Plan Fluor WD 0.20 MM Eco-Glass oil immersion objective lens, a Lumencor (Beaverton, ON) SOLA Solid State White-Light Excitation SubSystem, and a Photometrics (Tucson, AZ) Coolsnap ES2 12 Bit 20 MHz Digital Monochrome CCD Camera. A custom DAPI filter for the SOLA light source was used, which consisted of an ET395/25x excitation filter and an ET460/50m emission filter purchased from Chroma (Bellows Falls, VT). Nikon

EGFP (C-FL EGFP Hard Coat High Signal to Noise Zero Shift), Texas Red (C-FL Texas Red HC HISN Zero Shift), and Cy5 (C-FL CY5 Hard Coat High Signal to Noise Zero Shift) filter sets were also used.

FRAP. FRAP was performed with a Zeiss LSM 510 META scanning confocal microscope equipped with a 30 mW argon 488 nm laser and a Zeiss 40X/1.3 NA Plan-Apochromat objective as previously described (Östlund et al., 2009). Briefly, a region of interest was selected and photobleached for 25 iterations at 100% laser power, after which recovery of fluorescence was monitored with 2 second intervals at 5% laser power. ImageJ (http://rsb.info.nih.gov/ij/) was then used to quantify the average intensity of the fluorescence within the region of interest, which was normalized relative to the change in total fluorescence $I_{rel} = T_0 I_t / T_t I_0$ where T_0 is the total cellular intensity during the pre-bleach, T_t is the total cellular intensity at time point t, I_0 is the average intensity in the bleached area during pre-bleach, and I_t is the average intensity in the region of interest at time point t. The normalized fluorescence was then plotted against time after bleaching.

As the immobile fraction (the difference between the fluorescence intensity in the bleached area pre-bleach and the intensity at ∞ after bleach) differed between the different EGFP-tagged constructs, we used a modified $t_{1/2}$ value, where $t_{1/2}$ is the time after bleach required for the fluorescence levels to reach the median between levels immediately after bleach and pre-bleach, rather than using the median between pre-bleach levels and steady-state levels. To

determine $t_{1/2}$, a modification of the method described by Harrington et al. (Harrington et al., 2002) was employed. We plotted ln(1-i_t) vs. time after bleach, where it is the average normalized fluorescence intensity in the bleach-region at time t and 1 is the average normalized fluorescence intensity in the bleach-region pre-bleach. The curves were fitted using KaleidaGraph (http://www.synergy.com) and $t_{1/2}$ calculated as $t_{1/2}$ □ ln2 X (–1/slope). Data from the first 31 seconds after bleach were used in all experiments. The $t_{1/2}$ of recovery was calculated from ≥3 independent experiments.

Immunofluorescence. Cells grown on No. 1.5 coverslips were fixed in either −20°C methanol or room temperature 4% paraformaldehyde as previously described (Gomes et al., 2005; Palazzo et al., 2001). Coverslips were mounted on slides using Fluoromount purchased from Thermo Fisher.

Live cell DIC and fluorescence imaging. NIH3T3 fibroblasts or MEFs were grown on 35 mm dishes with #1.5 glass coverslip (0.16-0.19 mm) bottoms purchased from In vitro Scientific (Sunnydale, CA). Confluent monolayers were serum starved and wounded as described in “Cell culture and monolayer wounding**”** above. Cells were then washed twice with live imaging media ((GIBCO® HBSS purchased from ThermoFisher Scientific) containing essential and nonessential MEM amino acids purchased from Invitrogen), 2.5 g/L glucose, 2 mM glutamine, 1 mM sodium pyruvate, 20 mM HEPES (pH 7.4)), and

transferred to the 37° C Okolab USA Inc. (Burlingame, CA) full enclosure incubator with temperature control attached to a Marianas 200 Microscopy Workstation (Intelligent Imaging Innovations (3I), Denver, CO) built on a Zeiss (Jena, Germany) AxioObserver Z.1 stand and driven by SlideBook 6.0 (3I), Denver, CO). After selecting the regions of the coverslip to be imaged, the cells were stimulated with 20 μM LPA. DIC images were captured with a Photometrics CoolSnap HQ2 CCD camera. Fluorescence confocal imaging was performed with a 5000 rpm Yokogawa (Tokyo, Japan) CSU-X1 M1 Spinning Disk Confocal head and a Photometrics Evolve EMCCD camera. A 3I LaserStack laser launch containing two 50 mW solid state lasers (488 nm and 561 nm) was used as a light source for the live cell fluorescence imaging. A Yokogawa CSUX dichroic containing Semrock (Rochester, NY) filters for 405/488/561/640 excitation with quad emitter and individual emitters was used as the filter set. All live cell imaging was performed using a Zeiss Plan-Apochromat 63x/1.4NA oil objective containing DIC III prisms.

Quantification of dorsal perinuclear actin cables. LPA- and serum-stimulated wound-edge NIH3T3 fibroblasts that had been stained for F-actin and nuclei were used to assess the effect of siRNA-mediated torsinA- and LAP1-depletion on dorsal perinuclear actin cables. Dorsal actin cables above the nucleus were manually counted from single-plane images taken of F-actin and nuclei counting only those actin cables that passed over the nucleus.

Quantification of nuclear envelope protein levels. Eleven z-section epifluorescence images of LPA-stimulated wound-edge fibroblasts stained for DNA, microtubules, and a nuclear envelope protein were obtained with a 300 nm step size. After acquiring the images, the ‘select best planes’ function from Nikon NIS-Elements software was used to select a single z-section from each imaged area of cells using the microtubule channel as the guide for selecting the in-focus section. The selected images were then exported as 16-bit greyscale tiff files and imported into custom-made MATLAB software from MathWorks (Natick, MA) for analysis. This software applies a mask to the DAPI-stained DNA channel using the ‘canny edge detection’ algorithm. The user then identifies the nuclei on the wound-edge to be analyzed and the program integrates the intensity of the nuclear envelope protein channel within the DAPI mask and then divides that intensity by the area of the mask.

Quantification of rearward nuclear movement. Multipage tiffs were obtained for each cell imaged using DIC microscopy, with a single z-section (or maximum intensity projection), and time along the third axis of each image. Tiffs were then imported into custom MATLAB software for quantifying nuclear movement. Using this software, the user defines the wound-edge, and then manually traces an outline of the nucleus in the cell of interest at each time step. Next, the ‘region props’ function is used, which calculates the centroid, area, eccentricity, and

absolute angle of the major axis of the traced object. Using Microsoft Excel (Redmond, WA), the coordinates of our wound clicks are then rotated so that each cell analyzed is parallel to the x-axis providing a similar point of reference for each nucleus. Once rotated, the change in nuclear centroid position over time are used to determine overall speed (displacement) during the two-hr time course. Nuclei that move ≥ 10% of the cell radius towards the cell rear are defined as rearward moving nuclei. Experiments are repeated at least twice.

Quantification of nucleus and centrosome position. Fluorescence images of cells stained for centrosomes (anti-pericentrin), cell-cell contacts (anti-β-catenin), DNA (DAPI), expression tag, and microtubules (anti-Tyr-α-tubulin) were acquired as previously described (Gomes et al., 2005; Palazzo et al., 2001). Centrosome orientation was determined as previously described (Palazzo et al., 2001) and experiments were repeated ≤ thrice. Analysis of nucleus and centrosome position was performed as previously described (Gomes et al., 2005). Briefly, images were pseudocolored, combined and aligned such that the wound-edge was parallel to the x-axis using Metamorph software purchased from Molecular Devices (Sunnyvale, CA). Cell perimeters were drawn over the cell-cell contacts (β-catenin) and the wound-edge (Tyr-tubulin or injection-markers). From this information, the cell centroid and equivalent radius was calculated using the 'integrated morphometry analysis' program in Metamorph. The Metamorph 'measure pixel' function was used to identify the position of the centrosome

(pericentrin) and the approximate centroid of the nucleus. A vector representing the distances from the nuclear centroid and the centrosome to the cell centroid was drawn and resolved into x and y coordinates (parallel and perpendicular to the leading edge, respectively). Measurements were normalized to cell size to allow for comparison between cells. Only the y-coordinate was used in plots as the x-coordinate (position of the nuclear centroid or centrosome along the x-axis) did not change significantly. The difference between the cell centroid and the nucleus centroid or centrosome was then divided by the radius to determine the percentage of the cell radius either organelle traveled.

Quantification of retrograde actin flow. Serum-starved, wound-edge NIH3T3 fibroblasts treated with either non-coding or torsinA-targeting siRNAs were microinjected with the Lifeact-mCherry construct (20 ng/µL) and incubated for 1.5-2.0 h at 37°C to allow for expression. Cells were then washed with recording media and moved to the heated stage of our Marianas 200 Microscopy Workstation described above in “Live cell DIC and fluorescence imaging”. Both Lifeact-mCherry expression and nuclear position (DIC) were imaged every 5 minutes for 2.0 h shortly after the addition of 20 µM LPA to allow tracking of both nuclear movement and F-actin. The resulting images were then rotated so that each wound-edge was parallel to the x-axis to keep the point of reference similar between cells. Nuclear tracking using the DIC channel was completed as described above in “Quantification of rearward nuclear movement”. To track F-

actin over the nucleus, we isolated a single plane on the dorsal side of the nucleus and tracked the y-position of the center of individual actin cables between 35-90 minutes post-LPA stimulation. To track F-actin in the cytoplasm, we created maximum intensity projections of the cells and identified a region of the cell that was about 2 microns directly rearward from the center of the wound-edge where we tracked individual cables between 35-90 minutes post-LPA stimulation. Experiments were repeated 3 times.

Quantification of TAN line localization. After acquisition as described above in "Fixed cell fluorescence imaging", epifluorescence images were opened in FIJI. A maximum intensity projection of the image planes containing the top half of the nuclear envelope for each channel was created. Using mCherry-mN2G lines as a guide, the image was rotated without interpolation so that the TAN line was parallel to the X-axis. The rotation was then propagated to the torsinA channel. An 11-pixel tall box was then drawn to cover the length of the TAN line, with the central pixel centered on the TAN line. The mean intensity for each row of pixels was then calculated for each channel and then each mean intensity was expressed as a percentage of the sum intensity of the whole measured region. The regions were then mirrored by taking the mean of the first and the eleventh, second and tenth, etc, pixel. This process was repeated for all TAN lines. Fractional fluorescence of each pixel row was then calculated, and mean and

SEM was plotted as a function of distance from the center of the TAN lines. N≥35 cells for each construct.

Quantification of TAN line persistence. Serum-starved, wound-edge NIH3T3 fibroblasts treated with either non-coding or torsinA-targeting siRNAs were microinjected with the EGFP-mini-N2G construct (5.5 ng/µL) and incubated for 45 min at 37°C to allow for expression. Cells were then washed with live-imaging media and moved to the heated stage of our Marianas 200 Microscopy Workstation described above in “Live cell DIC and fluorescence imaging”. 19 z-section confocal stacks with a 0.4 µm step size were collected of expressing cells every 5 minutes for 2 h using a 63x/1.4NA Plan-Apochromat DIC objective following stimulation with 20 µM LPA. After the acquisition time course was completed, movies were inspected in 3-dimensional time-lapse view within SlideBook 6.0 in order to monitor the EGFP-mn2G signal on the dorsal nuclear surface. A Maximum intensity projection of the dorsal half of the nucleus was then generated using SlideBook 6.0 for the time course, in which TAN line persistence was analyzed by tracking individual TAN lines (linear EGFP-mini-N2G signals ≥ 2 µm in length) over time using ImageJ. Experiments were repeated three times.

Quantification of total protein levels by western blot. Whole cell lysates samples were prepared by lysing cells with non-reducing sample buffer. Protein

concentration was determined and 15µg protein was loaded onto Novex protein gels (Life Technologies). Samples were subjected to SDS-PAGE and then transferred to nitrocellulose and probed with the indicated antibodies. Blots were imaged and bands quantified using Odyssey imaging system and Image Studio software from LI-COR (Lincoln, Nebraska). All experiments were repeated three times.

Reagents. F-actin was stained with rhodamine-phalloidin, which was purchased from Cytoskeleton, Inc. (Denver, CO). DAPI was purchased from Life Technologies (Carlsbad, CA). LPA was purchased from Avanti Polar Lipids, Inc. (Alabaster, AL). Restriction enzymes were either purchased from New England Biolabs (NEB) (Ipswich, MA) or Promega (Madison, WI). The QuikChange Kit was purchased from Agilent Technologies (Santa Clara, CA). Phusion DNA polymerase, T4 DNA ligase, and T4 PolyNucleotide Kinase (PNK) were also purchased from NEB. All other chemicals were from Sigma-Aldrich (St. Louis, MI) unless otherwise specified. GFP mouse monoclonal antibodies were from Sigma-Aldrich (Cambridge, MA). IRDye® 650 nm-conjugated goat anti-mouse secondary antibodies were from LI-COR (Lincoln, NE). Wizard SV Gel and PCR Clean-Up System was from Promega. GeneJet Plasmid Midiprep Kit was from ThermoFisher Scientific (Waltham, MA). All other chemicals were purchased from Sigma-Aldrich (St. Louis, MO) unless otherwise specified.

RNAi. All RNAi experiments were performed using 50nM siRNA duplexes purchased from Shanghai GenePharma (Shanghai, China), which were transfected using Lipofectamine RNAiMAX purchased from Life Technologies according to the manufacturer. To identify functional siRNA duplexes, four sequences were selected using the artificial neural network BIOPREDsi (Huesken et al., 2005). The duplexes used in this study were the most effective at depleting the target protein based on western blot or RT-PCR analysis. The sequences of the duplexes used are described in Table S2. The GAPDH and N2G siRNA sequences were previously described (Luxton et al., 2010).

Statistics. Two-tailed *t*-tests were used to calculate *P* values (*$P < 0.05$, **$P < 0.01$; ***$P < 0.001$; ****$P < 0.0001$) throughout the manuscript. The error bars presented in bar graphs throughout the manuscript report the standard error of the mean.

Chapter 4

A torsin homolog in *Dictyostelium* is modulates developmental processes

Introduction:

Torsins are a subfamily of the larger family of ATPases Associated with various cellular Activities (AAA+) proteins family and localize to the shared lumen of the nuclear envelope (NE) and Endoplasmic Reticulum (ER), where they have many important but poorly understood roles (Rose et al., 2015; Saunders and Luxton, 2016). Highlighting the biological importance of torsins is the fact that their loss is often lethal (Goodchild et al., 2005; Basham and Rose, 2001). Additionally, a single amino acid deletion in human torsin1A is associated with the early-onset neurological movement disorder, DYT1 dystonia (Ozelius et al., 1997).

Within the ER, torsins have been shown to be involved in protein quality control and organization of the smooth ER (Nery et al., 2011; Rose et al., 2014). Many studies show that torsins also accumulated and function within the NE, which is a subdomain of the ER (Rose et al., 2015). Within the NE, torsins regulate NE egress of herpes viruses, spacing of the inner and outer nuclear membranes (INM and ONM, respectively), nuclear pore complex localization, and as well as displacement of resident NE proteins (Maric et al., 2011; Goodchild and Dauer, 2004; VanGompel et al., 2015; Vander Heyden et al., 2009).

AAA+ proteins typically assemble into hexameric rings and use the energy released during ATP hydrolysis to structurally remodel substrates (Hanson and

Whiteheart, 2005). Torsins have many hallmarks of AAA+ proteins, including but not limited to, ATP binding and hydrolysis as well as assembly into hexameric rings (Jungwirth et al., 2011; Sosa et al., 2014; Vander Heyden et al., 2009). However, torsins are atypical AAA+ proteins, in that they lack several canonical features of AAA+ proteins. Unlike most other AAA+ proteins, torsins to lack an N-terminal adaptor binding domain, which are typically critical for substrate recognition (Román-Hernández et al., 2011). Many torsins have a non-canonical Walker-A motif, which is responsible for ATP-binding (Wendler et al., 2012). The canonical Walker-A motif is GxxxxGK[T/S] (where x represents any amino acid), while torsins have a GxxxxGKN, with the threonine or serine residue at the end of the motif being replaced with an asparagine, which reduces the ATP hydrolysis rate in other AAA+ proteins (Nagy et al., 2009). Finally, torsins lack an arginine finger motif, which is critical for ATP hydrolysis (Hanson and Whiteheart, 2005).

Unique to AAA+ proteins, torsin1A ATPase activity is stimulated by another resident protein of the NE, Lamina Associated Polypeptide1 (LAP1). LAP1 localizes to the INM and its C-terminal domain extends into the lumen of the NE, allowing for interaction with torsinA. In mammals, there is another protein that shares 60% identity with the luminal domain of LAP1, called Luminal like Lap1, (LULL1), which resides in the ER (Goodchild and Dauer, 2005). The luminal

domain of LAP1 and LULL1 contain highly conserved arginine residues that stimulate torsinA ATPase activity (Zhao et al., 2013; Brown et al., 2014).

Currently, it is thought that torsinA and LAP1 homologs are only found in obligate multicellular animals (Rose et al., 2015). Given the several important cellular and developmental roles have been attributed to torsins, a phylogenetic analysis would help uncover a common ancestor and anciently conserved functions.

Results:

To see if we could identify torsin homologs outside of metazoans, we collected torsin sequences by using Basic Local Alignment Search Tools (BLAST) on the genomes that have been sequenced and are available online. Human torsin1A protein sequence (NCBI Reference Sequence: NP_000104.1) was used as a query sequence for the BLAST function at numerous databases.

Sequences that returned as likely to be torsin homologs were run through Simple Modular Architecture Research Tool (SMART) from European Molecular Biology Laboratories (EMBL), as well as a second signal sequence prediction tool, SignalP 4.1 (Petersen et al., 2011; Letunic et al., 2015). A potential homolog was considered for subsequent analysis if it contained a AAA+ domain and had either a transmembrane domain or signal sequence which would result in the AAA+ domain of the protein localizing in the lumen of the NE and ER. After compiling prospective sequences, the list was culled to even out the large number of

mammalian genomes that have been sequenced compared to other non-mammalian organisms.

Sequences were then assembled and entered into Practical Alignments using SATe and TrAnsitivity (PASTA) (Mirarab et al., 2014). PASTA is a pipeline that allows for alignment and comparison of multiple sequences. As ClpB is torsinA's closest relative, the D2 AAA domain of evolutionarily divergent ClpBs were used as an outgroup during the analysis (Figure 31).

We found that in mammals, there is a torsin4A, which has been largely overlooked in the torsin literature, only recently mentioned an article published at the time we started our analysis (Rauniyar et al., 2015). Torsin4a is different from the other mammalian torsins in that it does not have a N-terminal signal sequence, but instead has a transmembrane domain, although the AAA+ domain is predicted to still be within the lumen of the ER (Rose et al., 2015).

Torsin sequences in invertebrates tended to have KDEL-like sequences (i.e. HDEL, DDEL) (Capitani and Sallese, 2009; Pagny et al., 1999; Alanen et al., 2011), suggesting a more canonical mechanism for ER retention in that lineage compared to the NTD mediated retention for mammalian torsinA (Vander Heyden et al., 2011). Additionally, the conserved RSS of torsinA (GCK amino acid motif) is highly conserved in obligate multicellular organisms which also have a LAP1 homolog, but is not found in the organisms representing Archaeplastida,

Ameobozoa, or Excavata lineages, where LAP1 homologs have not been found (Zhu et al., 2010; Rose et al., 2015). The torsin homologs from these organisms

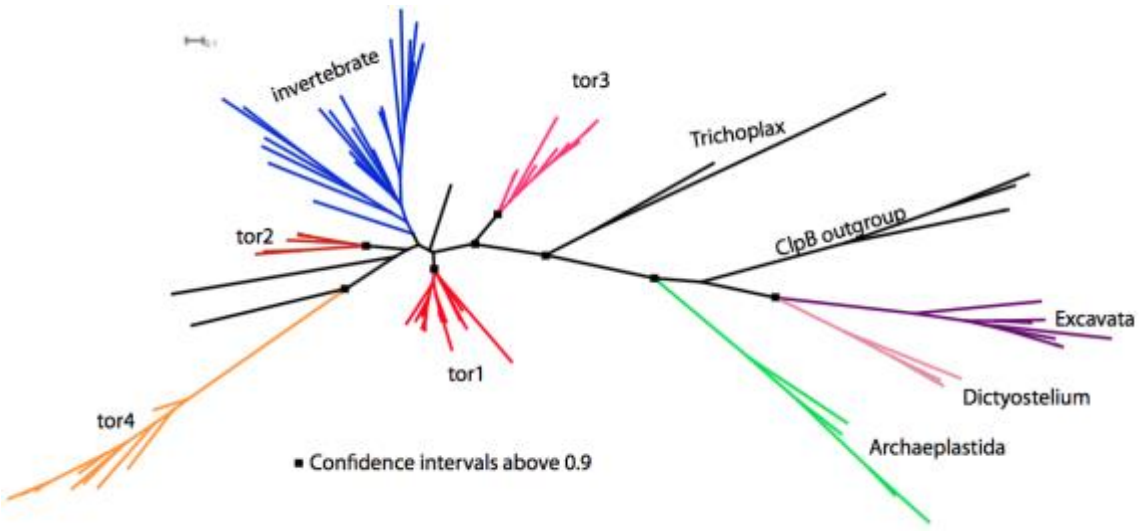

Figure 31: Phylogenetic analysis of torsins. Phylogenetic tree showing the relationship between the torsins analyzed. Black boxes represent confidence intervals above 0.9, as determined by PASTA (Mirarab et al., 2014), the scale is determined by FastTree (Price et al., 2010).

also have canonical Walker-A motifs (GxxGxGK[S/T], unlike the metazoan torsin, which contains a non-canonical Walker-A [GxxGxGKN].

We decided to focus our efforts on the torsin homolog in *Dictyostelium discoideum* for several reasons. First, it is a novel torsin relative found outside of metazoans. Second, *Dictyostelium* are well studied model organism with a plethora of molecular tools available, including a fully sequenced genome. Third, *Dictyostelium* are free living, and therefore easy to image live. Fourth, *Dictyostelium* control the position of their nucleus during directional cell migration and have conserved LINC complex components as well as nuclear lamins (Devos et al., 2014). Fifth, we were interested in the role of torsin homologs during directional cell migration, which is an important aspect of the Dicty development (Fey et al., 2007).

Characterization of tsin, a novel torsin homolog in *Dictyostelium discoideum*

Using human torsinA as query sequence for BLASTP at DictyBase (DIctyBase.org), two putative torsin related proteins were returned, DDB_G0268156 and DDB_G0289047 (SMART). DDB_G0268156 has a predicted signal sequence and one AAA domain. DDB_G0289047 did not have a predicted signal sequence, has two AAA domains, and a ClpB small domain (Figure 32).

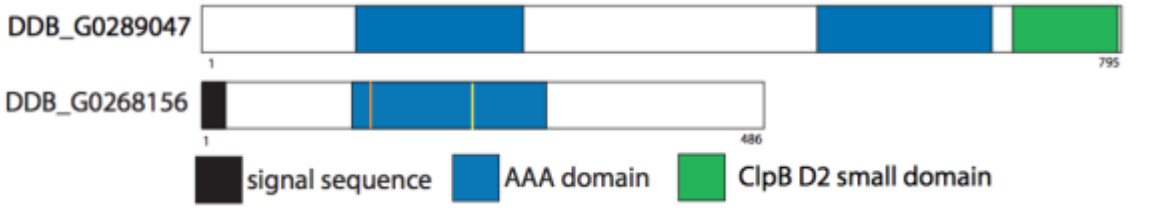

Figure 32: Comparison of the two genes returned after using human torsinA protein sequence as query for BLAST at Dictybase. DDB_G0289047 contains two AAA+ domains and a ClpB D2 small domain, while DDB_G0268156 has an N-terminal signal sequence and one AAA+ domain. Similar analysis was done on all potential torsins returned from databases.

Based on this analysis, we decided that DDB_G0268156 was likely to be a torsin homolog, while DDB_G289047 was the *Dictyostelium* ClpB homolog. Thus, it was named tsin, for **T**or**SIN** (http://dictybase.org/gene/DDB_G0268156). The *Dictyostelium* torsin homolog lacks a hydrophobic N-terminal domain, as well as lacking a KDEL-like sequence. However, luminal *Dictyostelium* proteins can have non-canonical ER retention mechanisms (Monnat et al., 2000).

Molecular modeling of tsin

To better understand the relationship between *tsin* and mammalian torsins, we utilized the structural prediction software Phyre2 (Kelly et al., 2015). The Clp family of AAA+ proteins are closely related to the torsin family. As such, the nucleotide binding domain 2 (NBD2) of the *Thermus thermophlius* ClpB protein was used as a reference for the modeled tsin molecule. Chimera was used to overlay the model onto the NBD2 of ClpB (Figure 33) (Pettersen et al., 2004; Zeymer et al., 2014). Much like the homology of torsinA with human ClpA small domain (Zhao et al., 2013), Chimera overlaid tsin on the small domain of ClpB (Figure 33b). In addition to the 3-dimensional model, Phyre2 also predicts alpha helix and beta sheet folds in proteins. Arginine fingers are found in the second region of homology at the end of alpha helix 4 of the AAA domain (Hanson and Whiteheart, 2005). As an additional level of confirmation, HHpred was used to align tsin with the nucleotide binding domain2 of *T. thermophilus* ClpB (Soding, 2005; Zeymer et al., 2014). The arginine at residue 342 at the end of the fourth

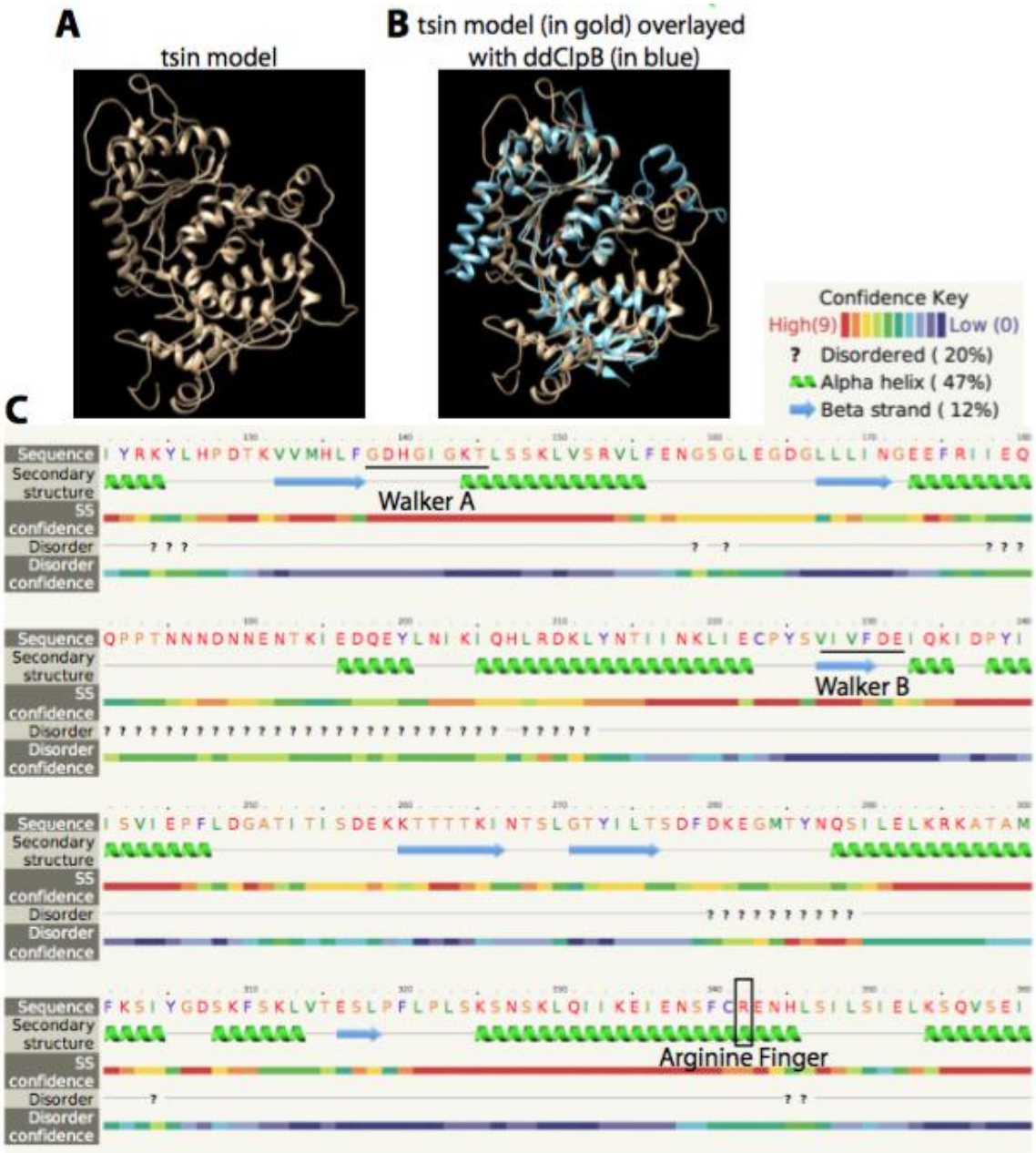

Figure 33: Molecular modeling of tsin.

FIGURE 33: Molecular modeling of tsin. **A)** tsin modeled using Phyre2 **B)** tsin overlaid on the *T. thermophilus* NBD2 ClpB (PDB: 4lj4) using the MatchMaker function in Chimera . Tsin is in gold and ClpB is in light blue. **C)** Secondary structure prediction of tsin shows that it has a canonical walker-A motif and an arginine finger.

alpha helix in tsin was aligned with the arginine finger of the D2 domain of ClpB (R747), which is the same residue that the LAP1 arginine finger aligns with, suggesting that tsin contains a canonical arginine finger (Brown et al., 2014).

Generation of *tsin* knock-out in *Dictyostelium discoideum*.

To test the role of *tsin* during development, we introduced a blasticidin resistance cassette into the *tsin* gene to disrupt function (De Lozanne and Spudich, 1987). Genomic DNA was isolated from the colonies, and PCR was performed using primer pairs that span the *tsin* allele to screen our colonies for insertion, and to show that the insertion did not cause chromosomal breaks (Figure 34). Of the ten colonies selected, three showed clean insertion of the BLAST resistance cassette into the *tsin* locus.

Preliminary experiments of growth on bacterial lawns showed no differences in growth rates between the three knock-out lines and Ax2 controls. Of the three lines with correct insertion, colony 8 was chosen to continue with experimentally.

EGFP tagged tsin localizes to the NE and ER.

If an identified gene is a torsin homolog, it should localize to the lumen of ER and NE. Therefore, we tagged *tsin* with EGFP to observe its sub-cellular localization

in cells (Figure 5). To do so, we first transformed cells expressing H2B mCherry (Corrigan and Chubb, 2014) with either ss-EGFP-tsin or the luminal marker GFP-

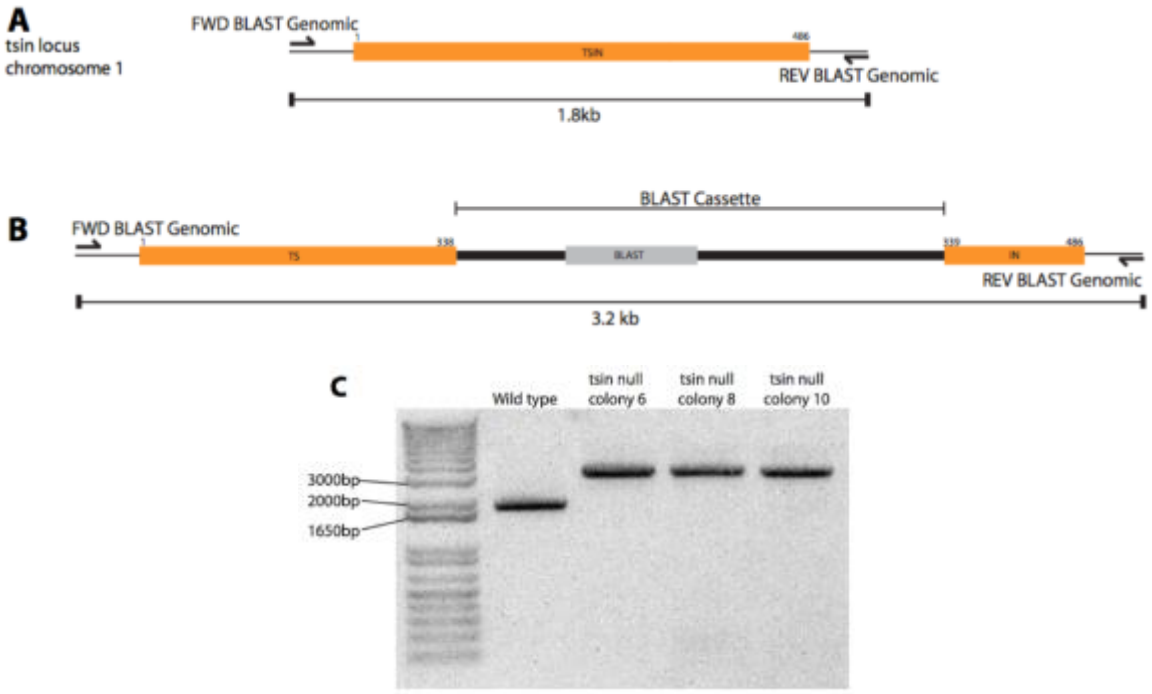

Figure 34: PCR verification of blasticidin cassette insertion into the tsin gene. A) Diagram of the tsin locus. Amino acids are listed on top as reference. B) Diagram of the tsin locus with the BLAST cassette inserted. C) PCR results insertion of the blasticidin cassette in three of the colonies.

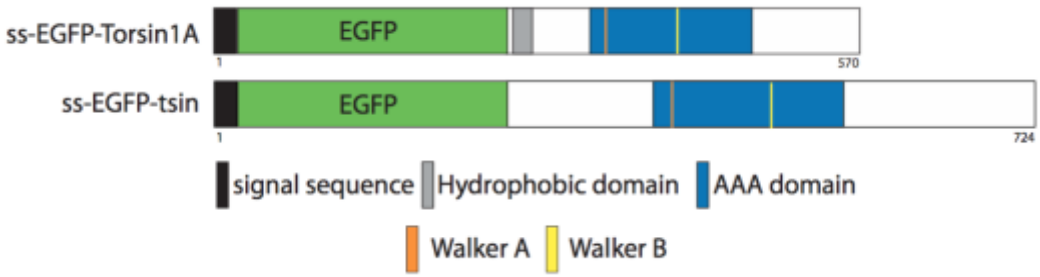

Figure 35: EGFP tagged tsin. Comparison of position of EGFP tag between human torsin and tsin. The EGFP was inserted between the signal sequence and the AAA+ domain.

calnexin (Müller-Taubenberger et al., 2001). Both constructs localized the nucleus and out to the cellular periphery in a manner suggestive of the ER and NE (Figure 36).

To identify the sub-cellular localization of potential substrates of *tsin*, a mutation was made in the Walker-B motif of EGFP-tsin (ss-EGFP-tsin^{E232Q}). Walker-B mutations in other AAA+ proteins inhibit ATP-hydrolysis, but not ATP binding, causing the AAA+ protein to become tightly bound to its substrate (Hanson and Whiteheart, 2005). The *tsin*$^{-}$ cell line was transformed with either ss-EGFP-tsin^{WT} or ss-EGFP-tsin^{E232Q}. Both ss-EGFP-tsin^{WT} and ss-EGFP-tsin^{E232Q} proteins express at the predicted size of 84kDa (Figure 37).

The substrate of *tsin* is found within the NE.

Expression of ss-EGFP-tsin^{WT} is found throughout subcellular structures reminiscent of the NE and ER. Expression of ss-EGFP-tsin^{E323Q} shows enrichment in the NE and the nucleus tends to be eccentric in shape. Some cells expressing ss-EGFP-tsin^{E323Q} appear to have defects the morphology of the NE, as long, finger-like extensions can be seen extending outward (Figure 38).

The role of tsin during *Dictyostelium* Development.

Dictyostelium respond to removal of nutrients by undergoing a developmental

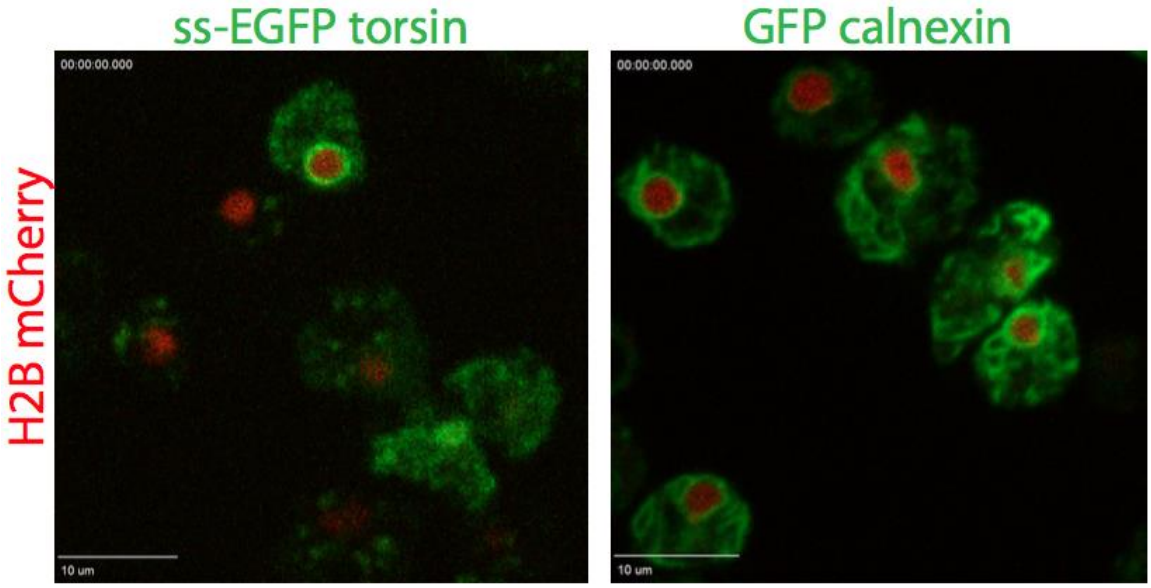

Figure 36: SS-EGFP-tsin localizes to subcellular compartments reminiscent of the NE and ER. Cells stably expressing H2B mcherry to mark the nucleus were transformed with either SS-EGFP-tsin or GFP-Calnexin, a known marker of the NE and ER. Scale bar is 10µm.

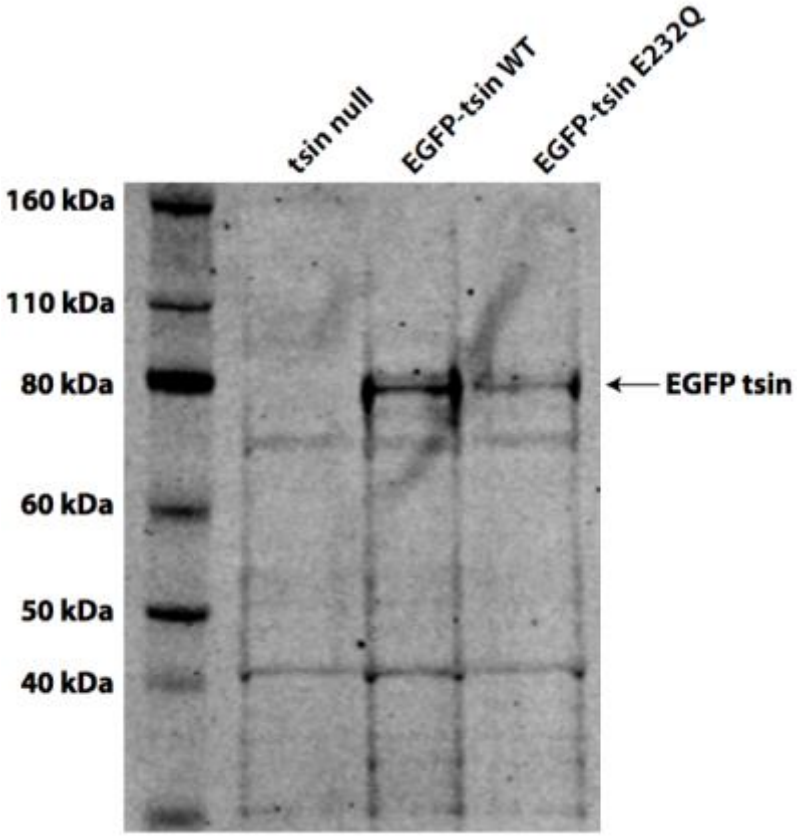

Figure 37: Western Blot of SS-EGFP-tsin constructs. Lysates of tsin null cells transformed with the indicated construct were subjected to SDS-PAGE and probed with an anti-GFP antibody. The predicted molecular weight of the EGFP-tsin chimera is 84kDa.

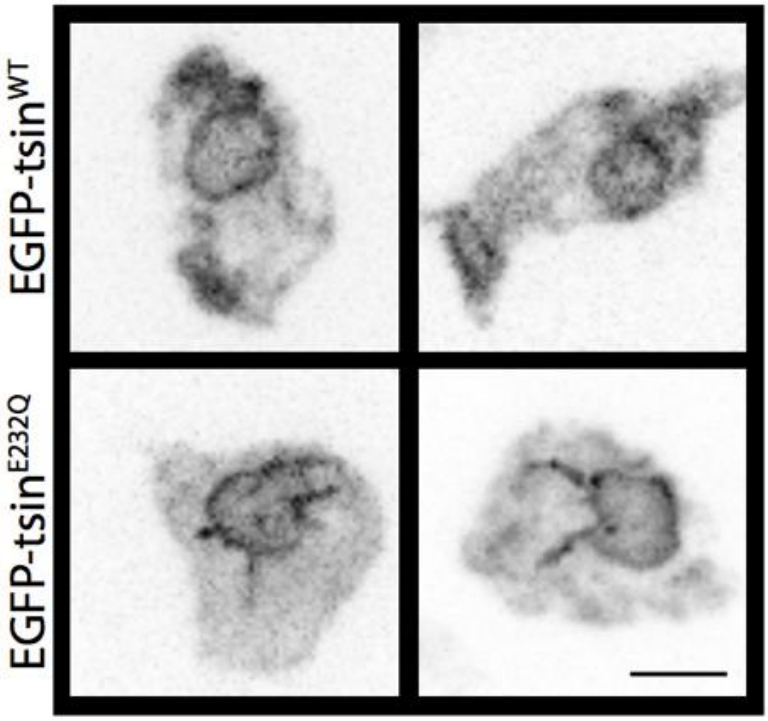

Figure 38: Differential localization and NE morphology of ss-EGFP-tsin^{E323Q}. *Tsin*$^{-}$ cells transformed with either ss-EGFP-tsin^{WT} or ss-EGFP-tsin^{E323Q}. Scale bar is 5µm.

response which is dependent upon a cellular response to cAMP (Kriebel et al., 2003). Cells begin to chemotax towards cAMP, leading to aggregation. After initiation of aggregation, cells will polarize and begin a process called streaming, where migrating cells secrete vesicles containing adenylyl cyclase from their posterior, which converts ATP to cAMP, leaving behind a trail of cAMP for subsequent cells to chemotax towards (Kriebel et al., 2003, 2008). In a head to tail fashion, the cells eventually form long chains, called streams. These characteristic streams begin to develop approximately 6 hours after starvation and lead towards an aggregation center. Once a critical mass of cells has aggregated, they undergo differentiation and pattern formation, resulting a small mound (Loomis, 2015). As development continues, the mound forms a tip, followed by a “first finger, which is a cylindrical structure growing upwards from the mound under the control of the tip. The process eventually culminates in a fruiting body with a sorus full of spores. The whole developmental process, starting at starvation and ending with a mature fruiting body, takes about 24 hours (Figure 39) (Fey et al., 2007).

In this developmental time frame, RNAseq data shows that *tsin* mRNA levels increase 42-fold after induction of starvation, reaching a maximum after 4 hours and remains elevated by at least 20-fold throughout development (DictyBase.org). To determine if *tsin* plays any role throughout development, we characterized the *tsin*$^{-}$ cells in a variety of developmental assays.

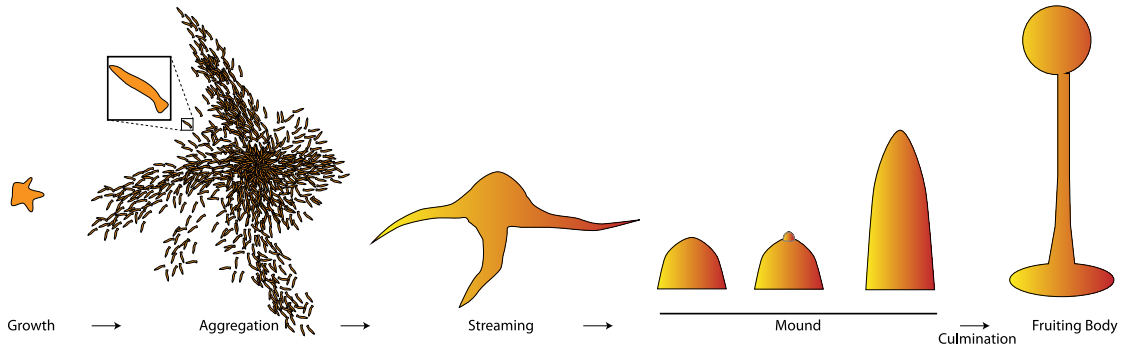

Figure 39: Schematic of *Dictyostelium discoideum* morphogenesis. Developmental progression of *D. discoideum*, starting at the left: A single, vegetative amoeba through aggregation, streaming, mound formation, and eventual culmination that results in a fruiting body topped with a sorus that contains spores ready for dispersal. Aggregation is facilitated by chemotaxis towards cAMP. Once aggregation starts, cells polarize and begin streaming towards an aggregation center, which becomes a multicellular organism, and appears as a small mound. Cells within the mound undergo differentiation and pattern formation. The mound forms a small tip that extends upward, forming a finger, that eventually contracts, and the tip begins to rise to form a fruiting body. Figure not drawn to scale, the persepective of the growth and aggregation stage is top down, the rest are from the side.

***Tsin* is required for streaming and development.**

To determine the role of *tsin* during early development, we first wanted to see if there was a defect in streaming compared to control Ax2 cells. Log phase cells were plated at high density, starved, and imaged every minute for approximately 9 hours.

Wild-type cells formed characteristic aggregation territories and streams that ended in large aggregates (Figure 40). However, the *tsin*$^{-}$ cells did not appreciably form aggregation territories, did not exhibit streaming, and began forming small aggregates before the controls cells had defined aggregation territories. While *tsin*$^{-}$ cells form aggregates, they do so in a streaming independent manner. These smaller *tsin*$^{-}$ aggregates would go through a series of aggregation and dissipation, forming increasingly larger and fewer aggregates, with the developmental process completing at approximately the same time (9hours after starvation) as the wild type controls. However, the final size of the *tsin*$^{-}$ aggregates appears smaller than wild-type controls with an apparent correlative increase in the number of aggregates (Figure 40).

***Tsin* controls developmental timing.**

We next wanted to test whether *tsin*$^{-}$ cells had any defect in later development, as *tsin* mRNA levels remain elevated throughout the process (Dictybase). Dots of

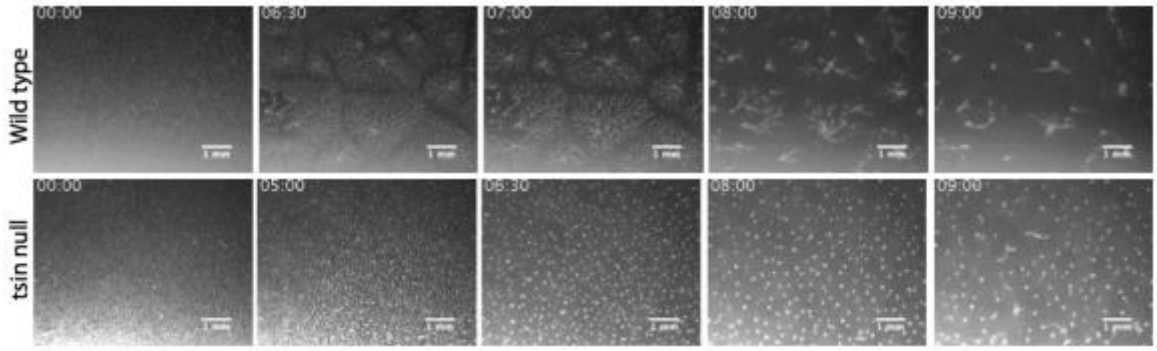

Figure 40: tsin- cells exhibit defective streaming. Control wild-type or *tsin*$^{-}$ cells were plated at high density on plastic dishes, starved, and imaged every minute for 9 hours. WT control cells can be seen making characteristic aggregation territories with streams leading to aggregation centers. *tsin*$^{-}$ cells begin aggregation precociously and have what appear to be much smaller aggregation territories. The small, precocious aggregates often disperse to form larger aggregates repeatedly over the nine-hour time-span. Images shown in each row are captures from a single movie.

liquid culture containing $1e^6$ cells were plated on nutrient poor agar dishes and imaged every minute for up to 43 hours on a dissection microscope (Figure 41).

After 9 hours, mound formation was observed in both wild-type and *tsin*$^-$ cells. Wild-type control cells continued through mound phase in a relatively synchronous manner and formed fruiting bodies on average 20 hours after plating (Figure 41). However, the *tsin*$^-$mounds were delayed in subsequent development. Instead of continuing through development, the *tsin*$^-$ mounds appear to rotate in place for several hours, and then asynchronously continue through development, with first first-finger formation averaging 20 hours after plating, compared to 10 hours for control cells (Figure 41). Additionally, during the pause in mound phase, two adjacent *tsin*$^-$ mounds will merge with each other at a very low frequency (Figure 41, Arrowheads). Additionally, with regular frequency, *tsin*$^-$ cells formed smaller aggregates that frequently spiraled outward, forming donut shaped structures that continued to expand until collapsing back into a small mound, doing so several times throughout development (Figure 41, Arrows), which was rarely seen wild-type cell. The *tsin*$^-$ cells averaged 30 hours after plating until the first fruiting body was formed. Additionally, while both wild-type and *tsin*$^-$ cells formed the same number of mounds, only 60% of the *tsin*$^-$ mounds completed development, compared to virtually all wild-type mounds (Figure 41). The mounds that did not continue through development stayed as

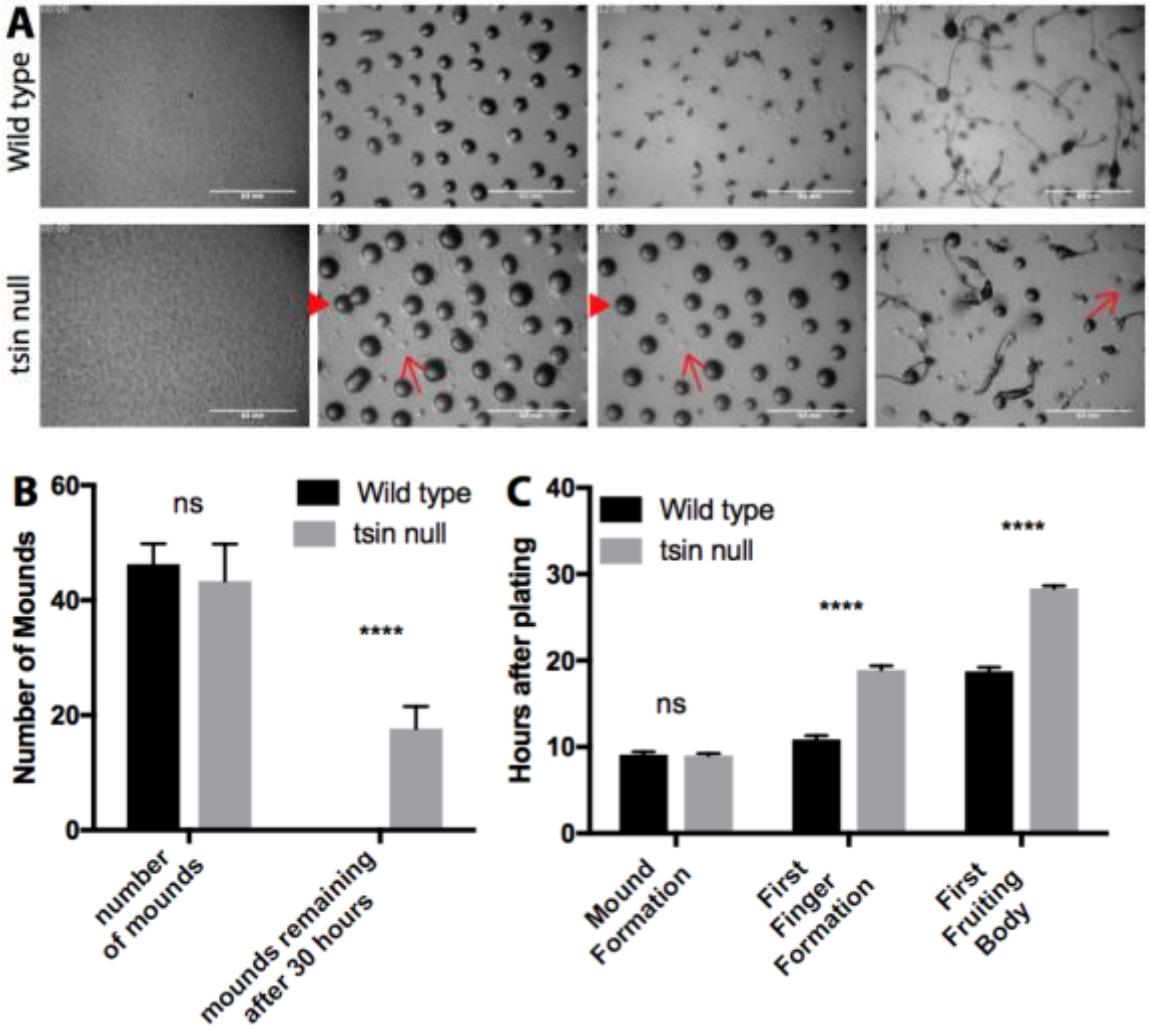

Figure 41: tsin is required for proper developmental timing in a Million Dicty Dot Assay.

FIGURE 41: tsin is required for proper developmental timing in a Million Dicty Dot Assay. A) One million wild type or *tsin*$^{-}$ cells were plated in 20µL HL5 media on nutrient poor phosphate buffered agar plates and imaged every minute for the duration of the experiment. Images shown in each row are captures from a single movie. Both wild-type and *tsin*$^{-}$ cells form mounds around nine hours after plating. Wild-type mounds proceed through development with no delay in mound phase. However, *tsin*$^{-}$ mounds delay in mound phase, and at low frequency two mounds will migrate towards one another and merge (arrowhead). Additionally, *tsin*$^{-}$ cells will form small aggregates that spiral out into large loops before collapsing back into small aggregates, which is rarely seen with WT cells (arrow). **B)** Quantification of mound formation and persistence. **C)** Quantification of developmental timing. **** $p<0.0001$ using two-way ANOVA

mounds for up to one week (data not shown). *Tsin*$^{-}$ fruiting bodies produce spores that can germinate and give rise to viable cells.

***tsin*$^{-}$ cells chemotax faster than wild-type cells.**

The lack of streaming and delayed development exhibited by *tsin*$^{-}$ cells raised the possibility that *tsin*$^{-}$ cells might have defects in chemotaxis. To address this possibility, Ax2 control and *tsin*$^{-}$ cells were pulsed with 150nM cAMP every 6 minutes (Fey et al., 2007) for 5 hours. Cells were then placed in a chemotactic chamber (ibidi, Madison, Wisconsin) with 1µM cAMP on one side and buffer alone on another. We then quantified the direction and speed of movement and found *tsin*$^{-}$ cells had no obvious defect in movement towards cAMP (Figure 42).

We found that *tsin*$^{-}$ cells chemotax almost twice as fast as WT control cells, with WT control cells moving 7µm per minute and *tsin*$^{-}$ cells at 12 µm per minute (Figure 42). In addition to their increased speed during chemotaxis, the *tsin*$^{-}$ cells were less polarized than wild-type cells during chemotaxis (Figure 43).

***Tsin* controls cell-substratum adhesion.**

As exhibited by the precocious aggregation during streaming, we have anecdotally observed that during development, the *tsin*$^{-}$ cells tend to stick to each other and come off the surface of the dish more easily than wild-type cells. This led to the hypothesis that *tsin*$^{-}$ cells may have improper adhesion.

To investigate cell-substrate adhesion, we used Interference Reflection Microscopy (IRM) (Weber et al., 1995). When cells are tightly adhered to a

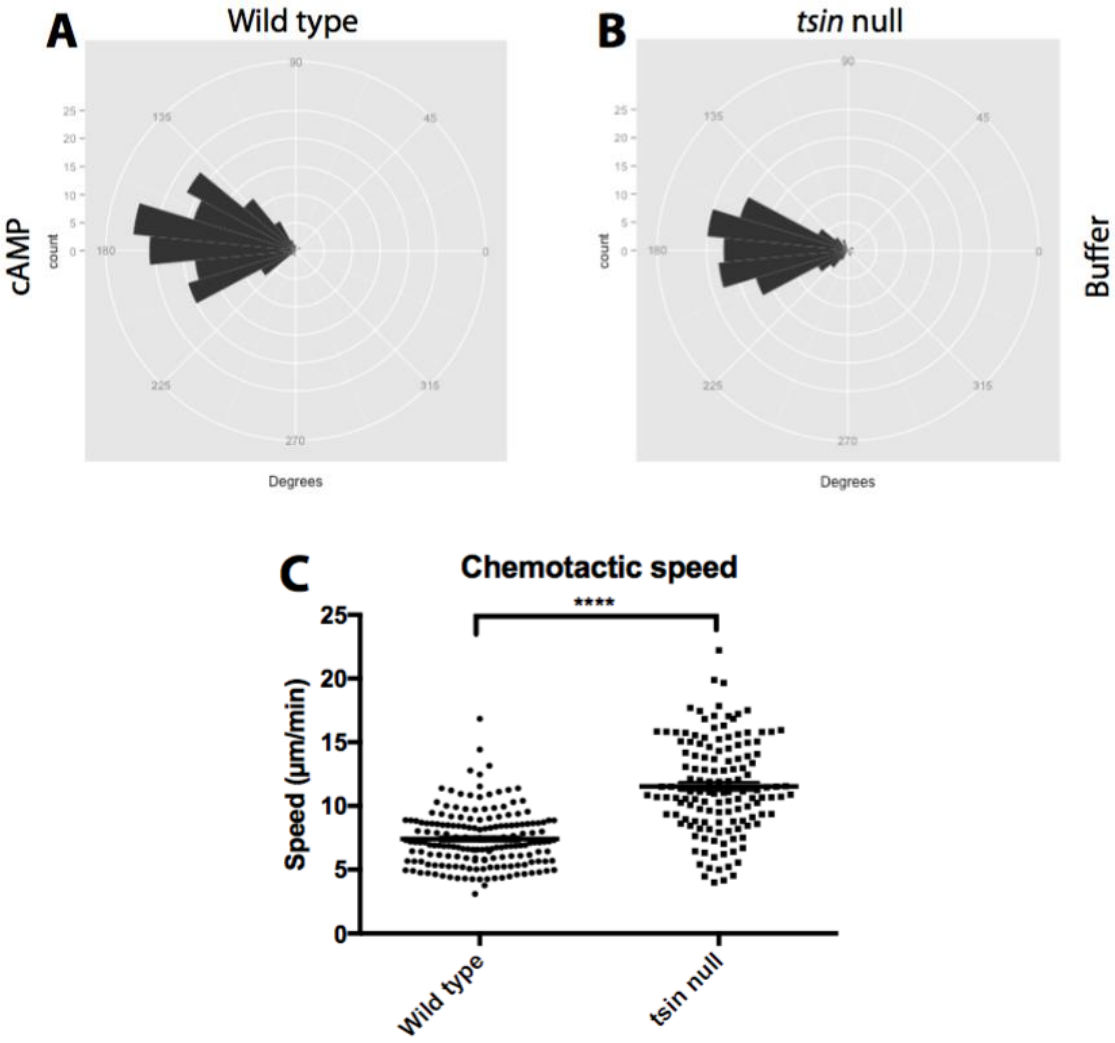

Figure 42: tsin- cells chemotax faster than wild-type cells.

FIGURE 42: *tsin*$^{-}$ cells chemotax faster than wild-type cells. A and B) WT control cells or tsin null cells were starved and pulsed with 150nM cAMP for five hours, plated in chemotactic chamber with 1mM cAMP to the left or buffer to the right. Rose plots showing chemotaxis of WT or *tsin*$^{-}$ cells toward cAMP. Cells were imaged for 20 minutes, their movement quantified using TRACKMATE plugin in FIJI. Each concentric ring represents 5 cells. The circle is binned by15 degree sections. **C)** Chemotatic speds of wild-type cells and *tsin*$^{-}$ cells. **** $p<0.0001$ using t-test.

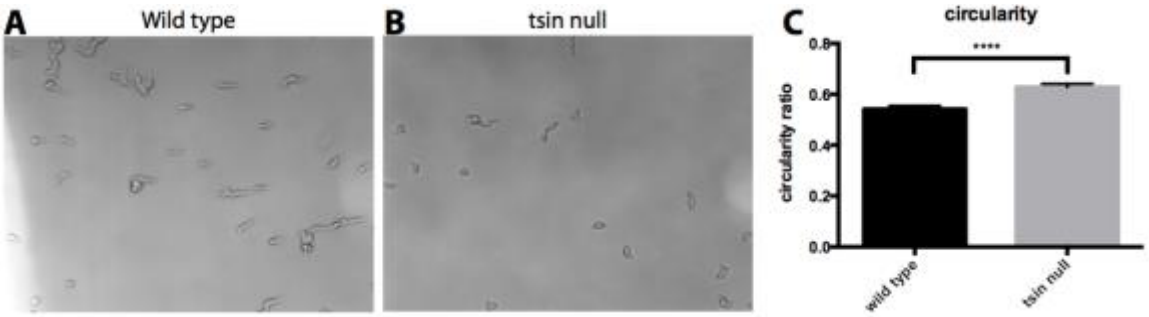

Figure 43: tsin- cells are less polarized during chemotaxis. A and B) Representative images of cells that were starved, pulsed with cAMP for 5 hours, and plated in a chemotactic chamber. The cells outlines were traced in FIJI and the circularity index was calculated. C) Quantification of circularity. The more circular a cell is, the closer to a perfect circle it is.

coverslip, the reflection from the coverslip will form an interference pattern from the tightly associated plasma membrane. However, where there is not a cell, or where a cell is not tightly adhered to the coverslip, there is no interference pattern, and the signal is a lighter grey.

In the vegetative state, *tsin*$^{-}$ cells have larger footprint as measured by IRM, although they also have a cell body circumference, suggesting that a lack of *tsin* may cause the cells to become more spread-out, adhered more tightly to the coverslip, or be larger in general (Figure 44).

To determine if *tsin*$^{-}$ null cells have defects in adhesion during directional cell migration, cells were pulsed with cAMP as described above, plated on glass bottom dishes, and imaged using both phase and IRM. The cells outline was traced in both the phase and IRM images, and the ratio of IRM footprint to cell size was determined. We found that the *tsin*$^{-}$ cells had a smaller ratio of cell perimeter to footprint when compared to wild-type controls cells (Figure 45). This decrease in the footprint of *tsin*$^{-}$ cells indicates that the cells are less adherent during migration than the wild-type controls, which suggests that *tsin* may play a conserved role in substrate adhesion (Hewett et al., 2006).

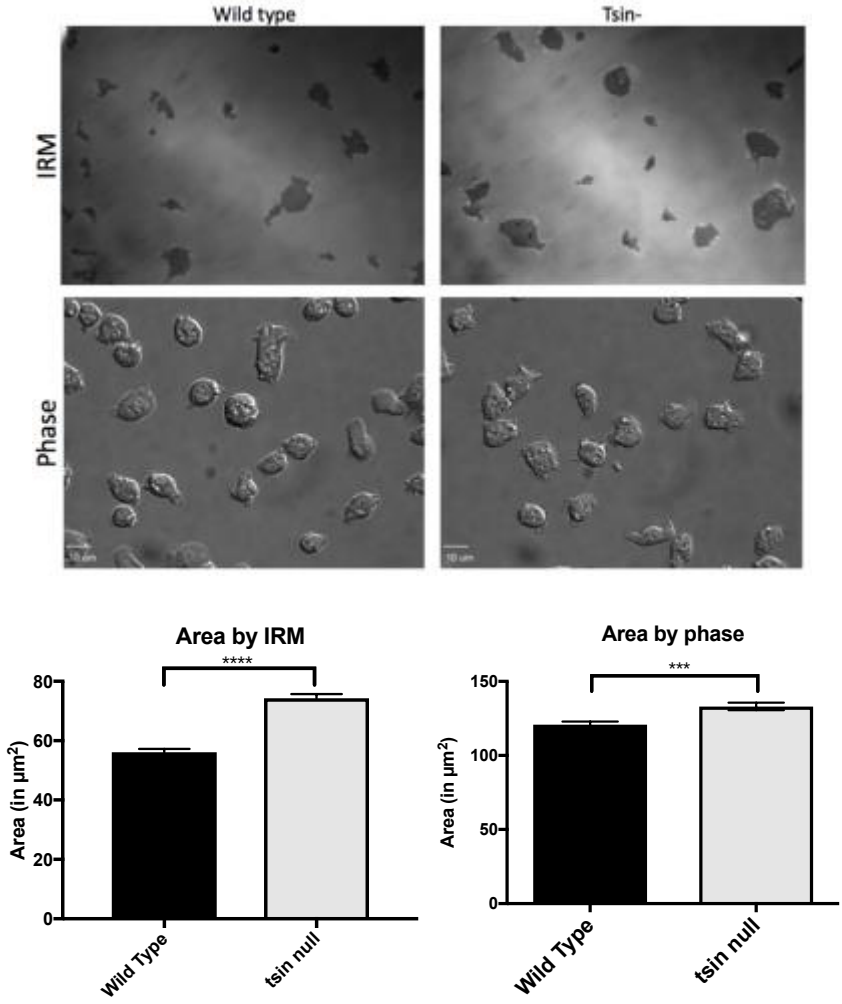

Figure 44: Size comparison of vegetative Dictyostelium by IRM and phase. **Representative images of vegetative cells.** Top row is IRM images, bottom row is Phase image. Quantification of cell contact area as determined by IRM. A mask was generated to calculate the contact area. Quantification of area of the cells as determined by phase.

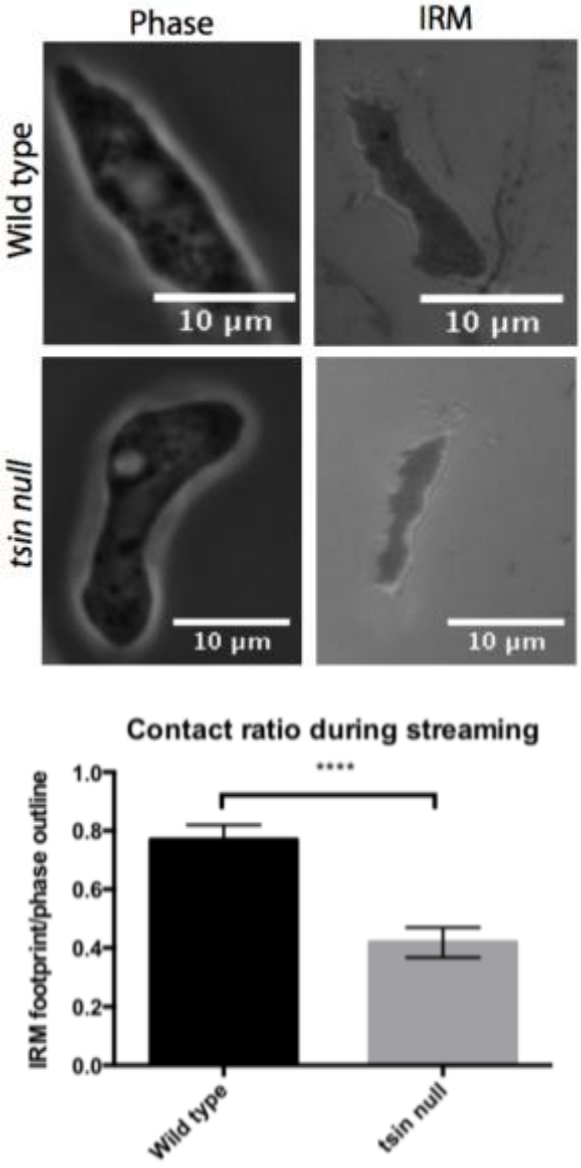

Figure 45: Tsin- cells are less adherent during chemotaxis

FIGURE 45: *Tsin*$^{-}$ cells are less adherent during chemotaxis. **A)** Representative images of a wild type cell (top) and a tsin null cell (bottom). Representative images of cells that were starved, pulsed with cAMP for 5 hours, and plated on an imaging dish. The cells were imaged in phase and IRM. The outline of the cells was traced and area determined by FIJI. **B)** Quantification the areal ratio of the outlines. **** $p<0.0001$ using t-test

DISCUSSION:

Here we showed that there are torsin homologs, defined here as AAA+ proteins localized to the shared lumen of the NE and ER, outside of metazoans. This suggests that torsins are more ancient and widespread than previously reported and appeared around the last eukaryotic ancestor. Phylogenetic analysis reveals that there are likely lineage specific ER retention mechanisms, and that more ancient torsin family members lack the hallmarks of metazoan torsins, such as non-canonical Walker-A motifs and a conserved GCK motif within the RSS. Using structural homology prediction software, we provide evidence that the *Dictyostelium* torsin homolog, named tsin, appears to have an arginine finger, which is also lacking in metazoans.

We show that EGFP-tsin localizes to the shared lumen of the NE/ER, and that mutation of the Walker-B motif causes enrichment of tsin within the NE and aberrant NE morphology, which reveals that the substrate of tsin likely resides within the NE. Walker-B mutations in human torsin1A also leads to enrichment of torsin1A to the NE, suggesting that NE localized AAA+ proteins have conserved function and substrates within the NE (Naismith et al., 2004; Goodchild and Dauer, 2004). However, the substrate of the torsin family of proteins has remained elusive. This is perhaps due in part to the fact that all organisms identified to date with a torsin homolog also have a LAP1/LULL1 homolog, which

have been shown to tightly bind to the substrate trap torsins, but are not substrates themselves (Zhao et al., 2013; Sosa et al., 2014). Using a new model organism that lacks LAP1/LULL1 homologs has the to potential to identify substrates of torsins.

Genetic disruption of *tsin* by homologous recombination causes several defects during development, including impairment of streaming as well as aberrant structures and timing in the mound phase. The *tsin*$^{-}$ cells have no defects in chemotaxing towards cAMP, and do so faster than wild-type cells. Cells lacking *tsin*$^{-}$ have aberrant adherence as measured by IRM. At this time, it is hard to ascribe a mechanism for tsin function. However, there are several hints about potential conserved mechanistic roles.

Mammalian *torsin1A* has been shown to be involved in cell-substrate adhesion and vesicular and protein trafficking in neurons (Hewett et al., 2006; Granata et al., 2008, 2011). *Dictyostelium* substrate adhesion is dependent upon delivery of SadA (Substrate Adhesion Defective) and SibA (Similar to Integrin Beta) proteins to the cell surface in order to contact the extracellular environment via van-der Waals interactions (Fey et al., 2002; Cornillon et al., 2008). As *Dictyostelium* begin to develop, their adhesion to the underlying substrate becomes diminished. However, this diminished adhesion is not mediated by SadA or SibA, as cells lacking these proteins had no decrease in cell-substrate adhesion (Tarantola et

al., 2014). Further developmental decrease in adhesion was seen when cells were treated with latrunculinA to disrupt actin organization. This treatment had little effect on vegetative cell adhesion (Tarantola et al., 2014). *Tsin*$^{-}$ cells exhibit a further decrease in adhesion than wild-type cells. Work in fibroblasts polarizing for migration has shown that torsinA affects actin cytoskeleton dynamics (Saunders et al., 2017). If tsin has similar functions to torsin1A, the decrease in adhesion during development seen in *tsin*$^{-}$ cells could be due in part to altered actin dynamics in developing *Dictyostelium.* While we detect slight increases in cell-substrate adhesion in vegetative cells, we also found that the cells appeared to be slightly larger (Figure 44). These results suggest that tsin may have a conserved role in actin cytoskeleton dynamics, resulting in defects in adhesion, although further experimentation is required.

Taken together, ER and NE luminal localized AAA+ proteins appear to have several conserved roles in cell biology throughout eukaryotes. In the future, determining if tsin can hydrolyze ATP without stimulators will be key to better understand its origins and cellular regulation. Furthermore, a more detailed interrogation of the adhesion defect will help better define the conserved role of torsins. Additionally, using the simpler system of *Dictyostelium*, identifying substrates of tsin has the potential to elucidate the molecular mechanisms of torsin function within the NE.

MATERIALS AND METHODS

Generation of DNA constructs:

Genomic DNA was used to clone tsin into a pSC-A vector (Agilent technologies, Santa Clara, CA) using PCR primers (forward CGCAAGCTTATGGGAAGGTATTTTTATCTCCAAT and reverse GCGCCTCGAGTTAATTTGTATTTTTATAAACATTTTTCGA) with cut sites HINDIII and XHOI, respectively. A BamHI site was introduced behind the predicted signal sequence (first 63 nucleotides) using site directed mutagenesis (Agilent technologies, Santa Clara, CA).

Fwd BamHI:

TATTTTTAAAATCATATTCAGGATCCGCACAAAATAATGATAAAAT

Rev BamHI: CATTTTTTATTTTATCATTATTTTGTGCGG

EGFP was then PCR amplified and inserted into the BamHI site using primers encoding BamHI cut sites:

Fwd - GCGGGATCCGTGAGCAAGGGCGAGGAG

Rev - ttttttGGATCCCTTGTACAGCTCGTCCATGC

The ATP hydrolysis mutant (E232Q) was generated using Q5 mutagenesis (New England Biolabs) using the following primers:

fwd - ATCACACTGTATGGACATTC

rev - TGTATTTGACcaaATTCAAAAAATTGATCC

The constructs were cloned from the pSC-A vector into the *Dictyostelium* expression vector pDXA-3C using restriction enzymes HindIII and XhoI.

To generate the *tsin* knock-out cassette, a Blasticidin resistance cassette was PCR amplified and inserted into an internal EcoRI site

Primers used to amplify BLAST insertion cassette

FWD: aaaaGAATTCAATTAACCATGGATAACTTCG

REV: tttttGAATTCCTGCAGGAATTAACCATGC

Generation and Identification of tsin null mutants: A tsin disruption plasmid was generated by inserting a Blasticidin cassette into the internal EcoRI site of tsin that was cloned into pDXA-3C. The resulting pDXA-3C plasmid was used as a template for PCR, which was then electrotransformed into Ax2 cells. Colonies that grew in HL5 supplemented with blasticidin (10mg/mL) were selected and screened by PCR using primer pairs that anneal to both sides of *tsin*.

Primers used for PCR analysis:

REV : TTGGAAAACTTTGGAATTAG (#467)

FWD : CACCCACACAAACAC (#466)

Phylogenetic analysis: Human torsin1a FASTA protein sequence (NCBI Reference Sequence: NP_000104.1) was used to BLASTP against other genomes. SMART analysis (EMBL) was used to as a preliminary check for torsin homology. A protein is considered a torsin if it has a predicted signal sequence (from two different sources SMART EMBL and ss pred) and an AAA+ domain, and was closely related to torsin, by reverse searching the protein sequence, should come back as torsin or ClpB (but with a signal sequence). Protein FASTA sequences were aligned and trees generated using PASTA with settings Aligner: MAFFT, Merger: MUSCLE, Tree Estimator FASTTREE, Model: WAG+G20. Decomposition: Centroid, Return: Best, Iteration limit: 10 (Liu et al Science 2009). Trees were generated in Dendroscope 3, and colored using Adobe Illustrator (Adobe Systems, San Jose, CA).

Cell Growth and development: Standard methods were used to maintain *Dictyostelium* strains (Fey et al 2007 Nature Methods). Cells were grown on tissue culture plates in HL5 supplemented with 10,000 U/mL Penicillin G (Fisher Scientific) and 10µg/mL streptomycin sulfate (Sigma Chemical Co). The tsin null mutants were maintained under constant selection in HL5 supplemented with Blasticidin S (ICN Biomedicals). Transformants expressing GFP, GFP-tsin, GFP-tubulin, GFP-CNX were maintained with HL5 supplemented with 10µg/mL G418 (Fisher Scientific). For development, log phase cells were rinsed and suspended in DB buffer to a final density of 1x10^7 cells/mL. The cells were shaken at 150-

200 rpm for 1 hour, then 150nM cAMP pulses were administered every 6 minutes for 4 hours. Cells were then rinsed with DB 2X and plated on imaging dishes.

Western Blotting analysis: Expression of the GFP tagged tsin was evaluated by western blot using mouse monoclonal anti-GFP antibody (MMS-118R; Covance Inc.). The washed blots were incubated with IRDye® 800 nm-conjugated goat anti-mouse secondary (LiCor Lincoln, NE). Detection was performed using Odyssey infrared imaging system (LI-COR Biosciences)

Million dicty dot assay (development assay): Cells grown in HL5 as described above were counted using a Coulter Counter (Beckman Coulter). 1x10^6 log phase cells were pelleted and re-suspended in 20µL HL5 and spotted on phosphate plates. Images were collected every minute for the duration of the timecourse using Leica MZFLIII dissection scope (Buffalo Grove, IL) with a Dage-MTI CCD 100 camera (Michigan City, IN) controlled by MetaVue v6.2 software (Sunnydale, CA).

Streaming assay: Log phase cells maintained as described above were collected and $1.5x10^7$ cells were plated on a 60mm dish. Cells were allowed to adhere, then rinsed with DB and DB was added to a final volume of 2mL. Cells were placed on a Leica microscope (from above) and imaged every minute for the duration of the experiment.

Phenotypic analysis:

For chemotaxis analysis, aggregation competent cells were placed in a µ-slide chemotaxis 3D chamber (Ibidi) and exposed to a cAMP gradient. The gradient was set up by placing 1mM cAMP in DB in one chamber and the DB vehicle in the other chamber. Cells were allowed to adhere, and once movement started, imaging began. Images were acquired on a Zeiss Axiovert 200 using a 20x air objective driven by Slidebook software (Intelligent Imaging Innovations, Denver, CO). Cell speeds were determined using the FIJI plugin TRACKMATE.

Phyre2 structural prediction analysis: tsin and ddclpB sequences were submitted individually to the Phyre2 server (Protein Homolgy/analogy Recognition Engine V2.0, Kelley et al 2015 Nature Protocols), run on intense mode. The resulting models were aligned using UCSF Chimera (version 1.10.2).

Statistics: All statistics were performed in Prism (GraphPad Software, La Jolla , CA)

Chapter 5

DISCUSSION:

My thesis work has been focused on understanding how resident proteins of the nuclear envelope connect the nucleoskeleton with the cytoskeleton by way of the Linker of Nucleoskeleton and Cytoskeleton (LINC) complex in cells undergoain centrosome orientation during directional cell migration. My work, in collaboration with members of Dr. Mueller's lab, has shown that the two most widely expressed SUN proteins, SUN1 and SUN2, form different oligomeric states within the nuclear envelope of living cells. Additionally, I have shown that the luminal localized AAA+ protein, torsinA, and its cofactor LAP1 are required for perinuclear retrograde actin flow as well as TAN line stability during rearward nuclear movement in fibroblasts undergoing centrosome orientation. Furthermore, I found that the torsin family of proteins has homologs throughout Eukaryota, and developed *Dictyostelium discoideum* as a novel model organism with which to elucidate conserved torsin functions.

In vivo analysis of SUN protein oligomerization

We were able to show for the first time in living cells that the luminal domain of SUN2 does trimerize, confirming the crystal structures that were solved by multiple groups starting in 2011 (Zhou et al., 2011; Sosa et al., 2012;

Wang et al., 2012; Nie et al., 2016). However, unlike the model put forth by Sosa et al (Sosa et al., 2012, 2013), where both SUN1 and SUN2 form trimers, we find that SUN1 behaves much differently from SUN2 within the nuclear envelope. Instead of trimerizing within the nuclear envelope, we find that the oligomeric state of SUN1 linearly increases with concentration. Although, like SUN2, the isolated SUN domain of SUN1 does not oligomerize within the nuclear envelope without a coiled-coil.

The oligomerization of SUN1 and SUN2 is dependent upon the local environment, as expression of either in the cytoplasm of cells results in differences in how both SUN proteins oligomerize. The luminal portion of SUN2 still oligomerizes, although it does so at lower concentrations, and requires the canonical coiled-coils. SUN1 oligomerization in the cytoplasm also differs from the lumen, with the oligomeric state no longer linearly increasing, but instead levels off as it approaches a tetramer. This indicates that SUN1 might not trimerize as predicted, but instead oligomerizes to form dimeric and tetrameric complexes, in line with previous biochemical findings (Lu et al., 2008).

Moving forward, it will be critical to better understand what endogenous factors regulate SUN oligomerization. From the crystal structures, it is predicted that calcium ion binding plays an important role in stabilizing the SUN domain. It will also be critical to understand what controls the interaction of the coiled-coil2 with the KASH lid of SUN2 (Nie et al., 2016). Additionally, while there is very high conservation of amino acid sequence of SUN domains, determining why these

two similar proteins behave differently will be critical to further our understanding of how they accomplish their specific roles in cells. While there is functional redundancy between SUN1 and SUN2, there are examples of separate functions within cells. For example, SUN1 has been shown to interact with nuclear pore complexes and anchor chromosomes during meiotic crossing over. Mutations in SUN1 are associated with Emery-Dreifuss Muscular Dystrophy. On the other hand, SUN2 acts as a tumor suppressor in lung cancer and is required for anchoring TAN lines to the nucleus during rearward nuclear movement in fibroblast (Bone and Starr, 2016).

Our findings that SUN1 and SUN2 form complexes of differing oligomeric states raises the question of what determines the oligomeric state of SUN proteins (Lu et al., 2008; Sosa et al., 2013). One potential model is that the SUN domain has little to no role in determining the oligomeric state of the protein. Instead, the coiled-coil domains of SUN1 and SUN2 are what determines the oligomeric state of the proteins. While SUN1 and SUN2 have very highly conserved amino acid sequences in their SUN domains, they differ in the organization of their coiled-coil domains (Haque et al., 2006). SUN2 has two canonical coiled-coils and a non-canonical coiled-coil located adjacent to the SUN domain (Sosa et al., 2012; Nie et al., 2016). The canonical coiled-coils as determined by Nie et al agree with coiled-coil prediction software (Lupas et al., 1991; Nie et al., 2016). Coiled-coil software often predicts that the luminal domain of SUN1 has either one large domain or a small and one large coiled-

coils domain, always farther away from the SUN domain compared to SUN2 coiled-coils (Haque et al., 2006; Tzur et al., 2006). Unfortunately, there is not a crystal structure available for confirmation.

Coiled-coils are regularly used to mediate protein-protein interactions and determine oligomeric states (Ciani et al., 2010). The most common oligomeric interaction states of coiled-coils are dimeric, trimeric, and tetrameric (Xu and Minor Jr, 2009). Point mutations in dimeric coiled-coils have been shown to cause them to change their oligomeric state from dimeric to trimeric interaction (Yoon et al., 2007). Other coiled-coils have been changed from trimeric coiled-coils to tetrameric coiled-coils (Xu and Minor Jr, 2009). Taken together, this leads to the model that the driving force which determines the final oligomeric state of SUN proteins is not the SUN domain, but instead the coiled-coils. In further support of this model, isolated coiled-coils of SUN2 can trimerize without the SUN domain present, but the SUN2 SUN domain is unable to oligomerize without coiled-coils (Nie et al., 2016). Indeed, using z-scan FFS, we find that both the SUN1 and SUN2 SUN domain do not oligomerize unless the coiled-coils are present on the molecule. With this in mind, one argument against this proposed model of coiled-coil driven differential oligomeric states is the high degree of conservation of SUN domains. It is hard to imagine how the SUN domain of SUN1 would be able stably bind to KASH peptides as either a dimer or tetramer, due to the intricate packing of the SUN2-KASH2 heterohexamer (Sosa et al., 2013; Ostlund et al., 2009).

There are several amino acid residues within all SUN domains that are absolutely conserved from *C. elegans* to *H. sapiens* (Sosa et al., 2012). Determining if these sites play any role in oligomerization and/or SUN-KASH interaction will be critical to understand regulation of SUN oligomerization. Several of these conserved residues are serine, threonine, and tyrosine, which makes them potential targets of post-translational modifications like phosphorylation. Mutation of these potential sites of post-translational modifications to residues unable to be post-translationally modified, like alanine or to a phosphomimetic like aspartic acid, coupled with analysis of oligomeric state using z-scan FFS will help to better understand if post-translational modifications control oligomerization of the SUN proteins within the nuclear envelope. There are additional residues that are highly conserved in either SUN1 but not SUN2, and vice versa (Sosa et al., 2012). These residues may contribute to differential regulation of oligomerization.

Coupling dual-color FFS (Fogarty et al., 2011) with z-scans will help determine not only oligomerization of SUN proteins, but binding and oligomeric states of intact LINC complexes. It has previously been proposed that SUN1 and SUN2 can interact to form hetero-oligomeric complexes (Lu et al., 2008). Dual-color z-scan FFS would allow for this model to be tested within the nuclear envelope.

TorsinA as a regulator of LINC complexes:

A potential regulator of LINC complex proteins is the NE/ER luminal localized AAA+ protein torsinA (Saunders and Luxton, 2016). AAA+ proteins typically operate as ring-shaped hexamers that structurally remodel substrates by coupling ATP hydrolysis with conformational changes (Hanson and Whiteheart, 2005). Using LPA stimulated fibroblasts polarizing along a wound edge, my work has shown that torsinA and its INM localized ATPase activator, LAP1, are required for rearward nuclear movement during centrosome orientation. Rearward nuclear movement in fibroblasts polarizing at a wound edge is mediated by assembly of higher-ordered nesprin-2G – SUN2 LINC complexes harnessing the forces generated by retrograde actin flow over the dorsal nuclear envelope (Luxton et al., 2010). These structures were name Transmembrane Actin-associated Nuclear (TAN) lines (Luxton et al., 2011). During rearward nuclear movement, torsinA not only localizes to TAN lines, but is required for their formation and persistence. Additionally, torsinA regulates the mobility of mini-N2G within the nuclear envelope, but not other LINC complex components, such as SUN1, SUN2, Nesprin3a, or Nesprin3b. In a novel finding, siRNA depletion of either torsinA or LAP1 or over-expression of the torsinA^{E171Q} mutant causes a decrease in dorsal perinuclear retrograde actin flow velocity, but not retrograde actin flow velocity in the front of the cell. This work also adds torsinA to the list of TAN line components, which includes Nesprin2G, SUN2, Samp1, and FHOD-1 (Luxton et al., 2010; Borrego-Pinto et al., 2012; Kutscheidt et al., 2014).

Future work elucidating the mechanism of torsinA function during rearward nuclear position will important to further elucidate is mechanistic role in cells polarizing for migration. For example, while the luminal domain of LAP1 has been shown *in vitro* to stimulate ATPase activity of torsinA via a conserved arginine finger, that same arginine finger is dispensable for rearward nuclear movement and centrosome orientation in the wounded fibroblast monolayer assay. This raises the possibility that torsinA may be working independently but in parallel with LAP1, or perhaps in an ATPase independent manner entirely. Most AAA+ proteins operate as ring shaped homohexamers, but a predominant model in the literature suggests that LAP1 and torsinA function as a heterohexameric ring to stimulate ATPase activity of torsinA (Sosa et al., 2014; Brown et al., 2014). Testing this model of heterohexamer versus homohexamer in the functional wounded fibroblast monolayer assay will be critical to better define the molecular mechanisms of torsinA dependent rearward nuclear movement during centrosome orientation.

One way to directly test the homo- vs. heterohexameric structure would be in a similar manner to a system that was developed to study ClpX, which is a bacterial AAA+ protein (Martin et al., 2005). By covalently linking up to six ClpX subunits together with a short 20 amino acid linker, Martin et al. were able to very elegantly show that ClpX operates as a hexamer and even determine whether the subunits hydrolyze ATP stochastically or sequentially (Martin et al., 2005). Constructing a similar system with torsinA and expressing it in torsin$^{-/-}$ MEFs

polarizing along a wound edge would shed light on the assembly of torsinA during centrosome orientation. Because the linker is present, the composition and order of the subunits is known. This system would also allow for the construction of a wide array of combinations of mutant and wild-type subunits within the hexamer, in order to test their effects on the potential ring structure and function, which could help determine the dominant-negative nature of the DYT1 mutation (Saunders and Luxton, 2016).

Replacing torsinA subunits with the luminal domain of either LAP1 or LULL1 would also allow for resolve of the operating principles of torsinA-LAP1/LULL1 holoenzyme. This forced heterohexamer would allow for a direct and controlled way to test whether LAP1 or LULL1 are incorporated into the hexamer during centrosome orientation. This would also reveal the order of subunits and their orientation to each other within the hexameric ring.

FFS has been applied to other AAA+ proteins, however do so with a NE localized AAA+ would require the application of the z-scan technique (Chakraborty et al., 2012; Aker et al., 2007). As mentioned above, coupling dual color FFS with z-scans would allow for the determination of whether and in what molecular ratios torsinA is interacting with LAP1 within the nuclear envelope. This would also allow us the ability to determine if torsinA is interacting with components of the LINC complex in living cells.

A Broader Conservation of the Torsin Family of AAA+ ATPases:

As a subfamily of the larger AAA+ protein family, torsins play critical roles in cell and developmental biology from their location within the shared lumen of the NE and ER (Saunders and Luxton, 2016). A single amino acid deletion in human torsin1A causes the early-onset neurological movement disorder DYT1 dystonia and the genetic loss of torsins is often lethal (Ozelius et al., 1997; Basham and Rose, 2001; Goodchild et al., 2005). Currently in the literature, torsins are thought to have arisen with obligate multicellular animals (Rose et al., 2015). The last part of my thesis dealt with phylogenetic analysis and conservation of the torsin family of proteins.

Prospective torsin protein sequences were gathered and analyzed in regards to the evolutionary relationship among the torsin family proteins. In this analysis, we found that torsins, much like nuclear pore complexes, the nuclear lamins, and LINC complexes (Devos et al., 2014). Based on the analysis, it seems that torsin-like AAA+ proteins actually arose with the last eukaryotic common ancestor. Because we were interested in the role of torsins during cellular migration and development, we decided to focus our efforts on characterizing the torsin homolog found in *Dictyostelium discoideum*, named *tsin*.

We began interrogation of *tsin* in *Dictyostelium discoideum*. I found that mutation of the Walker-B motif causes enhanced localization of EGFP-tsin to the nuclear envelope, suggesting that its substrate is found within the nuclear envelope, similar to mammalian systems (Goodchild and Dauer, 2004; Naismith et al., 2004). Additionally, through generation of *tsin* knockout cells (*tsin*$^{-}$), I found

that *tsin* is required for cellular streaming as well as passage through the mound phase of development. One potential mechanism for how *tsin*$^{-}$ cells might have aberrant development would be through inability to detect cAMP, which is the major chemoattractant in *Dictyostelium* development. However, we found that while *tsin*$^{-}$ have no defect chemotaxing towards cAMP, and move almost twice during chemotaxis.

A potential reason for the aberrant streaming and development of *tsin*$^{-}$ cells is defects in cell-cell or cell-substrate adhesion. To address this, we looked at cell-substrate adhesion during chemotaxis. When comparing the area of the cell by phase-contrast imaging to its contact area with the coverslip determined by IRM, *tsin*$^{-}$ cells had significantly reduced footprints compared to wild-type cells. This suggests that there is a disruption of adhesion molecules at the surface of the cell. We also observed that during streaming, the *tsin*$^{-}$ cells stick to each other more than wild-type cells, suggesting that both cell-substrate adhesion and cell-cell cohesion is affected by a lack of tsin.

Future efforts should work towards elucidating the mechanism responsible for the uncovered phenotypes *tsin*$^{-}$ cells. One key piece of information that has escaped detection in metazoan systems is the substrate of torsin. Currently, torsins are thought to be functional when interacting with LAP1 or LULL1 in an ATP-bound manner (Brown et al., 2014; Sosa et al., 2014). However, LAP1 and LULL1 homologs have not been detected outside of metazoans, but this may be because they are hard to identify based solely on primary amino acid sequence

(Sosa et al., 2014; Rose et al., 2015). This makes a model organism outside of metazoans especially useful for discovery of potential ancient forms of LAP1/LULL1, or identifying the origin of LAP1/LULL1. If more ancient LAP1 or LULL1 homologs are not found, this would make *Dictyostelium* be a simpler system to use for determination of torsin substrates, as there would not be the complicating factor of LAP1/LULL1 interactions. Using immunoprecipitation or the BioID system, identification of tsin interacting partners in *Dictyostelium* could help identify substrates of the torsin family (Kim and Roux, 2016). Finding substrates of the torsin family would help drive forward our understanding of regulation and function of the torsin proteins within the nuclear envelope, and what role they play during organelle positioning in migratory cells.

References

Aker, J., R. Hesselink, R. Engel, R. Karlova, J.W. Borst, A.J.W.G. Visser, and S.C. de Vries. 2007. In vivo hexamerization and characterization of the Arabidopsis AAA ATPase CDC48A complex using forster resonance energy transfer-fluorescence lifetime imaging microscopy and fluorescence correlation spectroscopy. *Plant Physiol.* 145:339–350. doi:10.1104/pp.107.103986.

Alanen, H.I., I.B. Raykhel, M.J. Luukas, K.E.H. Salo, and L.W. Ruddock. 2011. Beyond KDEL: The role of positions 5 and 6 in determining ER localization. *J. Mol. Biol.* 409:291–297. doi:10.1016/j.jmb.2011.03.070.

Aman, A., and T. Piotrowski. 2010. Cell migration during morphogenesis. *Dev. Biol.* 341:20–33. doi:10.1016/j.ydbio.2009.11.014.

Baker, T.A., and R.T. Sauer. 2012. ClpXP, an ATP-powered unfolding and protein-degradation machine. *Biochim. Biophys. Acta - Mol. Cell Res.* 1823:15–28. doi:10.1016/j.bbamcr.2011.06.007.

Bartolini, F., and G.G. Gundersen. 2006. Generation of noncentrosomal microtubule arrays. *J. Cell Sci.* 119:4155–63. doi:10.1242/jcs.03227.

Basham, S., and L. Rose. 1999. Mutations in ooc-5 and ooc-3 disrupt oocyte formation and the reestablishment of asymmetric PAR protein localization in two-cell Caenorhabditis elegans embryos. *Dev. Biol.* 215:253–263. doi:10.1006/dbio.1999.9447.

Basham, S., and L. Rose. 2001. The Caenorhabditis elegans polarity gene ooc-5 encodes a Torsin-related protein of the AAA ATPase superfamily. *Development*. 128:4645–4656.

Bone, C.R., and D.A. Starr. 2016. Nuclear migration events throughout development. *J. Cell Sci.* 129:1951–1961. doi:10.1242/jcs.179788.

Borrego-Pinto, J., T. Jegou, D.S. Osorio, F. Aurade, M. Gorjanacz, B. Koch, I.W. Mattaj, and E.R. Gomes. 2012. Samp1 is a component of TAN lines and is required for nuclear movement. *J. Cell Sci.* 125:1099–1105. doi:10.1242/jcs.087049.

Brown, R.S.H., C. Zhao, A.R. Chase, J. Wang, and C. Schlieker. 2014. The mechanism of Torsin ATPase activation. *Proc. Natl. Acad. Sci.* 111:E4822–E4831. doi:10.1073/pnas.1415271111.

Capitani, M., and M. Sallese. 2009. The KDEL receptor: New functions for an old protein. *FEBS Lett.* 583:3863–3871. doi:10.1016/j.febslet.2009.10.053.

Chakraborty, M., A.M. Kuriata, J. Nathan Henderson, M.E. Salvucci, R.M. Wachter, and M. Levitus. 2012. Protein oligomerization monitored by fluorescence fluctuation spectroscopy: self-assembly of rubisco activase. *Biophys. J.* 103:949–58. doi:10.1016/j.bpj.2012.07.034.

Chiplonkar, J.M., D.D. Vandré, and J.M. Robinson. 1992. Stimulus-dependent relocation of the microtubule organizing center in human polymorphonuclear leukocytes. *J. Cell Sci.* 102:723–728.

Ciani, B., S. Bjelic, S. Honnappa, H. Jawhari, R. Jaussi, A. Payapilly, T. Jowitt, M.O. Steinmetz, and R. a Kammerer. 2010. Molecular basis of coiled-coil oligomerization-state specificity. *Proc. Natl. Acad. Sci. U. S. A.* 107:19850–19855. doi:10.1073/pnas.1008502107.

Cornillon, S., R. Froquet, and P. Cosson. 2008. Involvement of sib proteins in the regulation of cellular adhesion in Dictyostelium discoideum. *Eukaryot. Cell*. 7:1600–1605. doi:10.1128/EC.00155-08.

Corrigan, A.M., and J.R. Chubb. 2014. Regulation of transcriptional bursting by a naturally oscillating signal. *Curr. Biol.* 24:205–211. doi:10.1016/j.cub.2013.12.011.

Crisp, M., Q. Liu, K. Roux, J.B. Rattner, C. Shanahan, B. Burke, P.D. Stahl, and D. Hodzic. 2006. Coupling of the nucleus and cytoplasm: role of the LINC complex. *J. Cell Biol.* 172:41–53. doi:10.1083/jcb.200509124.

Devos, D.P., R. Gräf, and M.C. Field. 2014. Evolution of the nucleus. *Curr. Opin. Cell Biol.* 28:8–15. doi:10.1016/j.ceb.2014.01.004.

Esra Demircioglu, F., B.A. Sosa, J. Ingram, H.L. Ploegh, and T.U. Schwartz. 2016. Structures of torsinA and its disease-mutant complexed with an activator reveal the molecular basis for primary dystonia. *Elife*. 5:1–14. doi:10.7554/eLife.17983.

Fey, P., a S. Kowal, P. Gaudet, K.E. Pilcher, and R.L. Chisholm. 2007. Protocols for growth and development of Dictyostelium discoideum. *Nat Protoc*. 2:1307–1316. doi:nprot.2007.178 [pii]\r10.1038/nprot.2007.178.

Fey, P., S. Stephens, M.A. Titus, and R.L. Chisholm. 2002. SadA, a novel adhesion receptor in Dictyostelium. *J. Cell Biol.* 159:1109–1119. doi:10.1083/jcb.200206067.

Fogarty, K.H., Y. Chen, I.F. Grigsby, P.J. Macdonald, E.M. Smith, J.L. Johnson, J.M. Rawson, L.M. Mansky, and J.D. Mueller. 2011. Characterization of cytoplasmic Gag-gag interactions by dual-color z-scan fluorescence fluctuation spectroscopy. *Biophys. J.* 100:1587–95. doi:10.1016/j.bpj.2011.02.008.

Folker, E.S., C. Ostlund, G.W.G. Luxton, H.J. Worman, and G.G. Gundersen. 2011. Lamin A variants that cause striated muscle disease are defective in anchoring transmembrane actin-associated nuclear lines for nuclear movement. *Proc. Natl. Acad. Sci. U. S. A.* 108:131–6. doi:10.1073/pnas.1000824108.

Gerace, L. 2004. TorsinA and torsion dystonia: Unraveling the architecture of the nuclear

envelope. *Proc. Natl. Acad. Sci. U. S. A.* 101:8839–8840. doi:10.1073/pnas.0402441101.

Glynn, S.E., A. Martin, A.R. Nager, T. a. Baker, and R.T. Sauer. 2009. Structures of Asymmetric ClpX Hexamers Reveal Nucleotide-Dependent Motions in a AAA+ Protein-Unfolding Machine. *Cell*. 139:744–756. doi:10.1016/j.cell.2009.09.034.

Glynn, S.E., A.R. Nager, T. a Baker, and R.T. Sauer. 2012. Dynamic and static components power unfolding in topologically closed rings of a AAA+ proteolytic machine. *Nat. Struct. Mol. Biol.* 19:616–622. doi:10.1038/nsmb.2288.

Gomes, E.R., S. Jani, and G.G. Gundersen. 2005. Nuclear movement regulated by Cdc42, MRCK, myosin, and actin flow establishes MTOC polarization in migrating cells. *Cell*. 121:451–63. doi:10.1016/j.cell.2005.02.022.

Goodchild, R.E., A.L. Buchwalter, and T. V Naismith. 2015. Access of torsinA to the inner nuclear membrane is activity dependent and regulated in the endoplasmic reticulum Journal of Cell Science Accepted manuscript. 2854–2865. doi:10.1242/jcs.167452.

Goodchild, R.E., and W.T. Dauer. 2004. Mislocalization to the nuclear envelope: an effect of the dystonia-causing torsinA mutation. *Proc. Natl. Acad. Sci. U. S. A.* 101:847–52. doi:10.1073/pnas.0304375101.

Goodchild, R.E., and W.T. Dauer. 2005. The AAA+ protein torsinA interacts with a conserved domain present in LAP1 and a novel ER protein. *J. Cell Biol.* 168:855–62. doi:10.1083/jcb.200411026.

Goodchild, R.E., C.E. Kim, and W.T. Dauer. 2005. Loss of the dystonia-associated protein torsinA selectively disrupts the neuronal nuclear envelope. *Neuron*. 48:923–32. doi:10.1016/j.neuron.2005.11.010.

Graef, M., G. Seewald, and T. Langer. 2007. Substrate recognition by AAA+ ATPases: distinct substrate binding modes in ATP-dependent protease Yme1 of the mitochondrial intermembrane space. *Mol. Cell. Biol.* 27:2476–85. doi:10.1128/MCB.01721-06.

Granata, A., S.J. Koo, V. Haucke, G. Schiavo, and T.T. Warner. 2011. CSN complex controls the stability of selected synaptic proteins via a torsinA-dependent process. *EMBO J.* 30:181–93. doi:10.1038/emboj.2010.285.

Granata, A., G. Schiavo, and T.T. Warner. 2009. TorsinA and dystonia: from nuclear envelope to synapse. *J. Neurochem.* 109:1596–609. doi:10.1111/j.1471-4159.2009.06095.x.

Granata, A., R. Watson, L.M. Collinson, G. Schiavo, and T.T. Warner. 2008. The dystonia-associated protein TorsinA modulates synaptic vesicle recycling. *J. Biol. Chem.* 283:7568–7579. doi:10.1074/jbc.M704097200.

Gribun, A., K.L.Y. Cheung, J. Huen, J. Ortega, and W. a Houry. 2008. Yeast Rvb1 and Rvb2 are ATP-dependent DNA helicases that form a heterohexameric complex. *J. Mol. Biol.* 376:1320–33. doi:10.1016/j.jmb.2007.12.049.

Gundersen, G.G., and H.J. Worman. 2013. Nuclear Positioning. *Cell*. 152:1376–1389. doi:10.1016/j.cell.2013.02.031.

Hanson, P.I., and S.W. Whiteheart. 2005. AAA+ proteins: have engine, will work. *Nat. Rev. Mol. Cell Biol.* 6:519–29. doi:10.1038/nrm1684.

Haque, F., D.J. Lloyd, D.T. Smallwood, C.L. Dent, C.M. Shanahan, A.M. Fry, R.C. Trembath, and S. Shackleton. 2006. SUN1 interacts with nuclear lamin A and cytoplasmic nesprins to provide a physical connection between the nuclear lamina and the cytoskeleton. *Mol. Cell. Biol.* 26:3738–51. doi:10.1128/MCB.26.10.3738-

3751.2006.

Hetzer, M.W., T.C. Walther, and I.W. Mattaj. 2005. PUSHING THE ENVELOPE: Structure, Function, and Dynamics of the Nuclear Periphery. *Annu. Rev. Cell Dev. Biol.* 21:347–380. doi:10.1146/annurev.cellbio.21.090704.151152.

Hewett, J.W., J. Zeng, B.P. Niland, D.C. Bragg, and X.O. Breakefield. 2006. Dystonia-causing mutant torsinA inhibits cell adhesion and neurite extension through interference with cytoskeletal dynamics. *Neurobiol. Dis.* 22:98–111. doi:10.1016/j.nbd.2005.10.012.

Vander Heyden, A.B., T. V Naismith, E.L. Snapp, and P.I. Hanson. 2011. Static retention of the lumenal monotopic membrane protein torsinA in the endoplasmic reticulum. *EMBO J.* 30:3217–31. doi:10.1038/emboj.2011.233.

Vander Heyden, A.B. Vander, T. V Naismith, E.L. Snapp, D. Hodzic, and P.I. Hanson. 2009. LULL1 Retargets TorsinA to the Nuclear Envelope Revealing an Activity That Is Impaired by the DYT1 Dystonia Mutation. 20:2661–2672. doi:10.1091/mbc.E09.

Jahed, Z., H. Shams, and M.R.K. Mofrad. 2015. A Disulfide Bond Is Required for the Transmission of Forces through SUN-KASH Complexes. *Biophys. J.* 109:501–9. doi:10.1016/j.bpj.2015.06.057.

Jungwirth, M.T., D. Kumar, D.Y. Jeong, and R.E. Goodchild. 2011. The nuclear envelope localization of DYT1 dystonia torsinA-ΔE requires the SUN1 LINC complex component. *BMC Cell Biol.* 12:24. doi:10.1186/1471-2121-12-24.

Kelly, L.A., S. Mezulis, C. Yates, M. Wass, and M. Sternberg. 2015. The Phyre2 web portal for protein modelling, prediction, and analysis. *Nat. Protoc.* 10:845–858. doi:10.1038/nprot.2015-053.

Kim, D.I., and K.J. Roux. 2016. Filling the Void: Proximity-Based Labeling of Proteins in

Living Cells. *Trends Cell Biol.* 26:804–817. doi:10.1016/j.tcb.2016.09.004.

Kriebel, P.W., V.A. Barr, and C.A. Parent. 2003. Adenylyl cyclase localization regulates streaming during chemotaxis. *Cell*. 112:549–560. doi:10.1016/S0092-8674(03)00081-3.

Kriebel, P.W., V.A. Barr, E.C. Rericha, G. Zhang, and C.A. Parent. 2008. Collective cell migration requires vesicular trafficking for chemoattractant delivery at the trailing edge. *J. Cell Biol.* 183:949–961. doi:10.1083/jcb.200808105.

Kutscheidt, S., R. Zhu, S. Antoku, G.W.G. Luxton, I. Stagljar, O.T. Fackler, and G.G. Gundersen. 2014. FHOD1 interaction with nesprin-2G mediates TAN line formation and nuclear movement. *Nat. Cell Biol.* 16:708–715. doi:10.1038/ncb2981.

Letunic, I., T. Doerks, and P. Bork. 2015. SMART: Recent updates, new developments and status in 2015. *Nucleic Acids Res.* 43:D257–D260. doi:10.1093/nar/gku949.

Li, R., and G.G. Gundersen. 2008. Beyond polymer polarity: how the cytoskeleton builds a polarized cell. *Nat. Rev. Mol. Cell Biol.* 9:860–73. doi:10.1038/nrm2522.

Liu, L., and C.A. Parent. 2011. TOR kinase complexes and cell migration. *J. Cell Biol.* 194:815–824. doi:10.1083/jcb.201102090.

Lombardi, M.L., and J. Lammerding. 2011. Keeping the LINC: the importance of nucleocytoskeletal coupling in intracellular force transmission and cellular function. *Biochem. Soc. Trans.* 39:1729–34. doi:10.1042/BST20110686.

Loomis, W.F. 2015. Genetic control of morphogenesis in Dictyostelium. *Dev. Biol.* 402:146–161. doi:10.1016/j.ydbio.2015.03.016.

De Lozanne, A., and J.A. Spudich. 1987. Disruption of the Dictyostelium myosin heavy chain gene by homologous recombination. *Science*. 236:1086–91. doi:10.1126/science.3576222.

Lu, W., J. Gotzmann, L. Sironi, V.-M. Jaeger, M. Schneider, Y. Lüke, M. Uhlén, C.A.-K. Szigyarto, A. Brachner, J. Ellenberg, R. Foisner, A.A. Noegel, and I. Karakesisoglou. 2008. Sun1 forms immobile macromolecular assemblies at the nuclear envelope. *Biochim. Biophys. Acta - Mol. Cell Res.* 1783:2415–2426. doi:10.1016/j.bbamcr.2008.09.001.

Luxton, G.G., E.R. Gomes, E.S. Folker, H.J. Worman, and G.G. Gundersen. 2011. TAN lines: a novel nuclear envelope structure involved in nuclear positioning. *Nucleus*. 2:173–81. doi:10.4161/nucl.2.3.16243.

Luxton, G.W.G., E.R. Gomes, E.S. Folker, E. Vintinner, and G.G. Gundersen. 2010. Linear Arrays of Nuclear Envelope Proteins Harness Retrograde Actin Flow for Nuclear Movement. *Science (80-.).* 329:956–959. doi:10.1126/science.1189072.

Luxton, G.W.G., and G.G. Gundersen. 2011. Orientation and function of the nuclear-centrosomal axis during cell migration. *Curr. Opin. Cell Biol.* 23:579–588. doi:10.1016/j.ceb.2011.08.001.

Majumdar, R., M. Sixt, and C.A. Parent. 2014. New paradigms in the establishment and maintenance of gradients during directed cell migration. *Curr. Opin. Cell Biol.* 30:33–40. doi:10.1016/j.ceb.2014.05.010.

Majumdar, R., A. Tavakoli Tameh, and C.A. Parent. 2016. Exosomes Mediate LTB4 Release during Neutrophil Chemotaxis. *PLoS Biol.* 14:1–28. doi:10.1371/journal.pbio.1002336.

Maric, M., J. Shao, R.J. Ryan, C.-S. Wong, P. Gonzalez-Alegre, and R.J. Roller. 2011. A Functional Role for TorsinA in Herpes Simplex Virus 1 Nuclear Egress. *J. Virol.* 85:9667–9679. doi:10.1128/JVI.05314-11.

Martin, A., T.A. Baker, and R.T. Sauer. 2008. Diverse pore loops of the AAA+ ClpX

machine mediate unassisted and adaptor-dependent recognition of ssrA-tagged substrates. *Mol. Cell*. 29:441–50. doi:10.1016/j.molcel.2008.02.002.

Martin, A., T. a Baker, and R.T. Sauer. 2005. Rebuilt AAA + motors reveal operating principles for ATP-fuelled machines. *Nature*. 437:1115–20. doi:10.1038/nature04031.

McCarthy, D.M., V. Gioioso, X. Zhang, N. Sharma, and P.G. Bhide. 2012. Neurogenesis and neuronal migration in the forebrain of the TorsinA knockout mouse embryo. *Dev. Neurosci.* 34:366–78. doi:10.1159/000342260.

Meier, I. 2016. LINCing the eukaryotic tree of life – towards a broad evolutionary comparison of nucleocytoplasmic bridging complexes. *J. Cell Sci.* jcs.186700. doi:10.1242/jcs.186700.

Mirarab, S., N. Nguyen, and T. Warnow. 2014. PASTA: Ultra-Large Multiple Sequence Alignment. *Proc. RECOMB*. 177–191.

Monnat, J., E.M. Neuhaus, M.S. Pop, D.M. Ferrari, B. Kramer, and T. Soldati. 2000. Identification of a novel saturable endoplasmic reticulum localization mechanism mediated by the C-terminus of a Dictyostelium protein disulfide isomerase. *Mol. Biol. Cell*. 11:3469–84.

Müller-Taubenberger, A., A.N. Lupas, H. Li, M. Ecke, E. Simmeth, and G. Gerisch. 2001. Calreticulin and calnexin in the endoplasmic reticulum are important for phagocytosis. *EMBO J.* 20:6772–6782. doi:10.1093/emboj/20.23.6772.

Nagy, M., H.-C. Wu, Z. Liu, S. Kedzierska-Mieszkowska, and M. Zolkiewski. 2009. Walker-A threonine couples nucleotide occupancy with the chaperone activity of the AAA+ ATPase ClpB. *Protein Sci.* 18:287–93. doi:10.1002/pro.36.

Naismith, T. V, J.E. Heuser, X.O. Breakefield, and P.I. Hanson. 2004. TorsinA in the

nuclear envelope. *Proc. Natl. Acad. Sci. U. S. A.* 101:7612–7. doi:10.1073/pnas.0308760101.

Nery, F.C., I. a Armata, J.E. Farley, J. a Cho, U. Yaqub, P. Chen, C.C. da Hora, Q. Wang, M. Tagaya, C. Klein, B. Tannous, K. a Caldwell, G. a Caldwell, W.I. Lencer, Y. Ye, and X.O. Breakefield. 2011. TorsinA participates in endoplasmic reticulum-associated degradation. *Nat. Commun.* 2:393. doi:10.1038/ncomms1383.

Nery, F.C., C.C. da Hora, N. a. Atai, E.Y. Kim, J. Hettich, T.R. Mempel, X.O. Breakefield, and D. Irimia. 2014. Microfluidic platform to evaluate migration of cells from patients with DYT1 dystonia. *J. Neurosci. Methods*. 232:181–188. doi:10.1016/j.jneumeth.2014.05.027.

Nie, S., H. Ke, F. Gao, J. Ren, M. Wang, L. Huo, W. Gong, and W. Feng. 2016. Coiled-Coil Domains of SUN Proteins as Intrinsic Dynamic Regulators. *Structure*. 24:80–91. doi:10.1016/j.str.2015.10.024.

Ostlund, C., E.S. Folker, J.C. Choi, E.R. Gomes, G.G. Gundersen, and H.J. Worman. 2009. Dynamics and molecular interactions of linker of nucleoskeleton and cytoskeleton (LINC) complex proteins. *J. Cell Sci.* 122:4099–108. doi:10.1242/jcs.057075.

Ozelius, L.J., J.W. Hewett, C.E. Page, S.B. Bressman, P.L. Kramer, C. Shalish, D. de Leon, M.F. Brin, D. Raymond, D.P. Corey, S. Fahn, N.J. Risch, a J. Buckler, J.F. Gusella, and X.O. Breakefield. 1997. The early-onset torsion dystonia gene (DYT1) encodes an ATP-binding protein. *Nat. Genet.* 17:40–48. doi:10.1038/ng0997-40.

Pagny, S., P. Lerouge, L. Faye, and V. Gomord. 1999. Signals and mechanisms for protein retention in the endoplasmic reticulum. *J. Exp. Bot.* 50:157–164. doi:10.1093/jxb/50.331.157.

Petersen, T.N., S. Brunak, G. von Heijne, and H. Nielsen. 2011. SignalP 4.0: discriminating signal peptides from transmembrane regions. *Nat. Methods*. 8:785–6. doi:10.1038/nmeth.1701.

Ponte, E., F. Rivero, M. Fechheimer, a Noegel, and S. Bozzaro. 2000. Severe developmental defects in Dictyostelium null mutants for actin-binding proteins. *Mech. Dev.* 91:153–61. doi:10.1016/S0925-4773(99)00292-0.

Price, M.N., P.S. Dehal, and A.P. Arkin. 2010. FastTree 2 - Approximately maximum-likelihood trees for large alignments. *PLoS One*. 5. doi:10.1371/journal.pone.0009490.

Rauniyar, N., K. Subramanian, M. Lavallee-Adam, S. Martinez-Bartolome, W.E. Balch, and J.R. 3rd Yates. 2015. Quantitative Proteomics of Human Fibroblasts with I1061T Mutation in Niemann-Pick C1 (NPC1) Protein Provides Insights into the Disease Pathogenesis. *Mol. Cell. Proteomics*. 14:1734–1749. doi:10.1074/mcp.M114.045609.

Ridley, A.J. 2011. Life at the leading edge. *Cell*. 145:1012–1022. doi:10.1016/j.cell.2011.06.010.

Rivero, F., A. Kuspa, R. Brokamp, M. Matzner, and A.A. Noegel. 1998. Interaptin, an Actin-binding Protein of the ⌴ -Actinin Superfamily in. *Cell*. 142:735–750.

Roll-Mecak, A., and R.D. Vale. 2008. Structural basis of microtubule severing by the hereditary spastic paraplegia protein spastin. *Nature*. 451:363–367. doi:10.1038/nature06482.

Román-Hernández, G., J.Y. Hou, R. a. Grant, R.T. Sauer, and T. a. Baker. 2011. The ClpS Adaptor Mediates Staged Delivery of N-End Rule Substrates to the AAA+ ClpAP Protease. *Mol. Cell*. 43:217–228. doi:10.1016/j.molcel.2011.06.009.

Rose, A.E., R.S.H. Brown, and C. Schlieker. 2015. Torsins: not your typical AAA+ ATPases. *Crit. Rev. Biochem. Mol. Biol.* 50:532–49. doi:10.3109/10409238.2015.1091804.

Rose, A.E., C. Zhao, E.M. Turner, A.M. Steyer, and C. Schlieker. 2014. Arresting a Torsin ATPase reshapes the endoplasmic reticulum. *J. Biol. Chem.* 289:552–564. doi:10.1074/jbc.M113.515791.

Roux, K.J., M.L. Crisp, Q. Liu, D. Kim, S. Kozlov, C.L. Stewart, and B. Burke. 2009. Nesprin 4 is an outer nuclear membrane protein that can induce kinesin-mediated cell polarization. *Proc. Natl. Acad. Sci. U. S. A.* 106:2194–9. doi:10.1073/pnas.0808602106.

Saffian, D., I. Grimm, W. Girzalsky, and R. Erdmann. 2012. ATP-dependent assembly of the heteromeric Pex1p-Pex6p-complex of the peroxisomal matrix protein import machinery. *J. Struct. Biol.* 179:126–32. doi:10.1016/j.jsb.2012.06.002.

Sameshima, M., Y. Imai, and Y. Hashimoto. 1988. The position of the microtubule-organizing center relative to the nucleus is independent of the direction of cell migration in Dictyostelium discoideum. *Cell Motil. Cytoskeleton*. 9:111–6. doi:10.1002/cm.970090203.

Sauer, R.T., and T. a Baker. 2011. AAA+ proteases: ATP-fueled machines of protein destruction. *Annu. Rev. Biochem.* 80:587–612. doi:10.1146/annurev-biochem-060408-172623.

Saunders, C.A., and G.W.G. Luxton. 2016. LINCing Defective Nuclear-Cytoskeletal Coupling and DYT1 Dystonia. *Cell. Mol. Bioeng.* 9:207–216. doi:10.1007/s12195-016-0432-0.

Schmoranzer, J., J.P. Fawcett, M. Segura, S. Tan, R.B. Vallee, T. Pawson, and G.G.

Gundersen. 2009. Par3 and Dynein Associate to Regulate Local Microtubule Dynamics and Centrosome Orientation during Migration. *Curr. Biol.* 19:1065–1074. doi:10.1016/j.cub.2009.05.065.

Schulz, I., O. Baumann, M. Samereier, C. Zoglmeier, and R. Gräf. 2009. Dictyostelium Sun1 is a dynamic membrane protein of both nuclear membranes and required for centrosomal association with clustered centromeres. *Eur. J. Cell Biol.* 88:621–638. doi:10.1016/j.ejcb.2009.06.003.

Soding, J. 2005. Protein homology detection by HMM-HMM comparison. *Bioinformatics*. 21:951–960. doi:10.1093/bioinformatics/bti125.

Sosa, B.A., F.E. Demircioglu, J.Z. Chen, J. Ingram, H.L. Ploegh, and T.U. Schwartz. 2014. How lamina-associated polypeptide 1 (LAP1) activates Torsin. *Elife*. 3:e03239. doi:10.7554/eLife.03239.

Sosa, B.A., U. Kutay, and T.U. Schwartz. 2013. Structural insights into LINC complexes. *Curr. Opin. Struct. Biol.* 23:285–291. doi:10.1016/j.sbi.2013.03.005.

Sosa, B.A., A. Rothballer, U. Kutay, and T.U. Schwartz. 2012. LINC Complexes Form by Binding of Three KASH Peptides to Domain Interfaces of Trimeric SUN Proteins. *Cell*. 149:1035–1047. doi:10.1016/j.cell.2012.03.046.

Speese, S.D., J. Ashley, V. Jokhi, J. Nunnari, R. Barria, Y. Li, B. Ataman, A. Koon, Y.-T. Chang, Q. Li, M.J. Moore, and V. Budnik. 2012. Nuclear Envelope Budding Enables Large Ribonucleoprotein Particle Export during Synaptic Wnt Signaling. *Cell*. 149:832–846. doi:10.1016/j.cell.2012.03.032.

Starr, D.A., and J.A. Fischer. 2005. KASH ’n Karry: The KASH domain family of cargo-specific cytoskeletal adaptor proteins. *BioEssays*. 27:1136–1146. doi:10.1002/bies.20312.

Stewart, R.M., A.E. Zubek, K.A. Rosowski, S.M. Schreiner, V. Horsley, and M.C. King. 2015. Nuclear-cytoskeletal linkages facilitate cross talk between the nucleus and intercellular adhesions. *J. Cell Biol.* 209:403–418. doi:10.1083/jcb.201502024.

Stinson, B.M., A.R. Nager, S.E. Glynn, K.R. Schmitz, T.A. Baker, and R.T. Sauer. 2013. Nucleotide Binding and Conformational Switching in the Hexameric Ring of a AAA+ Machine. *Cell*. 153:628–639. doi:10.1016/j.cell.2013.03.029.

Tarantola, M., A. Bae, D. Fuller, E. Bodenschatz, W.J. Rappel, and W.F. Loomis. 2014. Cell substratum adhesion during early development of dictyostelium discoideum. *PLoS One*. 9:1–7. doi:10.1371/journal.pone.0106574.

Tikhonenko, I., V. Magidson, R. Graf, A. Khodjakov, and M.P. Koonce. 2013. A kinesin-mediated mechanism that couples centrosomes to nuclei. *Cell Mol Life Sci*. 70:1285–1296. doi:10.1007/s00018-012-1205-0.

Tzur, Y.B., K.L. Wilson, and Y. Gruenbaum. 2006. SUN-domain proteins: “Velcro” that links the nucleoskeleton to the cytoskeleton. *Nat. Rev. Mol. Cell Biol.* 7:782–8. doi:10.1038/nrm2003.

VanGompel, M.J.W., K.C.Q. Nguyen, D.H. Hall, W.T. Dauer, and L.S. Rose. 2015. A novel function for the Caenorhabditis elegans torsin OOC-5 in nucleoporin localization and nuclear import. *Mol. Biol. Cell*. 26:1752–1763. doi:10.1091/mbc.E14-07-1239.

Wang, W., Z. Shi, S. Jiao, C. Chen, H. Wang, G. Liu, Q. Wang, Y. Zhao, M.I. Greene, and Z. Zhou. 2012. Structural insights into SUN-KASH complexes across the nuclear envelope. *Cell Res.* 22:1440–1452. doi:10.1038/cr.2012.126.

Weber, I., E. Wallraff, R. Albrecht, and G. Gerisch. 1995. Motility and substratum adhesion of Dictyostelium wild-type and cytoskeletal mutant cells: a study by

RICM/bright-field double-view image analysis. *J. Cell Sci.* 108 (Pt 4:1519–1530.

Wendler, P., S. Ciniawsky, M. Kock, and S. Kube. 2012. Structure and function of the AAA+ nucleotide binding pocket. *Biochim. Biophys. Acta*. 1823:2–14. doi:10.1016/j.bbamcr.2011.06.014.

White, S.R., K.J. Evans, J. Lary, J.L. Cole, and B. Lauring. 2007. Recognition of C-terminal amino acids in tubulin by pore loops in Spastin is important for microtubule severing. *J. Cell Biol.* 176:995–1005. doi:10.1083/jcb.200610072.

White, S.R., and B. Lauring. 2007. AAA+ ATPases: achieving diversity of function with conserved machinery. *Traffic*. 8:1657–67. doi:10.1111/j.1600-0854.2007.00642.x.

Wilson, K.L., and S.C. Dawson. 2011. Functional evolution of nuclear structure. *J. Cell Biol.* 195:171–181. doi:10.1083/jcb.201103171.

Xiong, H., F. Rivero, U. Euteneuer, S. Mondal, S. Mana-Capelli, D. Larochelle, A. Vogel, B. Gassen, and A.A. Noegel. 2008. Dictyostelium Sun-1 connects the centrosome to chromatin and ensures genome stability. *Traffic*. 9:708–724. doi:10.1111/j.1600-0854.2008.00721.x.

Xu, Q., and D.L. Minor Jr. 2009. Crystal structure of a trimeric form of the K V 7 . 1 (KCNQ1) A-domain tail coiled-coil reveals structural plasticity and context dependent changes in a putative coiled-coil trimerization motif. 18:2100–2114. doi:10.1002/pro.224.

Yoon, M.K., H.M. Kim, G. Choi, J.O. Lee, and B.S. Choi. 2007. Structural basis for the conformational integrity of the Arabidopsis thaliana HY5 leucine zipper homodimer. *J. Biol. Chem.* 282:12989–13002. doi:10.1074/jbc.M611465200.

Zeymer, C., T.R.M. Barends, N.D. Werbeck, I. Schlichting, and J. Reinstein. 2014. Elements in nucleotide sensing and hydrolysis of the AAA+ disaggregation machine

ClpB: A structure-based mechanistic dissection of a molecular motor. *Acta Crystallogr. Sect. D Biol. Crystallogr.* 70:582–595. doi:10.1107/S1399004713030629.

Zhao, C., R.S.H. Brown, A.R. Chase, M.R. Eisele, and C. Schlieker. 2013. Regulation of Torsin ATPases by LAP1 and LULL1. *Proc. Natl. Acad. Sci. U. S. A.* 2013. doi:10.1073/pnas.1300676110.

Zhou, Z., X. Du, Z. Cai, X. Song, H. Zhang, T. Mizuno, Q. Wang, M.I. Greene, J.M. Building, and H. Walk. 2011. Structure of the SUN domain defines features of a molecular bridge in the nuclear envelope. doi:10.1074/jbc.M111.304543.

Zhu, L., L. Millen, J.L. Mendoza, and P.J. Thomas. 2010. A unique redox-sensing sensor II motif in TorsinA plays a critical role in nucleotide and partner binding. *J. Biol. Chem.* 285:37271–80. doi:10.1074/jbc.M110.123471.

Zhu, L., J.O. Wrabl, A.P. Hayashi, L.S. Rose, and P.J. Thomas. 2008. The Torsin-family AAA Protein OOC-5 Contains a Critical Disulfide Adjacent to Sensor-II That Couples Redox State to Nucleotide Binding. 19:3599–3612. doi:10.1091/mbc.E08.